Antiproton and Pion Structure Functions From

Dimuon Production at 125GeV/c

W.   Schappert

Physics Department

McGill University, Montreal.

August, 1984

A thesis submitted to the Faculty of Graduate Studies and Research

in partial fulfillment of the degree of

Doctor of Philosophy

Antiproton and Pion Structure Functions From Dimuon Production

Abstract

The cross sections for muon pair production in antiproton-nucleus and pion-nucleus collisions have been measured using a 125 GeV/c beam incident on a tungsten target. Both cross sections agree well with data scaled from other beam energies. The measured cross section for antiproton produced pairs is a factor of K = 2.45 larger than the predictions of the Drell-Yan model using structure functions measured by deep inelastic lepton scattering experiments.

The Drell-Yan formula has been inverted and the antiproton and pion valence structure functions have been extracted from the data. The shape of the antiproton structure function agrees well with the shape of the proton structure function measured by deep inelastic scattering experiments. The shape and magnitude of both the antiproton and the pion structure functions agree well with measurements made by other muon pair experiments.

Sommaire

Les sections efficaces de productions de pairs de muons dans les collisions antiproton-noyau et pion-noyau ont été mesurées au moyen d'un faisceau de 125 GeV/c focalisé sur une cible de tungstène. Ces deux sections efficaces sont en bon accord avec d'autres données, apres correction pour la difference d'énergie incidente. La section efficace déduite de nos données, pour la réaction antiproton-noyau, est un facteur K=2.45 plus grande que celle prédite par le modèle de Drell-Yan, utitlisant les fonctions de structure mesurées dans les experiences de diffusions inélastiques profondes lepton-noyau.

La formule de Drell-Yan a été inversée et les fonctions de structure "de valence" de l'antiproton et du pion ont été extraites de nos données. La forme de la fonction de structure de l'antiproton est similaire à celle du proton, mesurée dans les experiences de diffusions inelastiques profondes. La forme et l'amplitude des fonctions de structure de l'antiproton et du pion sont en bonne accord avec celles déduites d'autres mesures.

Original Material

The results obtained by the E537 Collaboration represent the best measurement to date of muon pair production in antiproton-nucleon collisions, and as such, are a good test of the Drell-Yan model. My contributions to the work of the collaboration included:

1. the testing and installation of one of the drift chambers;

2. testing and maintenance of the drift chamber electronics system;

3. maintenance of the online software in cooperation with Carl Akerlof, Sergio Conetti, and Dave Nitz;

4. the development of the vertex reconstruction programme in cooperation with Morris Binkley;

5. the development of the Monte Carlo simulation programme;

6. the development of the maximum likelihood fitting programme;

7. the extraction of the stucture functions from the data; and

8. participation in the running and general operation of the experiment.

Acknowledgements

Modern high energy physics experiments are the result of the work of many people. In addition to work by the members of the collaboration, the successful completion of Experiment 537 owes much to the accelerator operators, the crew chiefs, the beam line support personnel, riggers, the online computer maintenance personnel, the mainframe computer operators, the Computing Department consultants, and the librarians, among others, at Fermilab and the participating universities. This list is by no means exhaustive. The experiment had excellent technical support from the Fermilab Physics Department, notably, Garvie Hale, Karen Kephart, and Don Trentlage.

Among the members of the collaboration, Bob Wagner deserves special thanks for the endless hours and the attention to detail that he devoted to the experiment. I also want to thank my advisior, Dave Ryan, for his advice and guidance, for his careful reading of this thesis, and for looking out for my best interests over the course of five years. Among the many people I had a chance to work with closely over the course of the experiment, I would like to particularly thank Hari Areti, Morris Binkley, Sergio Conetti, Janice Enagonio, and Paul Lebrun.

Table of Contents

List of Figures

List of Tables

CHAPTER 1

Introduction

The production of pairs of muons in the collisions of sub-atomic particles has been extensively studied since the original observation of a significant signal at Brookhaven in 1970[1]. This process provides us with a new tool to study the fundamental constituents of nature and their interactions.

Historically the bulk of our knowledge about the fundamental structure of matter has come from the scattering of elementary particles or the study of the bound states that they form. The scattering of α particles from gold foils in the early 1900's led Rutherford, Geiger and Marsden[2] to propose a picture of the atom as composed of a heavy charged nucleus surrounded by a cloud of orbiting electrons. Problems associated with the classical description of the hydrogen atom provided much of the impetus for the subsequent development of quantum mechanics. The discovery of the neutron

in 1932 by Chadwick[3][4] allowed all known matter to be described as bound states of the three fundamental particles known at that time, the electron, the proton and the neutron.

With the development of the accelerator, it became apparent that sufficiently energetic collisions were able to create more new particles and antiparticles in inelastic collisions. By the end of the 1950's hundreds of previously unknown particles had been discovered, calling into question the very concept of a fundamental particle. At the same time elastic scattering experiments at Stanford[5] using high energy electrons demonstrated that the proton and the neutron were not point-like particles, but had a finite size, leading to speculation that they themselves might be composite. The proliferating numbers of sub-atomic particles took on a pattern if it was assumed that they were, in fact, bound states of fractionally charged constituents named quarks. The quark model, as proposed independently by Gell-Mann[6] and Zweig[7] in 1964, did not identify the quarks with physical objects but rather used them more as a bookeeping device. The experimental state of the art at the time, while able to show that the nucleon was not a point-like object, was not able distinguish any substructure within. Subsequent inelastic electron scattering experiments at Stanford Linear Accelerator (SLAC) in the late 1960's and early 1970's were able to resolve internal substructure. The pattern of scattered electrons was consistent with a picture in which the nucleon was a bound state of fractionally charged point-like constituents, which were called partons.

The picture that emerged is shown schematically in the Feynman diagrams of Figure 1. The diagrams provide a graphical representation of the mathematical description of the interactions of charged particles in
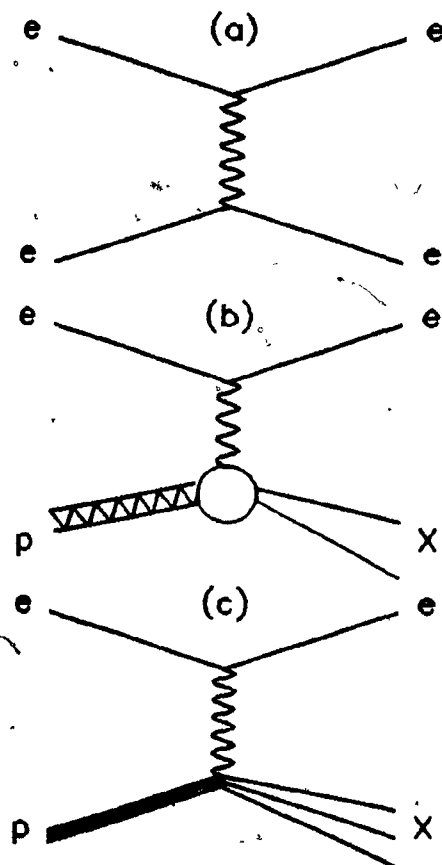
Figure 1 - Deep Inelastic Scattering

The top diagram shows the Feynman diagram for electron-electron scattering. Electrons are represented by single lines. The process is well described by QED in terms of the exchange of a single photon (wavy line). The middle diagram shows the general case of inclusive inelastic electron-nucleon scattering. The state X represents any possible final state. The interaction of the photon with the nucleon is unknown (as shown by the bubble at the photon-nucleon vertex). The bottom diagram shows the parton model picture of inclusive inelastic electron-nucleon scattering. Here the nucleon is represented as a sum of free constituents, represented as three single lines. The interaction of the photon with the constituents is given by QED in direct analogy with electron-electron scattering. Interactions between the constituents in the final state are ignored.

space-time. The horizontal direction represents the time dimension, while the vertical direction represents the three spatial dimensions. Figure 1a shows the description of the scattering of two electrons using Quantum Electrodynamics or QED. The point-like electrons are described as quantum mechanical waves and are represented by single lines. The interaction between the electrons is described by the exchange of a photon, as represented by the wavy line. Figure 1b shows the general case of electron-proton scattering. Because the electron cannot interact strongly, the electron part of the interaction is given completely by QED in terms of a point interaction with a photon. The proton, on the other hand, is not a point-like particle, and its interaction with the photon, shown as a bubble at the vertex in Figure 1b, is not known. In the picture of the proton that emerged from the SLAC results, the proton was represented by a sum of fractionally charged point-like constituents represented by the single lines of Figure 1c. The interaction of the photon with the proton is now given by the sum of all possible interactions of the photon with the individual constituents, in direct analogy with the QED description of electron-electron scattering. The identification of the constituents with the quarks which had proved so successful in the classification of sub-atomic resonances paved the way for the emergence of what many feel to be the first viable theory of strong interactions, Quantum Chromodynamics or QCD[8][9].

It was against this background that a Columbia-Stony Brook collaboration at Brookhaven[1], while searching for the W boson in proton-uranium collisions, noticed an anomalously high background of oppositely charged muon pairs. As in the case of deep inelastic electron scattering this phenomenon found an explanation in terms of the parton
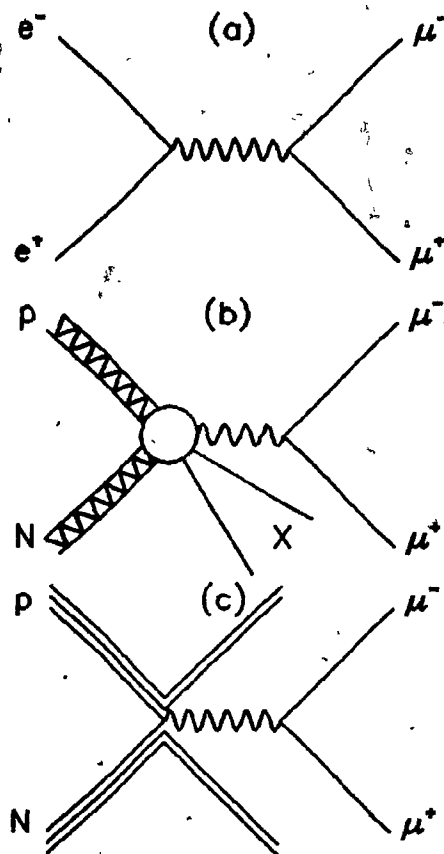
Figure 2 - Muon Pair Production

The top Feynman diagram represents electron-positron annihilation. The process is well described by QED in terms of the creation and decay of a single photon (shown as a wavy line). The middle diagram shows the general case of inclusive muon pair production. The bottom diagram shows the parton model picture of muon pair production. The proton and the nucleon are treated as sums of free constituents, and the cross section for the production of a massive photon is given by the sum of the cross sections for the annihilation of the constituents.

model, as shown in the Feynman diagrams of Figure 2. Figure 2a represents the annihilation of an electron-positron pair to create a pair of muons. As before, the point-like electrons and muons are described by quantum mechanical waves, represented by single lines in the diagram, and the interaction is well described if it is assumed that it is mediated by a single photon. The general case of the interaction of a proton and a nucleon with the associated production of a pair of muons is shown in Figure 2b. The unknown interaction between the proton and a nucleon is shown as a bubble at the proton-nucleon vertex. Because muons do not interact strongly, the process must be dominantly electromagnetic, as shown by the photon leaving the bubble and subseqently decaying to give two muons. In the parton model description of this process, as shown in Figure 2c, an analogy is drawn with the QED description of electron-positron annihilation, in the same way that an analogy was drawn between electron-electron scattering and inelastic electron-nucleon scattering. A constituent of the proton annihilates with a constituent of the nucleon to create an intermediate photon which subsequently decays into two muons. If the motion of the constituents inside the hadron is known, either from the solution of bound state wave equations, or from experimental measurements as in deep inelastic scattering, then the parton model gives explicit predictions for both the magnitude and shape of the spectrum of muon pairs. If the structure of the hadron is not known, as in the case of the pion, the inversion of the parton model expression for the cross section allows the motion of the constituents to be determined from the measured distributions.

This thesis presents the results of a measurment of the production of muon pairs in the collisions of 125 GeV/c antiprotons and pions with a

tungsten target. Antiproton-nucleon muon pair production is the best channel in which to compare experiment and theory, since this process is dominated by the annihilation of the constituents whose behaviour is most easily measured in inelastic scattering. The difficulties associated with producing a beam of antiprotons of sufficient intensity have inhibited the study of this process to date. A previous experiment at CERN[10] was able to achieve a comparable sample of muon pairs using a 150 GeV/c pion beam with a small antiproton component (≈ 2 percent). The high rates necessary to obtain this sample resulted in a large (≈ 25 percent) contamination of pion produced pairs, giving large systematic errors. Many experiments, however, have examined muon pairs produced by pions. The comparison of our pion cross sections with those of other experiments at different energies provides both a test of the scaling predictions of the parton model, and a valuable cross-check on the antiproton results.

The parton model and some of its implications for this experiment are discussed in the next chapter. The corrections required by perturbative QCD are also discussed. Subsequent chapters discuss the beam and the apparatus, the reconstruction of the kinematics of the muon pairs, the computer simulation of the apparatus, and the extraction of the cross sections and kinematic distributions. The final chapter presents our results and kinematic distributions and compares them to the parton model, leading order QCD calculations, and other experiments. The parton model is also used to extract the structure functions of the antiproton and the pion from the data.

CHAPTER 2

Theory

In the parton model, hadrons are treated as if they were just the sum of their constituents. The amplitude for electromagnetic interactions with hadrons is taken to be the incoherent sum of the amplitudes for electromagnetic interactions with the constituents. Interactions between the constituents and coherent effects are ignored. The cross section for inelastic scattering of a lepton from a hadron is given by the sum of the cross sections for the elastic scattering from the constituents weighted by structure functions describing the motion of the constituents inside of the hadron. The structure functions can be simply interpreted as the density of momentum carried by constituents with a fraction x of the momentum of the parent hadron.

In the parton model picture of muon pair production in hadron-hadron collisions first proposed by Drell and Yan[11][12] and conventionally

referred to as the Drell-Yan model, the cross section is given by the sum of the cross sections for electromagnetic constituent-constituent annihilation into a pair of muons weighted by the product of the relevant structure functions of the respective-hadrons. The structure functions are taken to be characteristic of the hadron rather than the process, so that the structure functions measured in inelastic scattering can be used to predict the cross section for muon pair production.

The parton model is often considered to be a zeroth order approximation to the underlying theory of strong interactions, currently believed to be Quantum Chromodynamics (QCD). In QCD the hadrons are bound states of fractionally charged fermions called quarks. A list of the quarks and the conventional assignment[13] of quark quantum numbers is given in Table 1. The quarks are also characterized by a quantum number conventionally called colour. Interactions between the quarks are mediated by field quanta called gluons which also carry colour. The quarks combine to form bound states in such a way that the net colour quantum number of any observable hadron is zero. The proton is a bound state of two u quarks and a d quark. The antiproton is made of two $\bar{u}$ quarks and a $\bar{d}$ quark. The neutron is a bound state of two d quarks and a u quark. The π^- is a bound state of a $\bar{u}$ and a d quark.

The bound state equations of QCD should give a complete description of the motion of the constituents within the hadrons, but a solution of them has thus far proved elusive. First order pertubative calculations have shown that although the size of the corrections to the parton model picture are large, the cross section for muon pair production can still be factored into products of process independent structure functions[14]. Questions

Table 1 - Quark Quantum Numbers

Quark	u	d	s	c	b	t
Baryon Number	1/3	1/3	1/3	1/3	1/3	1/3
Charge	-1/3	+2/3	-1/3	+2/3	-1/3	+2/3
Isospin Z	-1/2	+1/2	0	0	0	0
Strangeness	0	0	-1	0	0	0
Charm	0	0	0	+1	0	0
Bottom	0	0	0	0	+1	0
Top	0	0	0	0	0	+1

were raised as to whether proofs of factorization could be extended to all orders of perturbation theory[15] but further work[16][17] has verified that the cross section factorizes up to second order (two loop level).

The production of muon pairs and the Drell-Yan model have been reviewed extensively in the last several years. Lyons[18] and Stroynowski[19] review the production of both low mass and high mass muon and electron pairs, including the psi, ψ, and upsilon, T, resonances which can decay via this channel. Kenyon[20] specifically reviews the state of the Drell-Yan model. In addition, conference proceedings[21] and workshops[22] provide summaries of much of the recent progress in the field.

2.1 Drell-Yan Model

In the parton model picture, the cross section for the production of muon or electron pairs in hadron-hadron collisions is predicted absolutely once the structure functions of the hadrons are known from deep inelastic scattering.

The electromagnetic cross section for the annihilation of an electron and a positron into a pair of muons,

$$e^+ + e^- \rightarrow \mu^+ + \mu^-,$$

is given in the extreme relativistic limit using QED as

$$\frac{d\sigma}{d\Omega} = \frac{\alpha^2}{4s} [1+\cos^2\theta]$$

where

α is the electromagnetic coupling constant,

$s = (p_a + p_b)^2$ is the square of the centre of mass energy with p_a and p_b being the four momenta of the electron and positron respectively,

and

θ is the angle between the $e^+ - e^-$ axis and the $\mu^+ - \mu^-$ axis in the centre of mass frame.

Integrating over θ, the total cross section for production of a pair of muons is

$$\sigma = \frac{4\pi\alpha^2}{3s}.$$

Extending these considerations to the case of hadron-hadron collisions, the cross section for a point-like spin 1/2 parton of charge e_i with a fraction x_1 of the momentum p_a of one hadron to annihilate with a corresponding antiparton of momentum $x_2 p_b$ in the other hadron and create a pair of muons with momenta p_1 and p_2 and an invariant mass of

$$M^2 = (p_1+p_2)^2 = (x_1 p_a + x_2 p_b)^2 \approx x_1 x_2 s,$$

is

$$d^2\sigma = \frac{4\pi\alpha^2}{3M^2} e_i^2 q_i(x_1)\bar{q}_i(x_2) dx_1 dx_2$$

where

e_i is the parton charge in units of the electron charge, and

$q_i(x_1)dx_1$ and $\bar{q}_i(x_2)dx_2$ are the parton structure functions or the density of fractional momentum x, carried by quarks of type i.

The quark structure functions are defined in terms of the deep inelastic neutrino-proton scattering structure functions as

$$\sum_i [q_i + \bar{q}_i] = F_2^{\nu p}$$

and

$$\sum_i [q_i - \bar{q}_i] = x F_3^{\nu p}.$$

The structure functions used here are related to the commonly used parton distribution functions (the number density of quarks with fractional momentum x) by

$$q \text{ Structure} = xq \text{ Distribution}.$$

Summing over all partons in the hadrons, the cross section for muon pair production becomes

$$\frac{d^2\sigma}{dx_1 dx_2} = \frac{4\pi\alpha^2}{9sx_1^2 x_2^2} \sum_i e_i^2 q_i(x_1)\bar{q}_i(x_2).$$

The sum includes all parton types and an explicit factor of $1/3$ has been included to take into account the requirement that the annihilating quarks must have the same colour quantum number.

Rather than using x_1 and x_2, it is conventional to express the cross section in terms of the equivalent variables,

$$M^2 = x_1 x_2 s,$$

the invariant mass of the muon pair, and Feynman x, defined as

$$x_F = p_L/p_{Lmax},$$

the fraction of the maximum longitudinal momentum possible for a muon pair in the hadron-hadron centre of mass system. The invariant mass of the muon pair is often expressed in terms of the dimensionless ratio

$$\tau = M^2/s = x_1 x_2.$$

To a good approximation (neglecting terms of order $M^2_{Nucleon}/s$), p_{Lmax} can be taken to be

$$p_{Lmax} = \frac{\sqrt{s}}{2}(1-\tau).$$

Using this approximation, Feynman x becomes

$$x_F = \frac{2p_L}{\sqrt{s}(1-\tau)}.$$

Since the muon pair may be produced with appreciable transverse momentum — due to the intrinsic transverse momentum of the quarks or higher order effects ignored by the parton model — an additional kinematic variable is necessary to completely specify the motion of the muon pair. The third kinematic variable is conventionally taken to be p_T, the component of the muon pair's momentum perpendicular to the hadron-hadron axis in the hadronic centre of mass frame, as given by

$$\vec{p}_T = \vec{p}_a + \vec{p}_b - \vec{p}_L.$$

In terms of the variables M and x_F, the variables x_1 and x_2 become

$$x_1 = \frac{1}{2}[(x_F^2(1-\tau)^2+4\tau)^{1/2}+x_F(1-\tau)]$$

and

$$x_2 = \frac{1}{2}[(x_F^2(1-\tau)^2+4\tau)^{1/2}-x_F(1-\tau)]$$

and the cross section (integrated over p_T) becomes

$$\frac{d^2\sigma}{dMdx_F} = \frac{4\pi\alpha^2}{9M^3} \frac{2\tau(1-\tau)}{\sqrt{x_F^2(1-\tau)^2+4\tau}} \sum_i e_i^2 q_i(x_1)\bar{q}_i(x_2)$$

An immediate consequence of the parton model apparent from this equation is that the cross section $M^3\frac{d^2\sigma}{dMdx_F}$ scales, or depends only on M and s through the dimensionless ratio τ. Integrating over the same x_F region, the cross sections $M^3\frac{d\sigma}{dM}$ and $s^{3/2}\frac{d\sigma}{dM}$ should be functions of only τ and not M and s separately. Likewise the cross section $s \cdot \frac{d\sigma}{dx_F}$ should be independent of M and s if integrated over the same region in τ, allowing data at different beam energies to be compared.

2.2 Angular Variables

The variables M, x_F and p_T completely specify the motion of the rest frame of the muon pair with the exception of a trivial azimuthal angle about the hadron-hadron axis. Two additional variables are necessary to specify the motion of the individual muons with respect to the muon pair rest frame. These are typically taken to be θ, the polar angle, and ϕ, the azimuthal angle of the positive muon in the rest frame of the muon pair. Ideally the angles would be measured from the axis defined by the annihilating partons. Because the constituents are not necessarily collinear with the incoming hadrons, and because higher order effects can contribute to the cross section, the muon pair generally has some transverse momentum in the

hadron-hadron centre of mass system. When the particles are transformed to the muon pair rest frame, the beam and target momenta are not collinear and the parton-parton axis is unknown. In practice a convention is chosen such that the Z axis coincides with the hadron-hadron axis if the transverse momentum of the muon pair is zero.

The angles are shown schematically in Figure 3. Working in the rest frame of the muon pair, the beam and target momenta define a plane, conventionally taken to be the X-Z plane. The Y-axis is taken to be the unit normal to the plane in the direction of $\vec{p}_a \times \vec{p}_b$. The direction of the Z axis depends on a choice of convention. Two choices commonly used are the Gottfreid-Jackson[23] and the Collins-Soper frames[24]. The angle between two hadrons in the muon pair rest frame depends only on the hadronic variables, M, x_F and p_T. If we call the angle between the Z axis and the beam momentum α, then the Gottfreid-Jackson frame corresponds to a choice for α of

$$\alpha_{G-J} = 0$$

whereas the Collins-Soper frame corresponds to a choice for α of

$$\alpha_{C-S} = (\pi - \theta_H)/2$$

The Collins-Soper frame represents an attempt to take the intrinsic transverse momenta of the partons into account on the average under the assumption that the transverse momentum distributions of partons in the beam and target particles are the same.

Lam and Tung[25] have shown that if the process is mediated by a single photon, then the distribution of muons in the rest frame of the pair must be of the form

$$\frac{1}{\sigma}\frac{d\sigma}{d\Omega} = \frac{3}{8\pi}\left[W_T(1+\cos^2\theta) + W_L(1-\cos^2\theta) + \right.$$

$$\left. W_\Delta \sin 2\theta \cdot \cos\phi + W_{\Delta\Delta}\sin^2\theta \cdot \cos 2\phi\right]/[2W_T + W_L] .$$
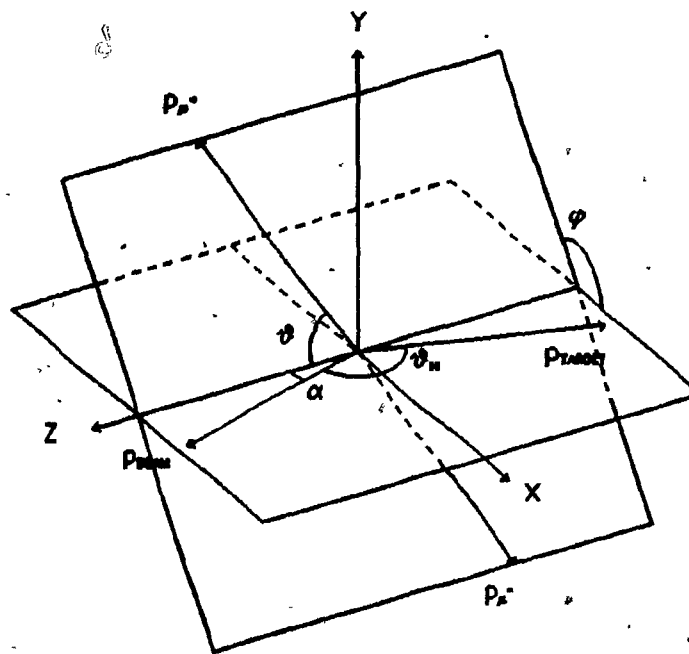
Figure 3 - Angular Variables

The angular variables are defined in the rest frame of the muon pair. The beam and target particle momenta define the X-Z plane. The Y axis is defined by the normal to the X-Z plane. The choice of Z axis depends on the convention chosen as discussed in the text. The angles θ and ϕ are the polar and azimuthal angles with respect to the Z axis.

where W_T, W_L, W_Δ, and $W_{\Delta\Delta}$ depend on the nature of the constituents. In the parton model picture, the angular distribution of muons in the rest frame of the virtual photon should be

$$\frac{1}{\sigma}\frac{d\sigma}{d\Omega} = \frac{3}{8}[1+\cos^2\theta],$$

and independent of ϕ, if the process is the result of the electomagnetic annihilation of point-like spin 1/2 constituents. A first order QCD calculation by Collins[26] shows that for interactions dominated by valence-valence subprocesses the terms other than that involving

$$1+\cos^2\theta$$

should be small.

2.3 Quantum Chromodynamics

Perturbative corrections to the Drell-Yan model can be calculated using Quantum Chromodynamics. Subprocesses such as those shown in Figure 4 can produce a massive photon which decays to a muon pair. In the impulse approximation, the cross sections for the subprocesses are calculated assuming that the quarks and gluons are free. The cross sections are convoluted with the quark and gluon structure functions of the beam and target particles. Calculations of the corrections to first order contain both infrared and mass singularities. The infrared singularities are handled as in Quantum Electrodynamics.

Politzer[27] pointed out that at the one loop level, the mass singularities are similar to the singularities that arise in the one loop corrections to deep inelastic scattering. In deep inelastic scattering, the logarithmic singularities can be absorbed into the structure functions at a particular value of Q^2 by defining an unobservable bare structure function
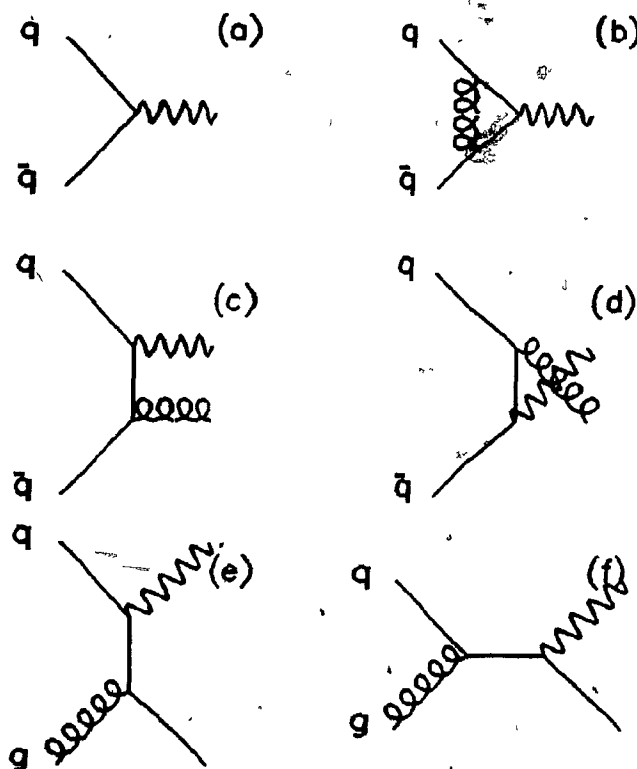
Figure 4 - QCD Annihilation and Compton Processes

Higher order QCD subprocess can also contribute to muon pair production. The Drell-Yan subprocess is shown in (a). A quark (single line) in the beam particle annihilates with an antiquark in the target particle to create a massive photon (wavy line), which can decay to give a pair of muons (not shown). QCD vertex corrections, such as (b), lead to large constant corrections. Annihilation diagrams such as (c) and (d), involving a gluon (looped line) in the final state, and Compton diagrams such as (e) and (f), involving a gluon in the initial state, can give the muon pair appreciable transverse momentum.

q_0, which is also singular, in such a way as to cancel the singularities of the correction term. The observable structure functions are now finite, but depend logarithmically on Q^2. The similarities of the one loop corrections suggested that the Drell-Yan cross section can still be expressed in terms of deep inelastic structure functions if the structure functions depend explicity on Q^2, that is,

$q(x) \rightarrow q(x,Q^2)$,

where Q^2 is identified as M^2.

Calculations in the leading log approximation[28] and to first order in the stong coupling constant, α_s[29][30], have confirmed that the singularites can be cancelled in this way. The size of the first order corrections has been shown to be of the same order as the parton model cross sections, that is,

$$\frac{d^2\sigma}{dMdx_F} = K \left(\frac{d^2\sigma}{dMdx_F}\right)_{Parton}$$

where

$$K = 1 + \frac{\alpha_s}{2\pi}\frac{4\pi^2}{3}$$

and does not depend strongly on M or x_F.

The size of the first order terms has raised concerns about the validity of the perturbative approach. It has been conjectured, on the basis of an analogy with QED, that the first order corrections are the leading term in the series expansion of an exponential[31],

$$K \rightarrow \exp[\frac{\alpha_s}{2\pi}\frac{4\pi^2}{3}].$$

Calculations up to order α_s^2 included (two loop level), have confirmed[32][33] that corrections to the Drell-Yan process lead to a well-defined part of the cross section giving the first three terms in a series expansion of

$$\exp[\frac{\alpha_s}{2\pi}\frac{4\pi^2}{3}].$$

Measurements of the cross section in proton-nucleon and pion-nucleon collisions seem to confirm that the measured cross sections are in fact about twice as large as the parton model would predict, but in both cases the calculations are dominated by terms involving structure functions which are not well known. Proton-nucleon muon pair production is dominated by the annihilation of valence quarks in the beam particle with the sea quarks of the target particle. Inelastic scattering experiments are able to measure the distributions of the valence quarks but the extraction of the sea quark distributions is sensitive to the assumptions made.

The pion structure functions are not accesible to electron scattering experiments. Muon and electron pair production may provide the best way to measure them. Because the normalization of the cross sections is very sensitive to the behaviour of the structure functions at low x, a region which is masked by resonances and other backgrounds, the normalization of the pion-nucleon Drell-Yan cross section is subject to large systematic uncertainties.

Measurements of the antiproton-nucleon cross section for muon pair production provides the best way to measure the K factor. The process is dominated by the annihilation of valence anti-quarks in the antiproton with valence quarks in the nucleon. The antiproton valence structure functions must be the same as the proton structure functions because of particle-antiparticle symmetry. and the nucleon valence structure functions are well measured in electron, muon and neutrino scattering experiments over large ranges of x and Q^2.

2.4 Nuclear Dependence

The question of the nuclear dependence of the cross sections is one of considerable practical importance but difficult to treat theoretically. Experiments are forced to use heavy nuclear targets in order to achieve an acceptable event rate and must extrapolate to obtain a cross section per nucleon. Nuclear effects are inherently nonperturbative, making them difficult, if not impossible, to calculate. The nuclear dependence is usually empirically parameterized as

$$\sigma = \sigma_0 A^\alpha$$

and measurements using several nuclear targets are fit to obtain α and σ_0. If the nuclei are not isoscalar, σ_0 will be a function of Z/A, the ratio of the atomic number and the atomic mass.

It can be argued that a strong process will involve interactions at the surface of the nucleus and should depend on A as

$$\sigma = \sigma_0 A^{2/3}$$

whereas a weaker probe like the photon will have an A dependence proportional to the volume of the nucleus and

$$\sigma = \sigma_0 A^1.$$

Currently accepted values[34] for α are consistent with

$$\alpha_{DY} = 1.0.$$

Recent results from muon scattering experiments at CERN[35] and a reanalysis of electron scattering results at SLAC[36][37] have shown that the structure functions of nucleons bound in iron and aluminum nuclei are not the same as the quasi-free nucleons of deuterium. Since most of the

structure function measurements use iron, which should be similar to our tungsten target, and since our experiment does not have sufficient data to see the difference between the structure function of the free antiproton and the nucleons of a tungsten nucleus, we have ignored these differences in our analysis.

2.5 Previous Experiments

Muon pairs were first observed at Brookhaven in 1970 by a Brookhaven-Columbia-Stony Brook (BCS)[1] collaboration using a proton beam and a uranium target to look for W bosons. A Columbia-Fermilab-Stony Brook (CFS)[38] collaboration at Fermilab, using a double arm spectrometer studied both muon and electron pair production in proton-nucleon collisions. Work by the same group led to the discovery of the upsilon family of resonances. A Chicago-Illinois-Princeton (CIP)[39] collaboration working at Fermilab at about the same time made the first attempt to extract the pion structure function[40]. Measurements of the π^+/π^- cross section ratio from nuclear targets by this group, provided confirmation of the electomagnetic nature of the production process.

Several experiments at CERN have published important results in the last several years. The Omega[41][42][43] collaboration has made measurements of the cross section for muon pair production at 40 GeV/c, with pion, kaon, proton and antiproton beams. As well as demonstrating the beam dependence of the cross section, comparison of the Omega data with experiments at higher energies provides one of the best examples of the type of scaling behaviour expected from the Drell-Yan model. The GOLIATH[44] collaboration measured muon and electron pair production rates in

pion-nucleon collisions at beam energies of 150 and 175 GeV/c. The NA3[45][46][47] collaboration at CERN has made extensive measurements of muon pair cross sections with proton, pion, and kaon beams incident on a platinum target as well as the first antiproton[10] results. Measurements by the NA3 group of the π^+/π^- cross section ratio for tungsten and hydrogen targets[48], measurements of the angular distributions of the muon pairs[49] and measurements of the A dependence of the muon pair cross section[50] have confirmed many of the features expected from the Drell-Yan model. The NA10[51] experiment has published preliminary results using an intense pion beam to produce muon pairs in a tungsten target. Initial results from this experiment[52] provide confirmation of the linear A dependence measured by the NA3 collaboration. Detailed comparisons of our data to data obtained by the NA3, CIP, Goliath and Omega collaborations will be made in the final chapter.

Two experiments running currently at Fermilab are also studying muon pair production. An extension of the CFS collaboration[53] is looking at the production of high mass electron pairs in proton-nucleon collisions at beam momenta of up to 1 TeV/c with a new spectrometer in the Meson Area. Members of the CIP collaboration[54] are examining muon pairs produced in pion-nucleon collisions at very high x_1 across the range of cosθ, using an apparatus in the High Intensity Area of the Proton line, upstream of the spectrometer used for this experiment.

CHAPTER 3

Apparatus.

The experiment described here was located in the high intensity area of the west proton beam line at Fermilab, in Batavia, Illinois, and took data in the spring of 1981 and the winter of 1982. The apparatus used was designed to look for events with one beam particle hitting the target, and a pair of muons leaving it. Systems of Cerenkov and scintillation counters with good time resolution provided fast signals to trigger the apparatus and reject accidental coincidences and background. Proportional and drift chambers with good spatial resolution provided precise measurements of points along the particle trajectories so that the events could later be reconstructed offline.

The apparatus used for the experiment was a closed geometry magnetic spectrometer, shown schematically in Figure 5. Tungsten, copper, and beryllium targets were exposed to a beam of 125 GeV/c pions and antiprotons.
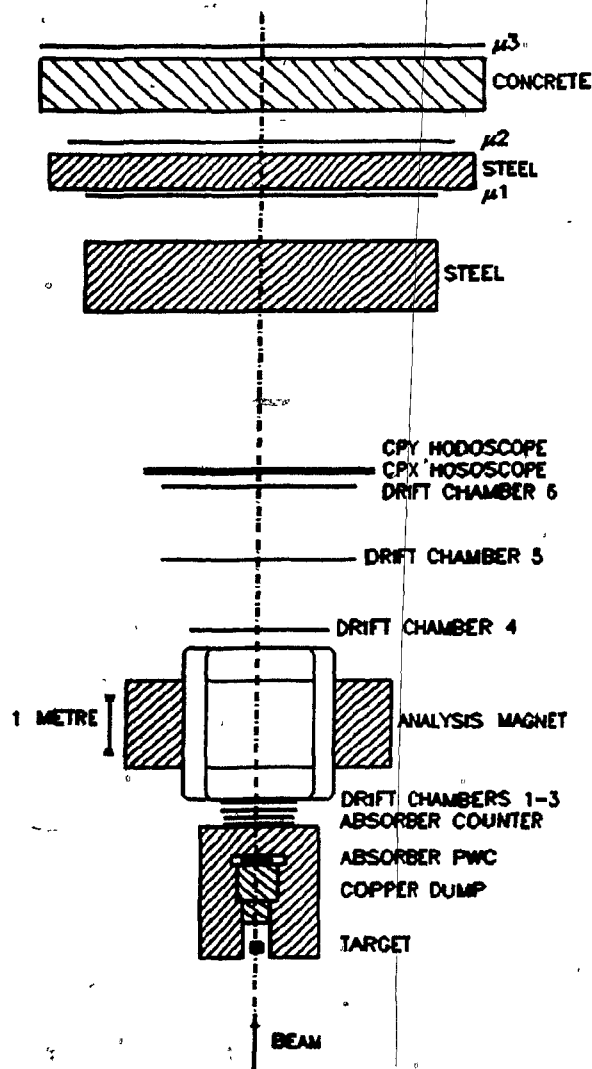
Figure 5 – Plan View of the E537 Spectrometer

The E537 apparatus is a closed geometry magnetic spectrometer and is descibed in detail in the text.

Hadrons from the interactions were filtered out by a copper beam dump. Track coordinates were measured 2/3 of the way through the beam dump by two planes of proportional wires. Immediately downstream of the dump a scintillation counter designed to detect muons produced at a large angle with respect to the beam provided a high mass bias for the fast trigger. Trajectories were also measured downstream of the dump by 9 planes of drift chambers. A large conventional dipole magnet deflected charged particles to permit a momentum measurement. Particles were tracked downstream of the magnet by 9 planes of drift chambers and 2 scintillation counter hodoscopes. Muons were identified by requiring them to pass through walls of steel and concrete interleaved with scintillation counter hodoscopes. Muons required a momentum of 6 GeV/c to penetrate to the final hodoscope. Signals from the counters were combined to produce a fast trigger signal when two muons were detected. Low mass events were rejected by a fast trigger processor, and information from the counters and chamber wires was written to magnetic tape so that the kinematic variables of the muon pair could be reconstructed offline.

A sample of 4.0×10^5 dimuon events with mass greater than 2 GeV/c was collected in a running period of 13 weeks.

3.1 Accelerator

The accelerator at the Fermilab site is a 400 GeV proton synchrotron[55]. Protons from a hydrogen gas source are given a kinetic energy of 750 KeV by a Cockroft-Walton electrostatic accelerator. A 200 MeV linac injects the protons into an 8 GeV booster syncrotron from which they enter the main ring. One burst of up to 3.0×10^{13} protons is accelerated.

every 9 to 15 seconds. The beam is extracted in a 1 second spill and split three ways to the Meson, Neutrino and Proton lines. The beam particles are not uniformly distributed thoughout the spill but cluster in buckets spaced 19 ns apart. The interbucket spacing is characteristic of the radio frequency voltage used in the main accelerator. Timing signals from the main control room allow the experiment to be synchronized with the accelerator.

3.2 Antiproton Beam

A schematic layout of the beam line elements is shown in Figure 6. A neutral beam of lambdas and kaons was produced by 400 GeV/c protons striking a 15 cm beryllium target[56][57]. Charged secondary particles were removed from the beam by a dipole sweeping magnet 2.3m downstream of the primary target. Pions and antiprotons from the decay in flight of the neutrals were gathered by a flux collecting quadrupole triplet and transported to the experimental hall by a beam line of conventional dipoles and quadrupoles. A dipole and collimator selected beam particles with a momentum of 125GeV/c and eliminated the positive decay products. A FODO channel collected the particles and transported them to the final focussing triplet. Electrons were removed from the beam by a 2.5 cm thick lead absorber.

The resulting beam consisted of 79 percent pions and 21 percent antiprotons, with a 10 percent momentum bite FWHM. The angular and spatial divergences of the beam at the experimental target were 1 mr and 2.5 cm respectively. To reduce uncertainties due to the large phase space of the beam, the momentum and trajectory of each individual beam particle was tagged in the experimental hall by a system of proportional wire chambers

EXPERIMENTAL TARGET

TARGETING TRIPLET

FODO CHANNEL

100 METRES

MOMENTUM SLIT

MOMENTUM DISPERSING
BEND

FLUX GATHERING TRIPLET

SWEEPING MAGNET
Be TARGET
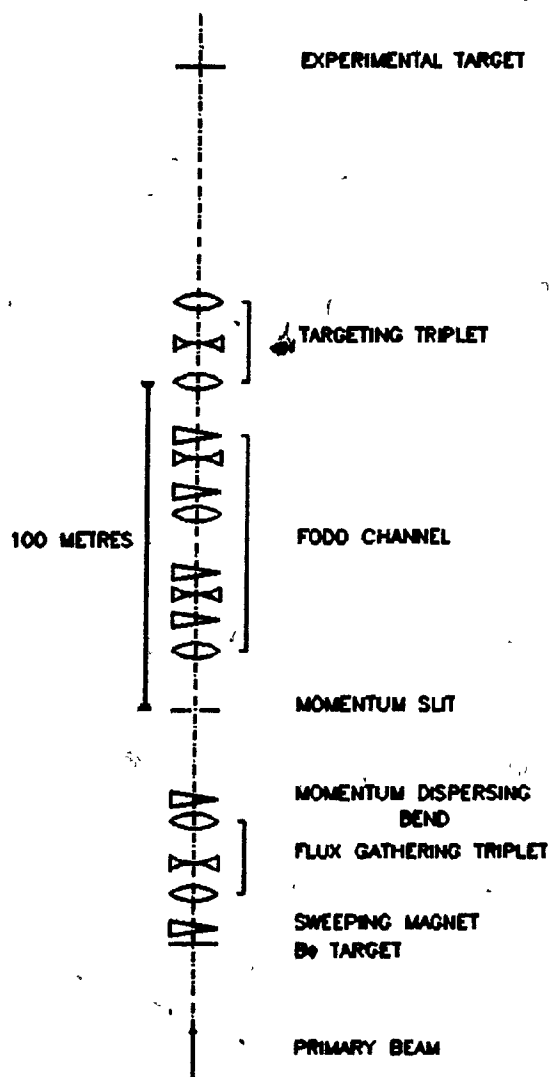
PRIMARY BEAM

Figure 6 - High Intensity Area Beam Line

A primary beam of 400 GeV/c protons strikes the beryllium target. Charged secondaries are swept from the beam and the neutral secondaries allowed to decay. A dipole and slit select 125 GeV/c pions and antiprotons from the decay products and a string of conventional dipoles and quadrupoles transports them to the experimental target.

and bending magnets described in the next section.

The primary beam flux was monitored by two Secondary Emission Monitors (SEM's)[58] upstream of the primary target. Beam position and spot size were monitored along the beam line and in the experimental hall by Segmented Wire Ionization Chambers (SWIC's)[59][60] tied into the Fermilab beam line control system. A primary beam flux of 7×10^{12} protons/spill typically resulted in a secondary beam flux of 12×10^6 particles/spill.

The beam was surrounded by a halo of muons produced by decaying pions and energetic secondary particles not removed from the neutral beam. Because the accidental coincidence between halo particles and a single muon produced by the beam could mimic the signature of a muon pair, thus increasing the trigger rate and contaminating the data sample, steps were taken to suppress as much of the halo as possible. Muon spoiler magnets upstream of the experimental hall swept off axis particles away from the beam region. The veto counters used to inhibit the apparatus when a halo particle was present are discussed in a later section. Strict vertex requirements, imposed on the events offline to suppress any remaining contamination of the data sample, are discussed in the next chapter.

3.3 Beam Tagging

The momentum and trajectory of each beam particle was measured with a beam telescope consisting of 9 planes of proportional chambers, three Y hodoscopes and two small dipole magnets. Beam particles were identified by two Cerenkov counters which will be discussed in the next section.

A plan view of the beam tagging system showing the relative locations of the elements is given in Figure 7. The first beam station, BY1, which consisted of three planes of proportional chambers and a hodoscope followed the first Cerenkov counter, CS1. A second beam station, BY2, was placed 3.95 meters downstream of the second Cerenkov counter, CS2. A third beam chamber station, BY3, followed 3.43 m upstream of the experimental target. The pair of magnets between CS2 and the second beam station gave each beam particle a vertical momentum increment of 0.319 GeV/c, allowing a beam particle with a momentum of 125 GeV/c to be measured to an accuracy of 1 GeV/c.

Each beam station had three planes of proportional wire chambers, with the wires oriented along the U, V and Y directions. The Y coordinate was taken in the vertical direction with the U and V directions defined by clockwise rotations about the Z axis (beam direction) of 240 and 120 degrees from Y respectively. Each station had an associated scintillator hodoscope which measured the Y coordinate.

All beam chamber sense wire planes consisted of 128 wires of 12.5 μ diameter spaced 1 mm apart. Cathode planes were made using 25.4 μ thick aluminum foil. The chambers were operated using a gas mixture of 25 percent isobutane, 5 percent methylal, 0.5 percent freon with the balance being argon. A discrete component amplifier followed by a high speed ECL comparator provided a differential time over threshold output[61].

Each hodoscope consisted of a 15.24 cm diameter disk of 0.6 cm thick NE110 plastic scintillator[62] segmented horizontally into eight parts. Each segment was optically coupled to a 12 stage Amperex 56AVP

TUNGSTEN TARGET

BEAM STATION BY3

VACCUUM PIPE

BEAM STATION BY2
DIPOLE MAGNETS

CERENKOV TANK CS2

10 METRES

BEAM STATION BY1

CERENKOV TANK CS1
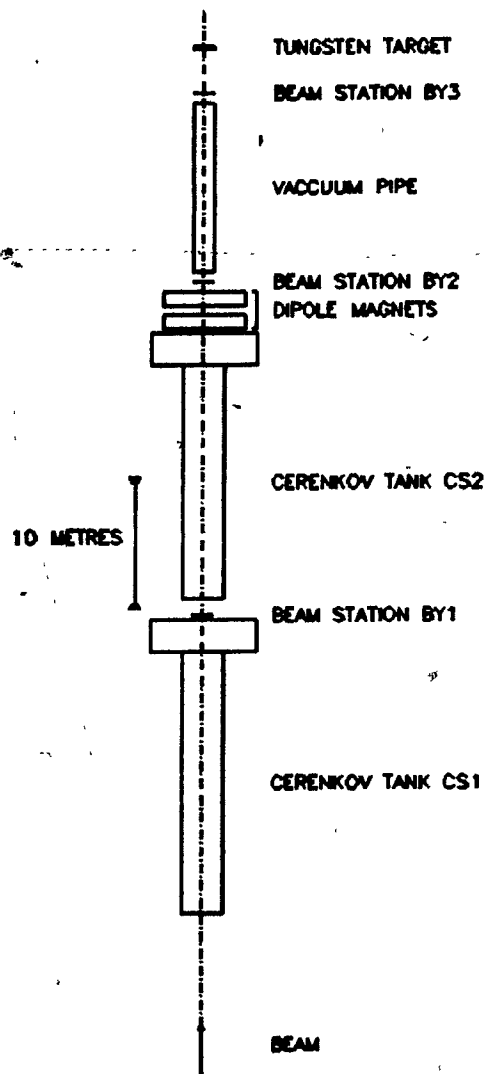
BEAM

Figure 7 - Beam Tagging System

Individual beam particles were tagged by a system of Cerenkov counters, scintillation counter hodoscopes, and proportional wire chambers, as discussed in the text.

photomultiplier[63] with a resistive voltage divider base. Zener diodes were used to clamp the final two dynode voltages. Photomultiplier outputs were clipped using a 3 ns stub of 50 Ω coaxial cable terminated in 25 Ω to allow the highest possible counting rates. The widths of the hodoscope segments were chosen to roughly equalize the individual counting rates.

The proportional chambers gave an accurate measurement of the position of the beam particle trajectory but were sensitive for a period of 60 ns, which included beam particles in three separate accelerator RF buckets. The beam hodoscope elements were designed to have a resolving time of 10 ns, and were capable of distinguishing between beam particles in successive RF buckets. Discriminator signals from the beam hodoscopes were recorded with each event so that tracks not associated with the beam particle causing the trigger could be rejected by the offline analysis.

3.4 Cerenkov Counters

The type of each incident beam particle was established by two differential gas Cerenkov counters. Both counters were filled with a mixture of 80 percent helium and 20 percent nitrogen. The fraction of beam particles counted by the first Cerenkov counter as a function of gas pressure is shown in Figure 8. Between pressures of 3 and 6 PSIA the counter is below the antiproton Cerenkov threshold and counts only pions, which constitute 80 percent of the beam. Between 10 and 12 PSIA, Cerenkov light from the pions is at the wrong angle to hit the photomultiplier and the counter is only sensitive to antiprotons, the remaining 20 percent of the beam. The first counter, CS1, was set to count antiprotons at 10.5 PSIA while the second (CS2) was set at 3.5 PSIA to identify pions.
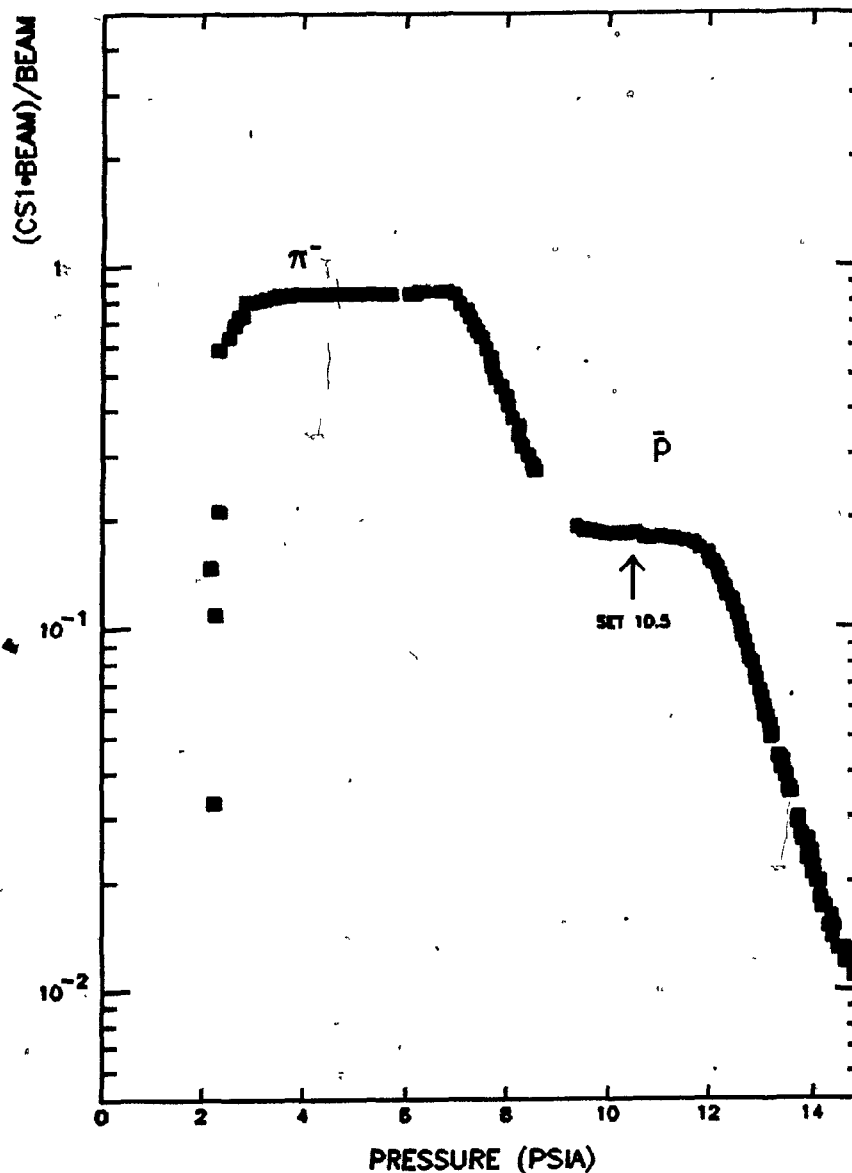
Figure 8 - CS1 Cerenkov Counter Pressure Curve

The vertical axis shows the fraction of the beam particles detected by the first Cerenkov counter. Between gas pressures of 3 and 6 psia the counter is below the antiproton Cerenkov threshold, and counts only pions. Above 10 psia the counter is not sensitive to light in the pion Cerenkov cone and the counter detects only antiprotons.

Cerenkov light produced in the 22 m long counters was reflected by a 33 cm diameter plastic mirror onto an RCA 31000M[64] photomultiplier tube through a 7.62 cm diameter quartz window. The mirrors were made of aluminized lucite with a 4.572 m radius of curvature and a 2.286 m focal length. Annular masks on the photomultiplier windows restricted the sensitivity of the counters to a cone of light with half angle between 4.4 mr and 7.9 mr in the case of CS1 and 5.7 mr to 7.6 mr in the case of CS2.

The counters were designed to be able to distinguish between beam particles in successive RF buckets. Transistorized bases[65] permitted counting rates in excess of 3.0×10^7 particles/second. Photomultiplier signals were clipped by a 3 ns stub of 50 Ω cable terminated in 25 Ω. The 25 Ω termination damped the size of the pulse reflected by the stub and gave the counters an output pulse of less than 6 ns duration with no ringing or overshoot. Signals were amplified by Lecroy VV100B 10 × amplifiers[66] prior to discrimination to reduce the average anode currents in the tubes. The average number of photoelectrons per particle ranged from 7-10 and the discriminators were set to trigger at 2 or more.

Cerenkov counter efficiency was monitored during the data taking by comparing the number of beam particles counted by the Cerenkov counters to the number of beam particles counted by the beam telescope, using

CERENTOT = [(CS1·BEAM) + (CS2·BEAM) − (CS1·CS2·BEAM)]/BEAM;

where

(CS1·BEAM) is the number of coincidences between signals from the first Cerenkov counter (CS1) and the beam telescope (BEAM), that is, the number of beam particles counted by the antiproton Cerenkov counter,

(CS2·BEAM) is the number of beam particles counted by the pion Cerenkov counter,

(CS1·CS2·BEAM) is the number of particles counted by both Cerenkov counters, and

BEAM is the number of beam particles counted by the beam telescope as discussed in the next section.

CERENTOT was always 0.995, indicating that the inefficiency of the counters was less than 1 percent. Because some RF buckets contained more than one particle, and the antiproton counter operated far above the threshold for pions, the large angular dispersion of the beam caused a 5 to 10 percent contamination of the antiproton signal by pions. Rejecting beam particles which counted in both CS1 and CS2 reduced this contamination to 0.1 percent.

The discriminated output signals from the two counters were used in the fast trigger logic to define PBAR and PION signals, which indicated that a single antiproton or that a single pion had traversed the beam telescope. These signals are discussed further in the next section. The pulse heights of both counters were measured and recorded for each event, so that the counter performance could be studied offline.

3.5 Beam Tagging Logic

Standard NIM[67] logic modules were used to form a BEAM signal from the discriminated outputs of the beam hodoscope counters. The BEAM signal was combined with signals from the Cerenkov counters to indicate the presence of a beam particle to the fast trigger logic. A simplified schematic diagram of the beam logic is shown in Figure 9. The logical OR of the signals from the counters in the first beam hodoscope, BY1-1 through BY1-8, was used to
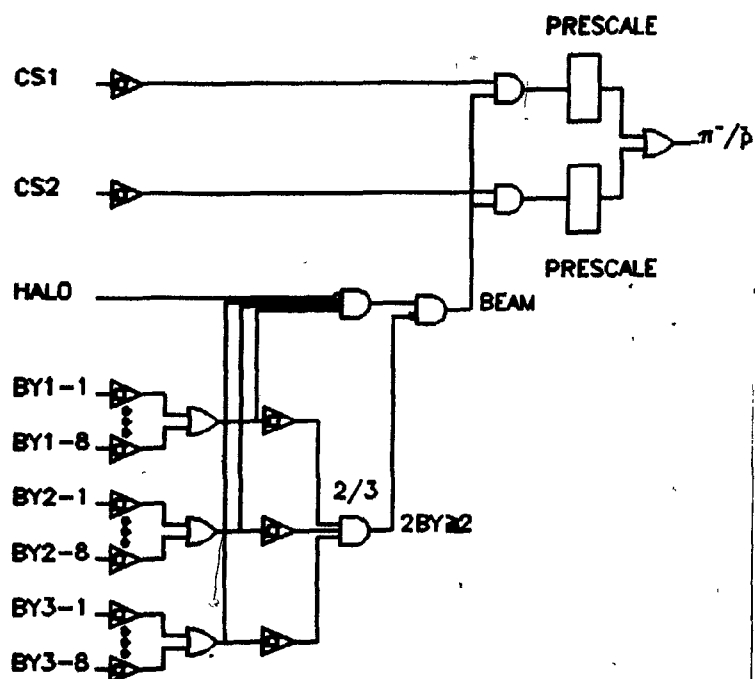
Figure 9 - Beam Logic

Photomultipler signals from the beam hodoscope elements and the Cerenkov counters were combined to form a $\pi^-/\bar{p}$ signal indicating that a single pion or antiproton had travelled through the beam telescope.

define a signal, BY1, which indicated that a beam particle had passed through the first beam station. Signals from the counters in the second and third beam hodoscopes were similarly used to define the signals BY2 and BY3. The discriminated signals from all hodoscope elements were recorded for each event.

To indicate when more than one beam particle had travelled through the beam telescope at the same time, the linear sums of the logical signals from the counters in each of the beam stations were rediscriminated to define the signals BY1$\geq$2, BY2$\geq$2 and BY3$\geq$2 if two or more of the counters in the respective hodoscopes had been hit. These signals were combined to give a veto signal, 2BY$\geq$2, if at least 2 out of 3 of the beam hodoscopes had more than 2 elements hit.

A BEAM signal was defined as the coincidence between the BY1, BY2 and BY3 signals from the beam hodoscopes, the anticoincidence of the 2BY$\geq$2 veto signal, and the anticoincidence of a HALO signal formed from the outputs of the halo counters as described in the next section, that is,

$$\text{BEAM} = \text{BY1} \cdot \text{BY2} \cdot \text{BY3} \cdot \overline{\text{2BY} \geq 2} \cdot \overline{\text{HALO}}.$$

The beam signal was .TRUE. if at least one counter was hit in each of the three beam stations, at least two of the three beam stations had only one counter hit, and none of the possible combinations of halo counters were hit. This signal indicated to the fast logic that one, and only one, beam particle had passed through the beam telescope, and that there were no halo particles present.

The logical signals PBAR and PION were defined if there were both a beam particle and a signal from the corresponding Cerenkov counter as

$$\text{PBAR} = \text{CS1} \cdot \text{BEAM} \cdot \overline{(\text{CS1} \cdot \text{CS2})},$$

and

PION = CS2 · BEAM · $\overline{(\text{CS1·CS2})}$,

where CS1 and CS2 were the discriminated signals from the Cerenkov counters described in the last section.

The PBAR and PION signals were prescaled separately and then combined to give a $\pi^-/\bar{p}$ signal which indicated the presence of a single identified beam particle to the fast logic. The antiproton prescaler was always set to count for each event but the pion prescaler was set to count once for every 1 to 4 events depending on overall trigger rate and beam conditions.

3.6 Veto Counters

Muons in the halo around the beam could combine with debris from interactions of the beam in the target and the dump to mimic the signature of a high mass muon pair. To reduce the effects of beam halo on the trigger rate, vertical (VX) and horizontal (VY) counters positioned around the beam axis as shown in Figure 10, were used to define a HALO signal which inhibited the apparatus during the presence of beam halo.

The counters were constructed of 1 cm thick NE114 plastic scintillator[62] and instrumented with Amperex 2212B photomultipliers[63]. Discriminated signals from an inner array of eight 73.66 cm × 12.7 cm and twelve 147.3 cm × 25.4 cm counters in the VX array were combined to form a VX signal as shown in Figure 11. A VY signal was formed with the OR of the discriminated signals from the eight 101.6 cm × 12.7 cm and eight 152.4 cm × 25.4 cm counters in the VY array. A VI signal formed from the AND of the VX and the VY signals indicated that a particle had passed
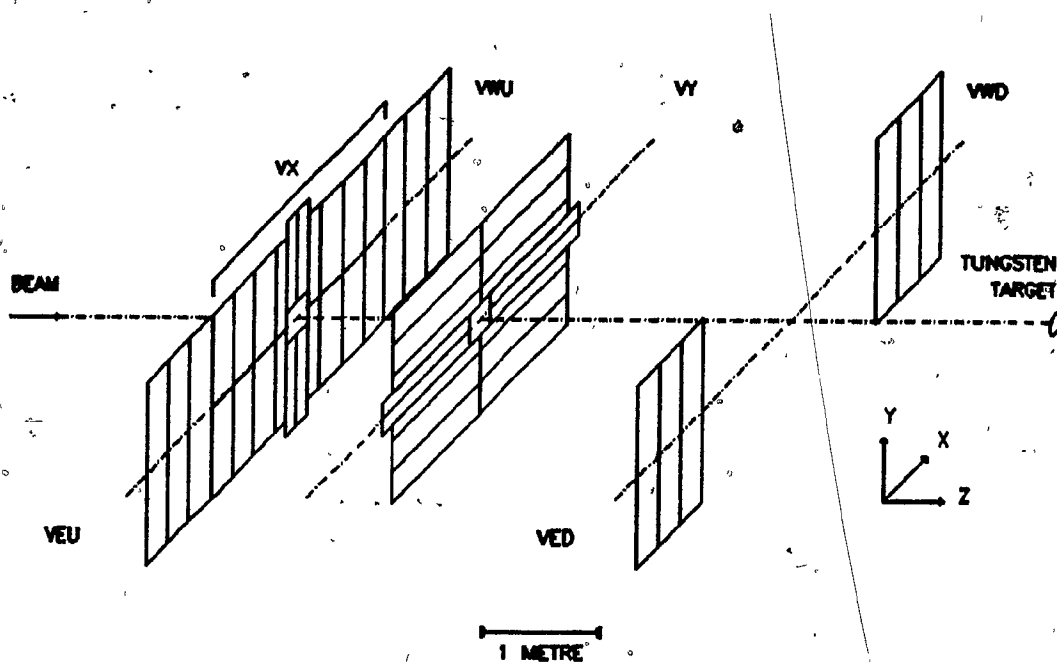
Figure 10.- Veto Counters

Arrays of scintillation counters around the beam indicated the presence of halo particles to the fast logic. Signals from the counters were combined to form a HALO signal used as a veto in the trigger.
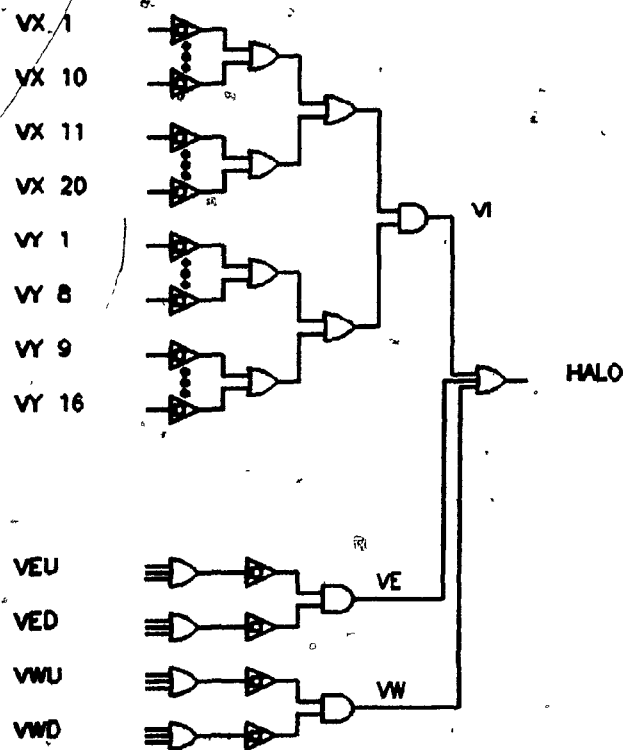
Figure 11 - Veto Counter Logic

This simplified schematic shows the combinations of veto counters used to form the HALO signal. A HALO signal was formed if a particle passed through both the VX array of counters and the VY bank of counters, if a particle passed through both VE arrays, or if a particle passed through both VW arrays.

through both of the inner arrays of halo counters. Central counters in both the VX and VY arrays were retracted from the beam axis to leave a 25.4 cm square beam hole.

An array of three 147.3 cm × 25.4 cm counters, VEU, covered the east side of the apparatus at the same location along the beam axis as the VX counters. The logical OR of the signals from these counters was combined with the logical OR of signals from an identical array of counters, VED, 3.1 m downstream but at the same position relative to the beam axis. A VW signal was formed from the outputs of two identical arrays, VWU and VWD, on the west side of the apparatus.

A HALO signal was defined as the logical OR of the VI, VE and VW signals indicating that a particle had passed through both of the innner arrays or either pair of the outer arrays on opposite sides of the apparatus. The HALO signal was used to veto the BEAM signal so that beam particles accompanied by a halo muon were ignored by the apparatus. Typically 4 percent of the beam particles were vetoed, but the trigger rate was reduced by a factor of 4, depending on the beam tune.

3.7 Target

Data was taken with three different nuclear targets, tungsten, copper and beryllium, to investigate the A dependence of the cross section. Initially all targets were chosen to be 1.0 absorption lengths for incident antiprotons, and were machined as 15.24 cm diameter cylinders. A 1.5 interaction length tungsten target was used during the 1982 run. A 0.4 interaction length tungsten target was also used for a fraction of the 1982

run to estimate the effects of reinteraction. The physical lengths and densities of all the targets used are listed in Table 2. The 1.0 interaction length targets were each divided into two segments and separated in such a way as to minimize any difference in acceptance between the various nuclear elements. Counters were placed between the segments to identify in which segment the interaction took place as an aid to the reconstruction programmes. The three segmented nuclear targets were mounted on a remote manipulator and interchanged regularly during the run to minimize any possible systematic effects.

The bulk of the data was taken with the tungsten target, however, to maximize the overall event rate.

3.8 Target Counters

The target counters consisted of 15.24 cm diameter disks of 0.635 cm thick plastic scintillator coupled to Amperex 56AVP photomultipliers[63] with 60 cm long lucite light guides. As with the beam and Cerenkov counters, the signals from the target counter photomultipliers were clipped and damped in an attempt to achieve the highest possible counting rate consistent with the conflicting requirements of high gain and wide dynamic range. The counters were mounted at the base of the target manipulator with the light guide holding the scintillator in the beam line so as not to interfere with the movement of the targets. One counter, T6, was mounted between the two segments and a second, T7, was mounted in the gap between the downstream target segment and the face of the absorber. Signal amplitudes from the target counters were recorded by Lecroy 2249A 12 channel ADC's[66] for use by the reconstruction programmes.

Table 2 - Target Densities and Lengths

	BE	CU	W	THICK W	THIN W
Density (gm/cm³)					
	.18600E+01	.89600E+01	.18500E+02	.18500E+02	.18500E+02
Target Length (cm)					
	.41240E+02	.15020E+02	.98090E+01	.14710E+02	.40870E+01
Absorption Length (cm)					
Pbar	.40420E+02	.14970E+02	.98245E+01	.98245E+01	.98245E+01
Pion	.58125E+02	.19259E+02	.11925E+02	.11925E+02	.11925E+02
Target Length (Absorption Lengths)					
Pbar	.10203E+01	.10033E+01	.99842E+00	.14973E+01	.41600E+00
Pion	.70951E+00	.77988E+00	.82253E+00	.12335E+01	.34271E+00
Effective Length (cm)					
Pbar	.25849E+02	.94813E+01	.62046E+01	.76264E+01	.33435E+01
Pion	.29534E+02	.10430E+02	.66864E+01	.84519E+01	.34603E+01

3.9 Beam Dump

Hadrons from interactions in the target and beam particles that did not interact were absorbed by a beam dump downstream of the target. A copper core of twelve 12.7 cm thick slabs covered the full acceptance of the spectrometer, giving a total thickness of 8 absorption lengths for 125 GeV/c pions. Copper was chosen for its relatively high density and acceptable ratio of radiation length to absorption length. Steel shielding on either side of the copper absorber minimized leakage from the sides and helped to attenuate off axis beam halo.

3.10 Absorber Chamber

Two planes of proportional wires were located approximately two thirds of the way through the dump to aid in the vertex reconstruction. The chamber package included 3 signal planes (X, U and V), 4 cathode planes, and 2 ground planes sharing the same gas enclosure. Only the U and the V planes could be instrumented because of space constraints. Signal planes consisted of 480 tungsten wires of 15 μ diameter, spaced so that adjacent wires were separated by 1.5 mm in the X direction. Cathode planes were wound of 63 μ diameter tungsten wire on a 0.5 mm spacing. The wires in the U and V planes were rotated from the vertical (Y axis) by ± 16.7 degrees. The readout electronics were identical to those used with the beam telescope, and the chamber used the same gas mixture.

3.11 Absorber Counter

A four element scintillation counter immediately downstream of the dump detected muons produced at angles greater than 70 mr with respect to the nominal beam direction. Because the mass of a muon pair depends linearly on the opening angle in the laboratory frame, this counter provided a high mass bias when used in one of the fast triggers. Four quadrants (ABUL, ABUR, ABDL and ABDR) made of 0.9525 cm thick PILOT A plastic scintillator[68] covered the full acceptance of the spectrometer except for a 0.305 m diameter hole centred on the beam axis. Figure 12 shows the counter and the shape of two of the four identical quadrants. Adjacent quadrants extended beyond the centre line by 12.7 cm in X and by 7.62 cm in Y to cover the full acceptance of the corresponding rear muon counter quadrant.

Each quadrant was coupled to an Amperex 56AVP photomultiplier[63] connected to a resistive divider base. As with the beam hodoscopes, the last two dynode stages were clamped with zener diodes and the output signals were clipped with a 3 ns stub of RG174 50 Ω coaxial cable terminated with a 25 Ω resistor. The photomultipliers were shielded from the fringe field of the analysis magnet by 1 cm wall thickness steel pipe, and enclosed in a 1 cm thick steel box. Discriminated signals from the four quadrants were used in one of the fast triggers and recorded for use in the analysis.

3.12 Drift Chambers

Muon trajectories in the spectrometer were measured by 18 planes of wire drift chambers. The design and operation of drift chambers have been
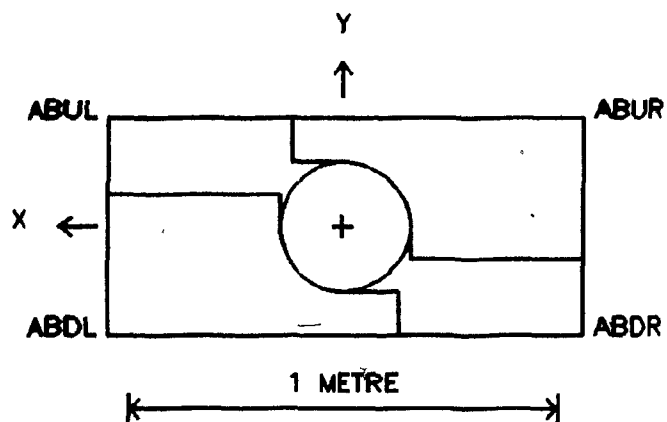
Figure 12 - Absorber Counter

The absorber counter was used to detect muons produced at large angles to the beam. Two of the four identical elements of the counter are shown in outline. Only the actual scintillator is shown.

reviewed extensively[69][70][71] and will not be discussed in detail here. The nine planes in front of the analysis magnet were grouped into three chambers of three planes each, as were the nine planes following the magnet. Wire spacings, diameters and orientations are listed in Table 3 and Table 4. The details of each chamber varied because they were constructed at different institutions.

The first chamber consisted of three signal planes wound on glass fibre-epoxy frames and sharing common cathodes. The cathode planes were also wound on glass-epoxy frames. The outermost cathodes were shielded by ground planes of similar construction. The glass-epoxy frames were bolted to an aluminum support frame and sealed with a noncorrosive silicon rubber. The cathodes were run at negative high voltage and the anode wires were direct coupled to the amplifiers.

The second and third chambers shared a common gas enclosure. The signal wires for these chambers were supported by precision inserts set in a jig bored aluminum frame. The cathodes, of stretched aluminum foil, were glued to an aluminum frame and were run at ground potential. Anode wires were capacitively coupled to the amplifiers. The physical construction of the fourth chamber was identical to that of the second and third chambers.

The final two chambers were similar to the first chamber in that wound signal planes and cathodes were used. Each plane was wound on a separate self supporting glass-epoxy frame. The cathode planes were run at negative high voltage and the signal wires were again connected directly to the amplifiers. The frames of each chamber were contained in a single gas enclosure with mylar windows.

Table 3 - Drift Chamber Parameters I

Chamber	Cell Size (cm)	Signal Wire Diameter (cm)	Cathode Plane Diameter (cm)	Drift Wire Diameter (cm)	Effective Aperture (cm)	Cathode Potential
DC1	0.6	2.0E-3 Tungsten	6.35E-3 Cu-Be 0.1016 Pitch	6.35E-3 Cu-Be	50x100	-H.V.
DC2	1.27	2.54E-3 Tungsten	2.54E-3 Al Foil	0.0127 Cu-Be	50x100	Ground
DC3	1.27	2.54E-3 Tungsten	2.54E-3 Al Foil	0.0127 Cu-Be	50x100	Ground
DC4	1.905	2.54E-3 Tungsten	2.54E-3 Al Foil	0.0127 Cu-Be	100x200	Ground
DC5	1.905	2.54E-3 Tungsten	6.35E-3 Cu-Be 0.1778 Pitch	6.35E-3 Cu-Be	167x335	-H.V.
DC6	1.905	2.54E-3 Tungsten	6.35E-3 Cu-Be 0.1778 Pitch	6.35E-3 Cu-Be	167x335	-H.V.

Table 4 - Drift Chamber Parameters II

Chamber	Plane	Type	Angle (Degrees)	Number of Cells	Cell Size (cm)	Z Position (cm)
DC1	1	V	-16.7	192	0.6	-163.70
	2	X	0.0	192	0.6	-164.25
	3	U	16.7	192	0.6	-164.93
DC2	4	V	-16.7	93	1.27	-152.81
	5	X	0.0	92	1.27	-151.50
	6	U	16.7	92	1.27	-150.17
DC3	7	V	-16.7	92	1.27	-138.84
	8	X	0.0	93	1.27	-137.55
	9	U	16.7	93	1.27	-136.27
DC4	10	V	-16.7	123	1.905	161.43
	11	X	0.0	124	1.905	163.37
	12	U	16.7	124	1.905	165.32
DC5	13	V	-16.7	192	1.905	285.09
	14	X	0.0	176	1.905	286.97
	15	U	16.7	192	1.905	288.90
DC6	16	V	-16.7	192	1.905	412.11
	17	X	0.0	176	1.905	414.02
	18	U	16.7	192	1.905	415.92

All chambers used a gas mixture of 50 percent argon and 50 percent ethane to achieve a low saturation voltage in the rear chambers, while providing a high drift velocity (50 μ/ns)[72] and minimal dead time in the front chambers. Flow rates were set to flush the individual chamber volumes once every two days.

The signal wires were connected to Lecroy MVL100 monolithic amplifier-discriminator chips[66] consisting of a 100 × gain amplifier followed by a voltage programmable ECL comparator. The control voltage was set to give discriminator thresholds between 80 mV and 130 mV at the signal wires, depending on the chamber. The differential ECL outputs of the MVL100's were connected to Lecroy 2770A drift chamber digitizers[66] and read out via CAMAC[73]. Each digitizer contained 96 time to digital converters (TDC's) with a full scale time range of approximately 256 ns for 256 counts. To correct for a channel to channel variation of 10 percent and ensure an accurate measurement of the drift time, the TDC's were calibrated at the beginning of each data tape.

The calibration system applied a series of 5 volt pulses to the field shaping wires of the chambers under computer control. These pulses induced signals on the sense wires, causing the discriminators to trigger and sending start pulses to the TDC's. A common stop pulse was sent to the TDC's after a computer controlled delay. A series of 600 calibration events was written automatically at the beginning of each data tape. Ten pulses at 10 different delay times were sent to each of the six chambers in turn. Prior to the analysis of the data tapes, the calibration events were read and straight lines were fit to the number of counts vs delay curves to obtain a set of calibration constants for each digitizing channel on each

tape. After calibration the TDC's had a time resolution of better than 1 ns.

A stand alone version of the calibration system was used to monitor the drift chamber electronics and diagnose malfunctioning channels throughout the data taking.

3.13 Analysis Magnet

The spectrometer magnet was a large window frame dipole with saddle coils containing 240 turns. The magnet aperture measured 90 cm vertically and 180 cm horizontally with a 75 cm long iron yoke. At the nominal setting of 2400 amperes, the main component of the field gave a horizontal momentum change to the particles of 830 MeV/c. The field was mapped by measuring the current induced in 3 orthogonal coils as they moved through the magnetic field under computer control. NMR measurements of the field at the centre of the magnet were used for absolute calibration. The magnet current was monitored continuously by a precision shunt in addition to the standard power supply current transducer. The field was monitored using a Hall probe fixed to the lower pole face of the magnet. The agreement between the current shunt and the Hall probe was always better than 0.1 percent. Using the measured $\int B \cdot dl$ of the magnet, the ψ mass was reproduced to better than 1 percent accuracy. The polarity of the field was reversed periodically during the course of the 1981 run to check for systematic effects associated with properites of the beam halo.

3.14 Charged Particle Hodoscope

Two scintillation counter hodoscopes, CPX and CPY, located immediately behind the final drift chamber measured the X and Y positions of charged tracks respectively.

The CPX hodoscope consisted of two rows of counters made of 1 cm thick × 4 cm wide × 1m long NE110 plastic scintillator[62], and arranged as shown in Figure 13. The counters were coupled to EMI 9807B and 9814B photomultiplier tubes[74] with transistorized bases[65]. A simplified schematic diagram of the CPX electronic logic is shown in Figure 14. The output signal from each photomultiplier on the top row of 92 counters was summed with the signal from the corresponding counter in the lower row before discrimination. Logical signals from the combined CPX counters were summed and rediscriminated to supply a CPX≥2 signal to the fast trigger logic when more than two of the counters were hit. The discriminated signals from all of the CPX counters were recorded for each event.

The CPY hodoscope consisted of 48 1 cm thick × 8 cm wide × 2m long NE110 plastic scintillation[62] counters coupled to Amperex 56AVP[63] photomultiplier tubes with transistorized bases[65]. The counters were arranged in two vertical columns of 24 counters each extending from X = 0.0 to X = ±2.0 m. Logical signals from the CPY counters were used by the trigger processor. As with the CPX counters, discriminated signals from the CPY counters were recorded for each event.

Central counters in both hodoscopes were retracted to leave a 32 cm square beam hole.
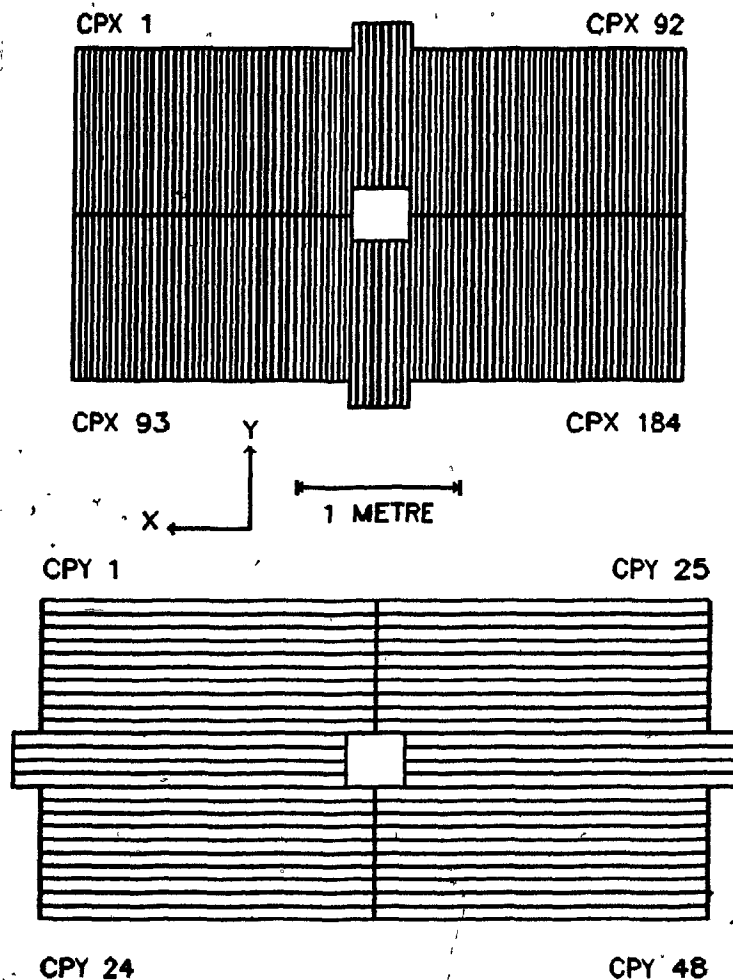
Figure 13 - Charged Particle Hodoscope

The Charged Particle Hodoscopes, CPX and CPY, measured the X and Y positions of charged tracks as discussed in the text. The counters are shown looking along the beam direction and the scale is indicated.
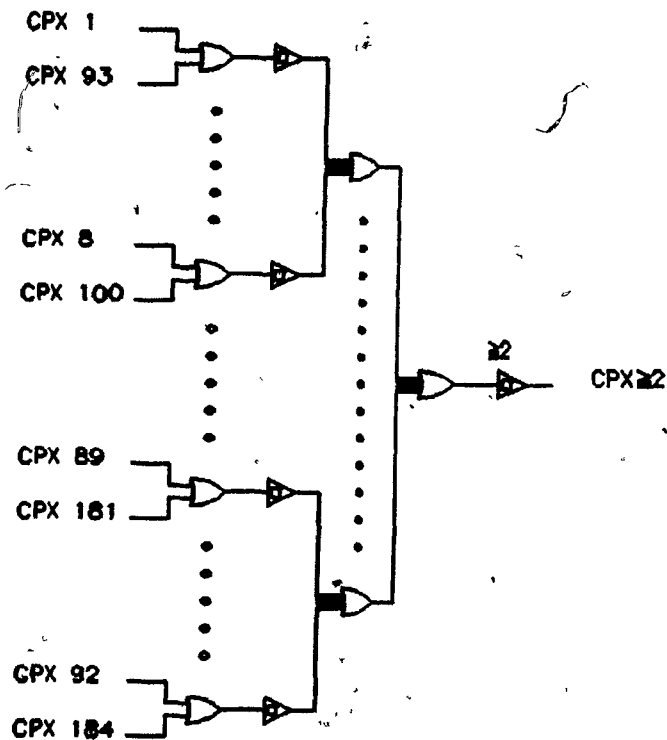
Figure 14 - Charged Particle Hodoscope Logic

This simplified schematic diagram shows the electronic logic used to define the CPX≥2 signal from the outputs of the CPX counters. Photomultiplier signals from the upper row of counters were summed with signals from the corresponding counters in the lower row prior to discrimination. The linear sum of the discriminated signals was rediscriminated to define the CPX≥2 signal.

3.15 Muon Hodoscopes

Muons were identified by requiring them to traverse a telescope of three scintillation counter hodoscopes interleaved with walls of steel and concrete. The arrangement of the counters in the first plane and a plan view of the three planes is shown in Figure 15.

The first muon hododscope, $\mu1$, consisted of two rows of 30 1 cm thick × 20.3 cm wide × 1.45 m long counters made of NE114 plastic scintillator[62] located behind a 1.106 m thick steel wall. The four central counters in the first plane were retracted to leave a 20.32 cm square beam hole. A second hodoscope, $\mu2$, with two rows each consisting of 31 1 cm thick × 23 cm wide × 1.57 m long counters followed a 61 cm thick steel wall. A third hodoscope, $\mu3$, with 62 1 cm thick × 26.7 cm wide × 1.75 m long counters arranged in two rows of 31 counters each, followed a 90 cm thick concrete wall. Counters in the first plane were spaced 20.574 cm centre to centre so that there was no overlap between adjacent counters, and the array was positioned symmetrically about the beam axis. Counters in the second and third planes were spaced 22.225 cm and 24.57 cm apart respectively.

All of the muon counters were coupled to Amperex 2212B photomultipliers[63] with transistorized bases[65]. Discriminated signals from counters in the upper row of the first wall were combined with the logical OR of pairs of counters in the upper rows of the second and third planes to define muon triple coincidence signals TC1-TC30 as follows:

$$TC1 = \mu1\text{-}1 \cdot (\mu2\text{-}1 + \mu2\text{-}2) \cdot (\mu3\text{-}1 + \mu3\text{-}2),$$

$$TC2 = \mu1\text{-}2 \cdot (\mu2\text{-}2 + \mu2\text{-}3) \cdot (\mu3\text{-}2 + \mu3\text{-}3),$$
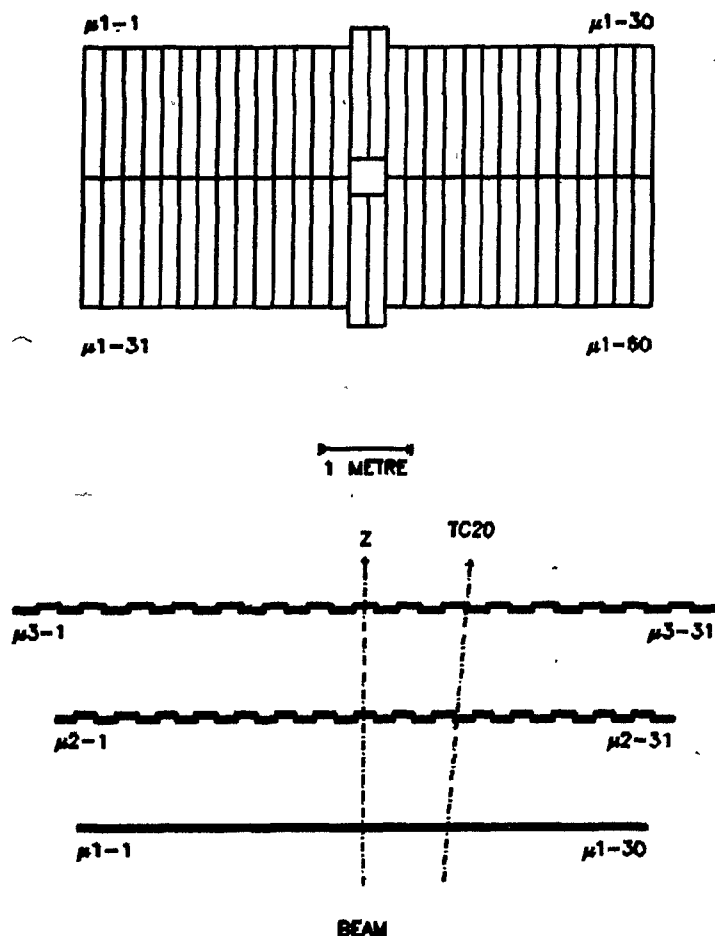
-56-

Figure 15 - Muon Triple Coincidence Counters

This figure shows the first plane of muon hodoscope counters and the relative locations of counters in the three planes. All planes were centred on the nominal beam axis. The central counters in the first plane were withdrawn to create a beam hole. The centre line of a typical muon triple coincidence channel is indicated by the dashed line.

. . .

and

$$TC30 = \mu1\text{-}30 \cdot (\mu2\text{-}30 + \mu2\text{-}31) \cdot (\mu3\text{-}30 + \mu3\text{-}31),$$

as shown in Figure 16. The signals TC31-TC60 were defined for the lower row of counters as follows:

$$TC31 = \mu1\text{-}32 \cdot (\mu2\text{-}32 + \mu2\text{-}33) \cdot (\mu3\text{-}32 + \mu3\text{-}33),$$

$$TC32 = \mu1\text{-}33 \cdot (\mu2\text{-}33 + \mu2\text{-}34) \cdot (\mu3\text{-}33 + \mu3\text{-}34),$$

. . .

and

$$TC60 = \mu1\text{-}61 \cdot (\mu2\text{-}61 + \mu2\text{-}62) \cdot (\mu3\text{-}61 + \mu3\text{-}62).$$

To suppress coincidences caused by halo muons, the counters of each triple coincidence channel were centred to line up along the path taken by an infinite momentum muon produced in the target. The widths of the counters in the second and third planes were chosen to give good acceptance down to muon momenta of 6 GeV/c when allowances were made for multiple scattering.

Logic signals from all of the counters were recorded and read out via CAMAC[73] for each event. The time elapsed between the event trigger and the signals from the first plane of muon counters was measured and recorded using Lecroy 2249A 8 channel TDC's[66] so that backgound due to beam halo or hadronic decays could be studied offline.

3.16 Fast Logic

Standard NIM[67] logic modules were used to form three fast trigger signals if appropriate combinations of counters had outputs consistent with the signature of a high mass muon pair, a single beam particle hitting the
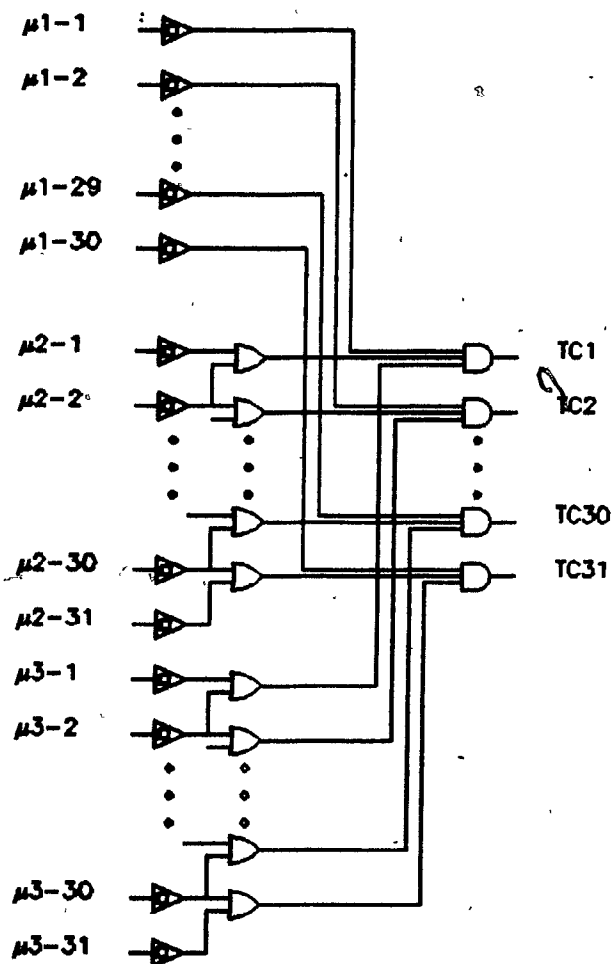
Figure 16 - Muon Triple Coincidence Logic

This simplified schematic diagram shows the electronic logic used to define
the muon triple coincidence signals TC1-TC30 from the photomultipler outputs
of counters in the top rows of the three muon hodoscopes as discussed in the
text. Identical logic was used to define the signals TC31-TC60 from the
outputs of counters in the lower rows.

target and two muons traversing the apparatus. A simplified schematic diagram of the fast trigger logic is shown in Figure 17. In the absence of any transverse momentum, muons from a high mass pair would enter the apparatus in different geometrical quadrants. The accidental coincidence between a beam halo muon and a muon produced by hadronic decay would not be so constrained. The four fold symmetry of the apparatus about the beam axis was exploited in the definition of the trigger signals to bias against muon pairs produced by such accidental coincidences.

A muon was assumed to have traversed the apparatus if one of the muon triple coincidences produced a signal. The 60 TC channels were combined together 15 at a time to form 4 quadrant signals as follows:

$$\mu QUAD1 = TC1 + TC2 + \ldots + TC15,$$

$$\mu QUAD2 = TC16 + TC17 + \ldots + TC30,$$

$$\mu QUAD3 = TC31 + TC32 + \ldots + TC45,$$

and

$$\mu QUAD3 = TC46 + TC47 + \ldots + TC60.$$

A QUAD signal was defined as

$$QUAD = (\mu QUAD1 \cdot \mu QUAD2) + (\mu QUAD1 \cdot \mu QUAD3) +$$

$$(\mu QUAD1 \cdot \mu QUAD4) + (\mu QUAD2 \cdot \mu QUAD3) +$$

$$(\mu QUAD2 \cdot \mu QUAD4) + (\mu QUAD3 \cdot \mu QUAD4),$$

indicating that two muons had passed through different quadrants of the apparatus. The timing of the QUAD signal was set by the leading edge of the $\pi^-/\bar{p}$ signal from the beam tagging logic.

The lowest level fast trigger was defined as

$$TRIG0 = (\pi^-/\bar{p}) \cdot QUAD.$$
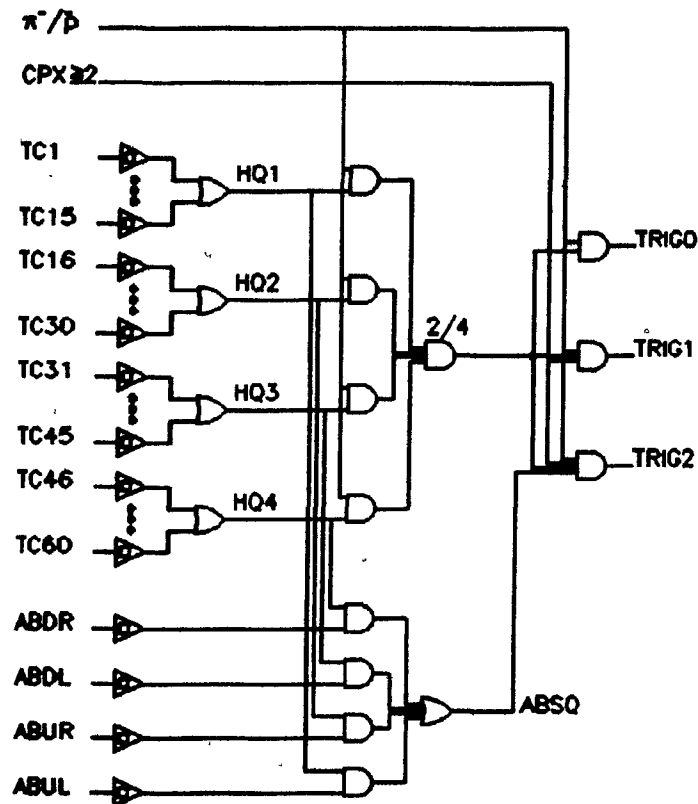
Figure 17 - Trigger Logic

This simplifed. schematic diagram shows the electronic logic used to define
the three fast trigger signals. These signals were separately prescaled and
then combined with PION and PBAR signals from the beam logic to give a final
trigger signal.

Incorporating the requirement that at least two charged particles had passed through the CPX hodoscope, the CPX$\geq$2 signal was used to define the fast trigger TRIG1 as

$$\text{TRIG1} = \overline{(\pi^-/\overline{p})} \cdot \text{QUAD} \cdot \text{CPX}\geq 2.$$

With typical beam conditions, the CPX$\geq$2 requirement reduced the trigger rate by a factor of 2. The most restrictive of the fast triggers was biased against low mass pairs by requiring at least one of the muons to hit an absorber counter quadrant and was defined as

$$\text{TRIG2} = (\pi^-/\overline{p}) \cdot \text{QUAD} \cdot \text{CPX}\geq 2 \cdot \text{ABSQ}.$$

The signal ABSQ was in turn defined as

$$\text{ABSQ} = (\text{ABUL} \cdot \mu\text{QUAD1}) + (\text{ABUR} \cdot \mu\text{QUAD2}) +$$

$$(\text{ABDL} \cdot \mu\text{QUAD3}) + (\text{ABDR} \cdot \mu\text{QUAD4}).$$

The TRIG2 rate was typically a factor of 5 lower than the TRIG0 rate.

The three fast triggers were prescaled separately and then combined with PION and PBAR signals from the beam logic to provide a final event trigger signal for the computer controlled readout. Most of the antiproton data was taken with TRIG1 in order to avoid the kinematic biases of the absorber counter. The bulk of the pion data was taken with TRIG2 to keep the overall event rate as low as possible. Sufficient data was taken with TRIG0 to check the efficiency of the CPX and absorber counters. Special runs requiring only two of three counters in the muon triple coincidences were taken to check the muon counter efficiencies.

3.17 Trigger Processor

Events satisfying the fast trigger logic were examined by a digital trigger processor in real time. The processor has been described in some

detail elsewhere[75], and therefore only the algorithm used and its implementation will be outlined here.

Wires hit in the X planes of the chambers downstream of the magnet, CPX counter outputs, CPY counter outputs, and muon triple coincidence channel outputs were stored by a fast ECL encoder gated by the trigger logic. A hard wired trigger processor employing the Fermilab ECL-CAMAC system of modules[76][77] calculated the invariant mass of all possible muon pairs and rejected events which reconstructed to a mass of less than 2.0 GeV/c².

The processor examined all combinations of drift chamber hits and counter outputs to find candidate tracks in the X projection. The momenta and opening angles in this projection were calculated assuming that the tracks originated in the target. The CPY counter information was used to give an upper bound on the opening angle in the Y projection. The invariant mass was calculated for each pair of tracks using the approximation

$$M^2 = p_i p_j \theta_{ij}^2$$

where p_i and p_j are the momenta of the ith and j^{th} tracks respectively, and θ_{ij} is the angle between the tracks in radians. Events with any combination giving a mass above 2.0 GeV/c² were read out via CAMAC[73] and recorded on magnetic tape. Events with no candidates reconstructing to at least the minimum mass were cleared and reset without being read.

The processor made extensive use of precalculated tables stored in fast memories to simplify the logic and improve the performance. Typically about 5 μs were required to evaluate an event, and events complicated enough to require more than 100 microseconds to evaluate were accepted unconditionally.

During the development of the processor, a diagnostic and simulation programme was written using the interactive language FORTH[78]. Test events from the simulation programme and data tapes allowed the processor to be tested in stages by comparing internal values to results calculated by the simulator.

A fraction of the triggers obtained during any given run were recorded unconditionally, so that the trigger processor performance and efficiency could be checked. The usefulness of the trigger processor can be seen immediately from Figure 18, which shows the large number of low mass events that were rejected. Its efficiency can be seen from Figure 19, by comparing the number of events rejected by the processor to the results of a full reconstruction. The processor reduced the overall trigger rate by a factor of 5-10, depending on the beam tune, with an efficiency of better than 99 percent.

3.18 Data Acquisition

The experiment was controlled and monitored using a PDP 11/45 computer[79] running under the RSX11/M operating system. Data recording modules were connected to the computer using 3 parallel CAMAC[73] branches. Two 800 BPI magnetic tape drives were used to record the events for offline reconstruction.

One CAMAC branch was used to service the trigger processor described in the last section. A second branch contained the following:
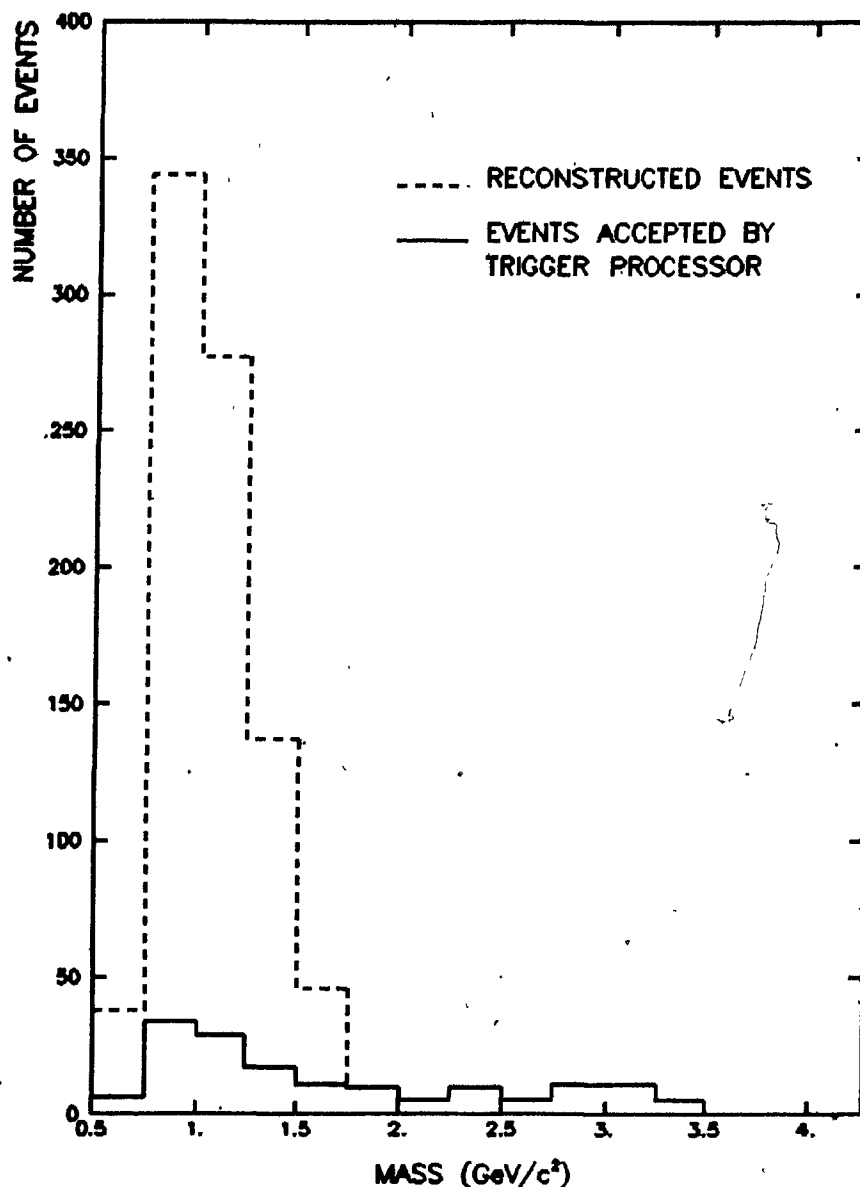
Figure 18 - Trigger Processor Performance

The dashed line shows the mass spectrum of muon pairs reconstructed offline from events where the processor information was not used in the trigger. The solid line shows the mass spectrum of the events accepted by the trigger processor. The large numbers of low mass events rejected by the trigger processor resulted in a substantial reduction of the trigger rate.
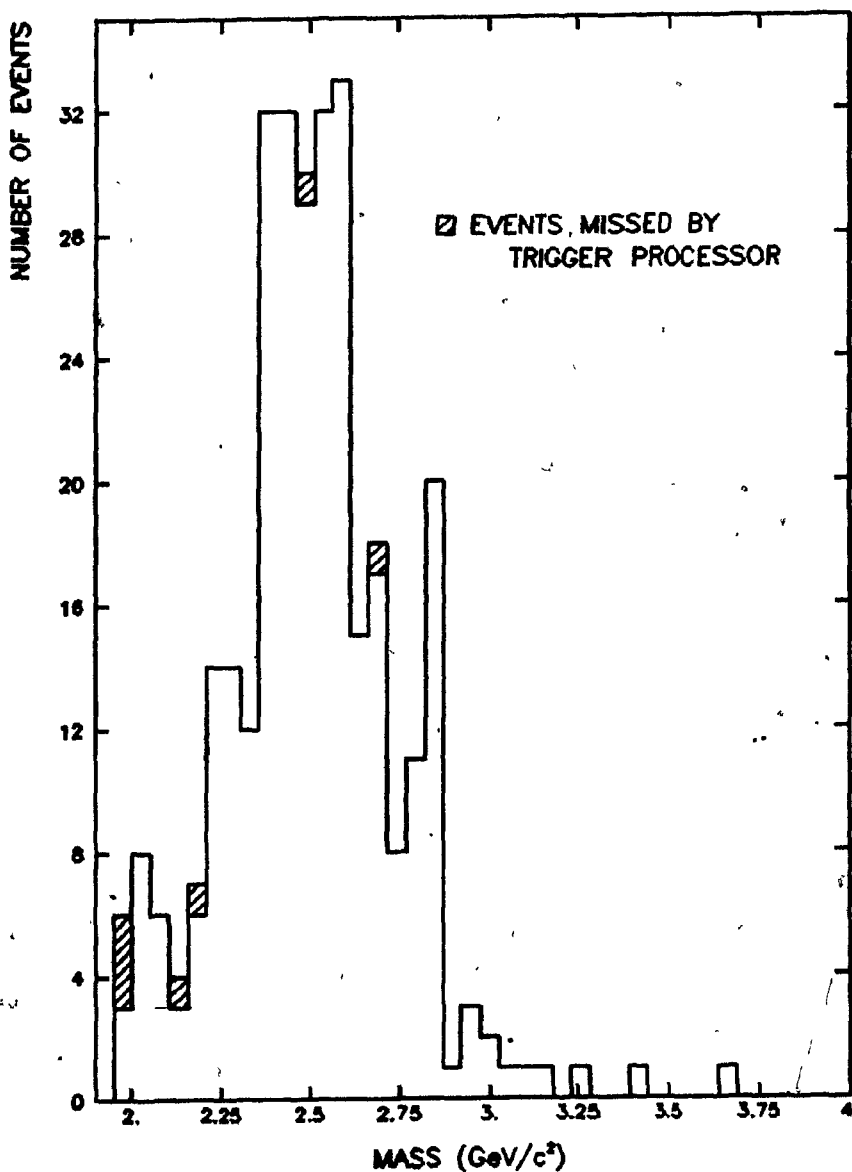
Figure 19 - Trigger Processor Efficiency

This histogram shows the mass spectrum of muon pairs reconstructed offline from events where the processor information was not used in the trigger. The hatched areas show events that would have been rejected by the trigger processor. The measured efficiency of the processor was 0.99.

1. scalers used to monitor counting rates at various stages of the fast trigger logic and to record beam flux totals;

2. analog to digital converters (ADC's) used to monitor the performance of various counters throughout the experiment;

3. time to digital converters (TDC's) used to monitor the Cerenkov counters and the first plane of muon counters; and

4. coincidence registers which were used to record the state of all the counters in the experiment at the time of the trigger.

A third branch was used to read out the wires hit in the proportional and drift chamber systems.

The output of the trigger processor was used to interrupt the computer, which then read out the three CAMAC branches using a Fermilab supplied data acquistion package[80][81]. The events were transferred directly into a 256 Kbyte bulk memory[82] during the spill, and transferred to magnetic tape at the end of each spill. The information recorded for each event included the following:

1. the date and time of the spill;

2. a list of all proportional chamber wires hit;

3. a list of all drift chamber wires hit and the drift times;

4. a complete list of all counters hit in coincidence with the fast

trigger; and.

5. ADC and TDC information for monitoring purposes.

In addition at the end of each spill, a list of scaler sums was written to the tape. This list included the following:

1. antiproton and pion flux totals;

2. primary beam intensities;

3. counting rates in the Cerenkov counters and the beam telescope;

4. counting rates of the absorber counters and selected muon counters; and

5. counting rates at various stages in the beam logic and the fast trigger logic.

The reconstruction of the muon pair kinematic variables from the information on the data tapes will be discussed in the next chapter.

3.19 Online Analysis

During the data taking the spectrometer performance was monitored online by several analysis programmes based on SUPERGRAM[83][84], a histogramming package written at the University of Michigan. By efficiently using disk storage, SUPERGRAM was capable of accessing over 10^5 bins of

information while requiring only 6×10^3 words of programme memory space. The online analysis performed the following functions:

1. kept track of scaler sums to give up to date beam totals, and to monitor the performance of the beam tagging system and the trigger;

2. histogrammed wire and time distributions for the drift chambers and proportional chambers to aid in the diagnosis of malfunctioning channels and to monitor chamber efficiencies;

3. histogrammed TDC, ADC and latch information to monitor counter and trigger performance;

4. controlled the data acquisition system, beginning and ending runs; and

5. plotted histograms under console command.

The online analysis was typically able to process 10 percent of the events in the time between successive beam spills, giving prompt information about problems with the apparatus as they arose. A version of the online analysis which read events from data tapes allowed efficient development and testing of the online software.

3.20 Data Sample

The experiment collected data for a total of 13 weeks between April and June of 1981 and January and March of 1982, collecting 1500 data tapes.

Most of the data was taken using a tungsten target in order to achieve the highest possible event rate. Ten percent of the running time was spent using a beryllium target, and 6 percent using a copper target, so that the A dependence of the cross section for ψ production by antiprotons and pions could be investigated. Of the 84 percent of the data taken with tungsten targets, 28 percent was taken with the 1.0 interaction length target during the 1981 run. For the 1982 run, the length of the target was increased to 1.5 interaction lengths and 46 percent of the running time was spent using this configuration. In the final weeks of the 1982 run, the remaining 10 percent of the total running time was spent using a 0.4 interaction length tungsten target so that corrections for reinteraction of secondary particles could be investigated.

During the course of the data taking, the performance of the spectrometer was monitored online as described in a previous section. A subsample of the data tapes was also analysed offline as the experiment proceeded to ensure that the apparatus was working correctly. After the completion of the data taking, events on the complete set of data tapes were analysed and reconstructed as described in the next chapter.

CHAPTER 4

Reconstruction

The information from the drift chambers was used to reconstruct the trajectories of charged particles which had travelled through the apparatus. Track segments in the rear chambers were linked with segments in the chambers in front of the magnet. The momentum of each particle was calculated from the bend in the trajectory caused by the analysis magnet. To eliminate tracks left in the chambers by the debris from other interactions, the tracks were required to intersect with CPX and muon hodoscope counters that had been hit in coincidence with the trigger. The four momenta of the muons were combined with information from the beam telescope to calculate the kinematic variables of the muon pair. Many of the details of the calibration procedure, time to distance conversion, track reconstruction, and track finding efficiency have been discussed at length in another thesis[85] and will not be repeated here.

Reconstruction of the events from the data tapes took place in three stages. In the first stage of the analysis, each event was required to have two tracks in the chambers which pointed to muon triple coincidence channels that had been hit in coincidence with the trigger. The two tracks were required to give an invariant mass of at least 2 GeV/c². If an event satisfied these critera the original event record was written to a secondary file known as a condensed file. A data tape with 1.4×10^5 triggers could be reduced to a file of 200 condensed events in 1500 CPU seconds on the Fermilab Cyber 175 computer[86]. The condensed files from each run were collected on tape and subject to a second stage of analysis.

In the second stage, the events on the condensed data tapes were subject to the full analysis using both the drift chamber and beam telescope information. The track parameters from this stage of the analysis were written to a data summary tape without the original event record. Each event required four times as much CPU time at this stage as had been required for the previous condensation. The summary tapes allowed events to be studied in detail without repeating the reconstruction each time.

In the final stage, the reconstructed tracks were required to pass through fiducial regions corresponding to the physical apertures of the apparatus. Additional requirements were made on events with a high energy negative muon to reduce the contamination from beam halo. Events meeting all of these conditions were listed on a disk file with their reconstructed kinematic variables, centre of mass energy, and trigger level requirement.

The entire chain of analysis programmes was checked using Monte Carlo events written in the original data event format with background hits incorporated from actual experimental data events.

4.1 Drift Chamber Calibration

The first step in the drift chamber track reconstruction involved the calibration of the time to digital converters (TDC'S) and the conversion of the drift time to drift distance. To a good approximation, the drift velocity of electrons in the 50 percent argon and 50 percent ethane mixture used in this experiment is 50 μ/ns at atmospheric pressure independent of the electric field[72]. Because the drift paths are not always linear, and the drift velocity is not exactly constant across the cell, a better estimate of the time to distance conversion is obtained by integrating the time spectrum[87] as shown in Figure 20. If the chamber is illuminated by a uniform flux of N particles across a drift cell of width Δx, the time spectrum will be given by

$$\frac{dN}{dt} = \frac{dN}{dx}\frac{dx}{dt}$$

where

$\frac{dN}{dt}$ is the number of particles having a drift time t,

$\frac{dN}{dx} = \frac{N}{\Delta x}$ is the constant flux, and

$\frac{dx}{dt}$ is the drift velocity which may be a function of x.

By integrating both sides, the time to distance conversion relationship can be expressed as

$$x(t) = \frac{1}{N}\Delta x \int \frac{dN}{dt}\, dt.$$

An initial analysis of a subset of the data tapes was made assuming a constant drift velocity across the cell. The time spectra of drift chamber hits used for the tracks reconstructed in this analysis were integrated to give a time to distance conversion relationship for each drift chamber plane. The relationships were stored as tables on a disk file.

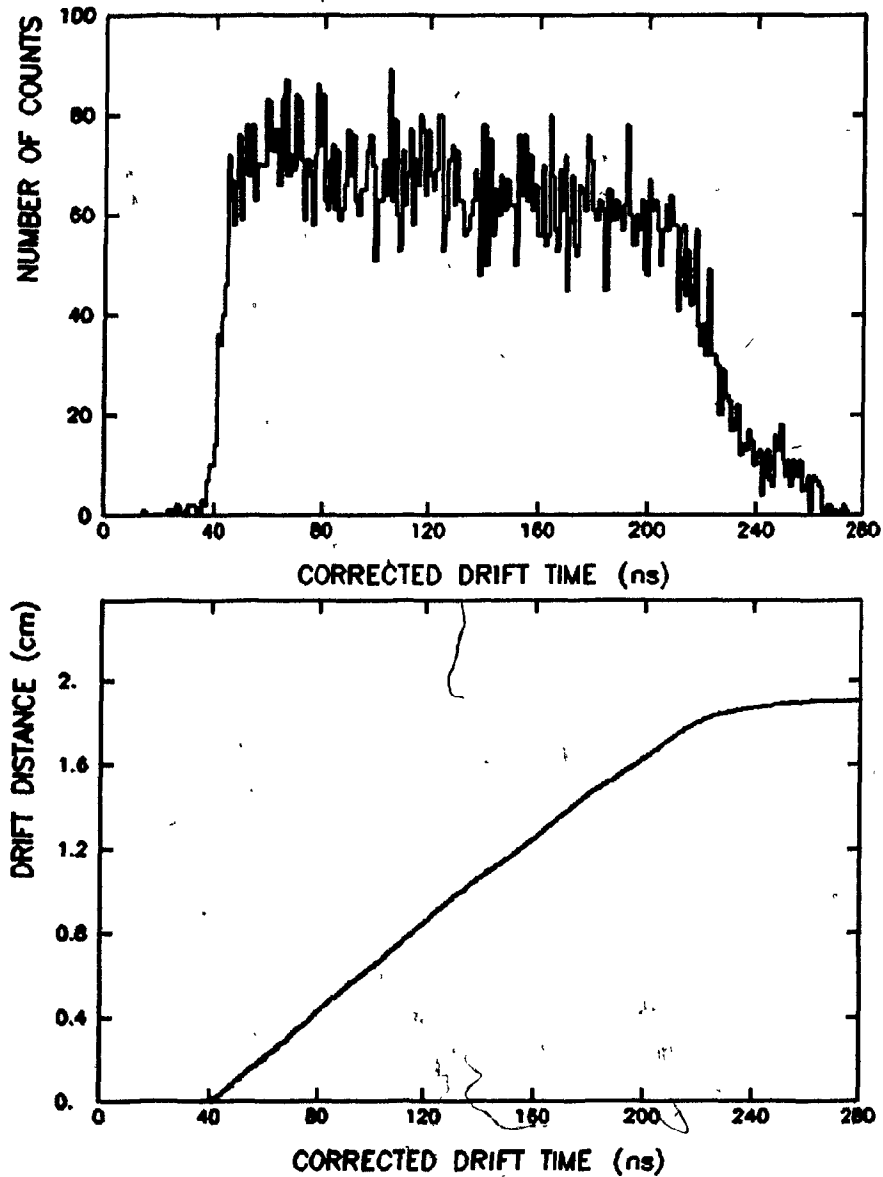As discussed in the last chapter, each data tape began with a series of

Figure 20 - Time to Distance Conversion

The top histogram shows the number of tracks plotted against the corrected drift time for the X plane of drift chamber DC4. The lower figure shows the integrated time distribution normalized to give the time to distance conversion as discussed in the text.

six hundred calibration events. Prior to the analysis, the calibration events were read and straight lines were fit to the number of counts vs delay curve for each TDC. As the TDC information was read for each event, the calibration constants for each channel were used to convert the counts to drift time. The drift time was used to look up the distance the track had passed from the sense wire.

4.2 Drift Chamber Reconstruction

The drift chamber track reconstruction proceeded from the rear of the spectrometer to the front. The chambers downstream of the magnet typically had half as many wires hit per plane for a given event, and this made track finding simpler. Track segments in the rear were projected through the magnet and used to help find the coresponding hits in the front chambers. The track momentum was calculated from the bend of the track in the analysis magnet and combined with the direction of the upstream track segment to give the four momentum of the muon in the laboratory frame. The charge of each particle was determined from the direction of the magnetic deflection.

The information from each of the drift chambers in the rear was studied in turn and all possible combinations of hits were examined to find intersections of U and V wire hits that coincided with an X wire hit as shown schematically in Figure 21. The combination was deemed to be a rough triplet if

$$|X - \cos\theta \frac{U+V}{2}| \leq 0.8\Delta X$$

where

X, U and V are the coordinates of the wires as measured from the Z axis as shown in the figure,
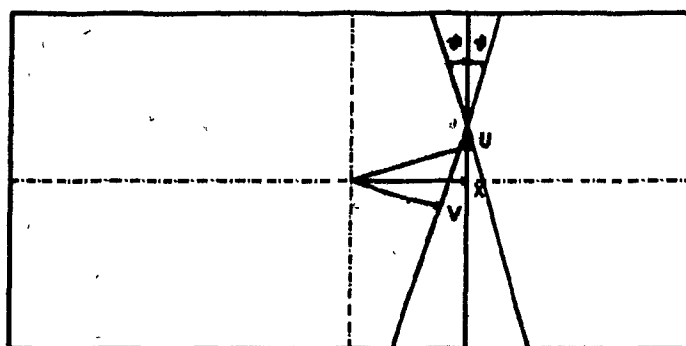
Figure 21 - Drift Chamber Triplets

The intersections of hit wires in the X, U, and V planes of a chamber were used to define a drift chamber triplet as discussed in the text. The X,U and V coordinates were measured from the centre of the chamber as indicated by the arrows.

ΔX is the chamber wire spacing, and

$\theta = \tan^{-1}0.3$ is the stereo angle from the vertical of the U and V planes in the drift chambers.

At this stage only the wire coordinates were used; no information about the drift time was included. Up to 40 rough triplets were allowed in each chamber.

The next step was to combine the rough triplets in the three chambers downstream of the magnet to find all possible track segments. Three triplets, one each in chambers DC4, DC5 and DC6, were deemed a rough track segment (no drift time information used) if

$$\left| X_5 - \frac{X_4 + X_6}{2} \right| \leq 1.1\Delta X$$

and

$$\left| Y_5 - \frac{Y_4 + Y_6}{2} \right| \leq 1.1\Delta X / \tan\theta$$

where

X_i and Y_i are the coordinates of the triplet in chamber DCi, and ΔX and θ are the wire spacing and stereo angle as discussed above. After all track segments with three rough triplets were found, the programme returned to find any track segments that could be constructed using two rough triplets and a pair of wires in the remaining chamber. Thus a track segment required that at least 8 of the 9 possible hits be found before it could be reconstructed. Again up to 40 rough track segments were allowed.

At this point, the time information was included to refine the rough triplets. The drift time was calculated from the digitizer counts using the calibration constants discussed in the last section, and was used in turn to calculate the distance the track had passed from the sense wire. The slopes of the rough tracks were used to project the hits in the U and V planes onto

the corresponding X plane. When the time information was included, each set of three hit wires could be used to construct 2^3 possible fine triplets because of the left-right ambiguity inherent in the drift time. The X and Y positions of each possible fine triplet were calculated as

$$X_{Triplet} = (V+X+U)/3$$

and

$$Y_{Triplet} = (V-U)/(2\tan\theta)$$

where X, U and V are the coordinates of the drift chamber hits projected onto the appropriate X plane with the time information included. The sum of the squared residual distances, R^2, of the X, U and V hits from the position of the fine triplet, that is,

$$R^2 = (X-X_{Triplet})^2+(U-U_{Triplet})^2+(V-V_{Triplet})^2$$

was required to be less than 0.016 cm^2 where the U and V positions of the triplet were given by the following expressions:

$$U_{Triplet} = (X_{Triplet}+Y_{Triplet}\tan\theta); \text{ and}$$

$$V_{Triplet} = (X_{Triplet}-Y_{Triplet}\tan\theta).$$

Again θ is the stereo angle of the U and V planes. The residuals of the fine triplets in the rear chambers typically had an RMS value of 0.25 mm. The fine triplets were in turn used to define fine tracks in the rear.

The remaining track segments in the rear were then projected through the magnet to the plane of the third drift chamber. The Y coordinates of rough triplets in the chamber were compared to the Y coordinate of each projected track in turn and fine triplets were constructed if a match was found. Rough track segments in the front were constructed by linking the fine triplets in the third chamber with the intercept at the magnet bend plane of the track segment in the rear. The candidate track segments in the front were projected to the first and second chambers which were then

examined for triplets or doublets of wires. Rear track segments which could not be matched with triplets in the third chamber were checked against triplets in the first and second chambers. All tracks required at least one triplet and two doublets be found in the front chambers before it could be reconstructed. The residuals of the fine triplets in the front chambers typically had an RMS value between 0.30 and 0.35 mm.

The horizontal momentum component of each track was then calculated by fitting a circular arc of radius

$$\rho = L_{Eff}/(\sin\theta_{IN}-\sin\theta_{OUT}),$$

as shown in Figure 22, between the X projections of the front and rear track segments and using[13]

$$P_{X-Z} = 0.3H\rho/c.$$

The quantities appearing in these equations are defined as follows:

θ_{IN} is the angle between the the X-Z projection of the track upstream of the magnet and the Z axis;

θ_{OUT} is the angle between the the X-Z projection of the track downstream of the magnet and the Z axis;

L_{Eff} is the effective length of the field;

P_{X-Z} is the component of momentum in the X-Z plane measured in MeV/c;

H is the magnetic field in Kgauss; and

ρ is the radius of curvature of the track in centimetres.

Corrections were applied for the energy loss of the muons in the copper absorber[88], and the four momentum components of each muon were calculated from P_{X-Z} and the direction of the upstream track segment as

$$P_X = P_{X-Z}\sin\theta_{IN},$$

$$P_Y = P_{X-Z}\cos\theta_{IN}\frac{dY}{dZ},$$

$$P_Z = P_{X-Z}\cos\theta_{IN}, \text{ and}$$
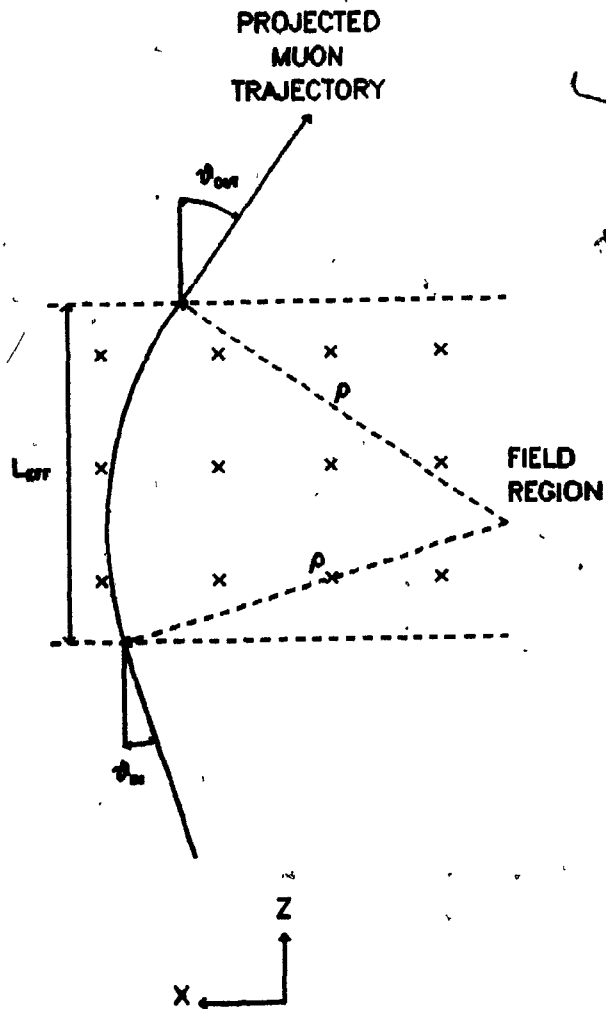
Figure 22 - Momentum Calculation

The momenta of the tracks were calculated using a square field approximation as discussed in the text.

$$E = (p_X^2 + p_Y^2 + p_Z^2 + M_\mu^2)^{1/2}$$

where $\frac{dY}{dZ}$ is the Y slope of the upstream track segment. The charge of each muon was determined from the direction of the deflection in the magnetic field.

4.3 Beam Chamber Reconstruction

The large momentum spread and spatial divergence of the beam made it necessary to measure the position and momentum of each individual beam particle. Information from the beam chambers and the beam hodoscope counter elements was used to reconstruct the beam particle trajectories. The particle momenta were calculated from the bend in the trajectories caused by the magnets in the beam spectrometer.

Wires hit in the nine planes of beam proportional chambers were examined to find triplets in each of the three beam stations as shown schematically in Figure 23. Correlated triplets in the three stations were matched in the non-bend or X coordinate to find tracks. The momenta of the tracks were calculated using a single bend plane approximation for the pair of dipole magnets in the beam spectrometer. Candidate tracks outside of the acceptance of the beam telescope or of the momentum bite of the beam were rejected.

As discussed in the last chapter the beam counter hodoscopes were designed to have a sensitive time shorter than the separation between successsive RF buckets. Residual tracks in the chambers due to particles not in coincidence with the trigger were eliminated by requiring the trajectories to point at beam hodoscope elements which had recorded a count.

Figure 23 - Beam Chamber Triplets

Beam chamber triplets were defined by the intersections of hit wires in the
Y, U, and V planes. The Y, U, and V coordinates were measured from the
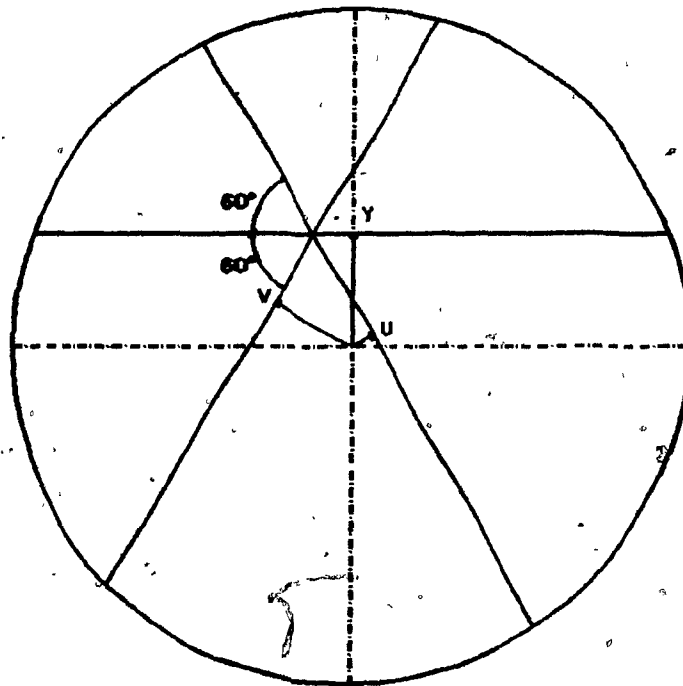centre of the chamber as indicated by the arrows.

The beam momentum spectrum and profile are shown in Figure 24. The momentum spread of the beam was 15 GeV/c FWHM. At the target the beam had a spatial spread of 10 cm FWHM in X and 6 cm FWHM in Y. The beam is not centred about Y = 0 at the target because of the upward bend caused by the momentum tagging magnets. The tagging system allowed the momentum to be measured to 1 GeV/c and the position to 0.5 cm FWHM at the target position.

4.4 Vertex and Halo Requirements

Pairs of reconstructed tracks were projected upstream through the beam dump to determine whether the collision had occured in the target or the dump. The point at which the distance between the tracks was a minimum was used as a first estimate of the production vertex. Information from the drift chambers, beam chambers, and the absorber chamber was used to make a better estimate of the vertex using the algorithm discussed in Appendix II. A histogram of the Z position of the reconstructed vertices for pion induced events in the 1982 sample is shown in Figure 25, and the position of the target and the upstream end of the dump are indicated. The vertex reconstructed in this way allowed events produced in the dump to be clearly separated from events originating in the target.

Requirements were placed on the distance between the tracks at the reconstructed vertex and on the position of the vertex to ensure that the two muons did originate at a common point and were not the result of an accidental coincidence between a halo particle and a muon from the decay of a hadron. The reconstructed vertex was required to be within 9.144 cm in X and 10.16 cm in Y of the nominal beam spot at the target, that is, X = 0.0 and Y = 5.08 cm. The Z position of the reconstructed vertex was required to
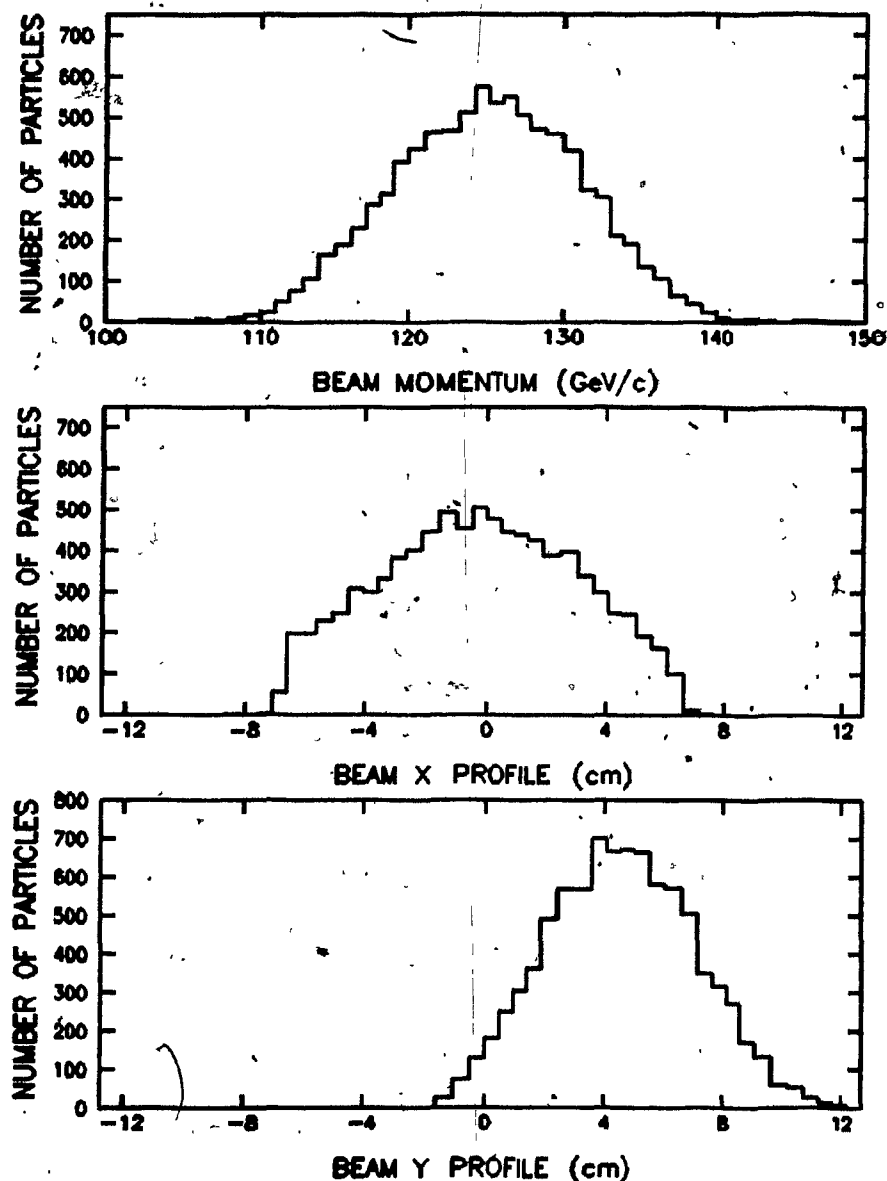
Figure 24 - Beam Momentum Spectrum and Profile

The top histogram shows the reconstructed beam momentum for events from the 1981 run. The second histogram shows the X distribution of the beam tracks at the target. The Y distribution of the tracks at the target is shown in the final histogram. The Y distribution of the beam is not centred at 0 because of the upward bend caused by the momentum tagging magnets.
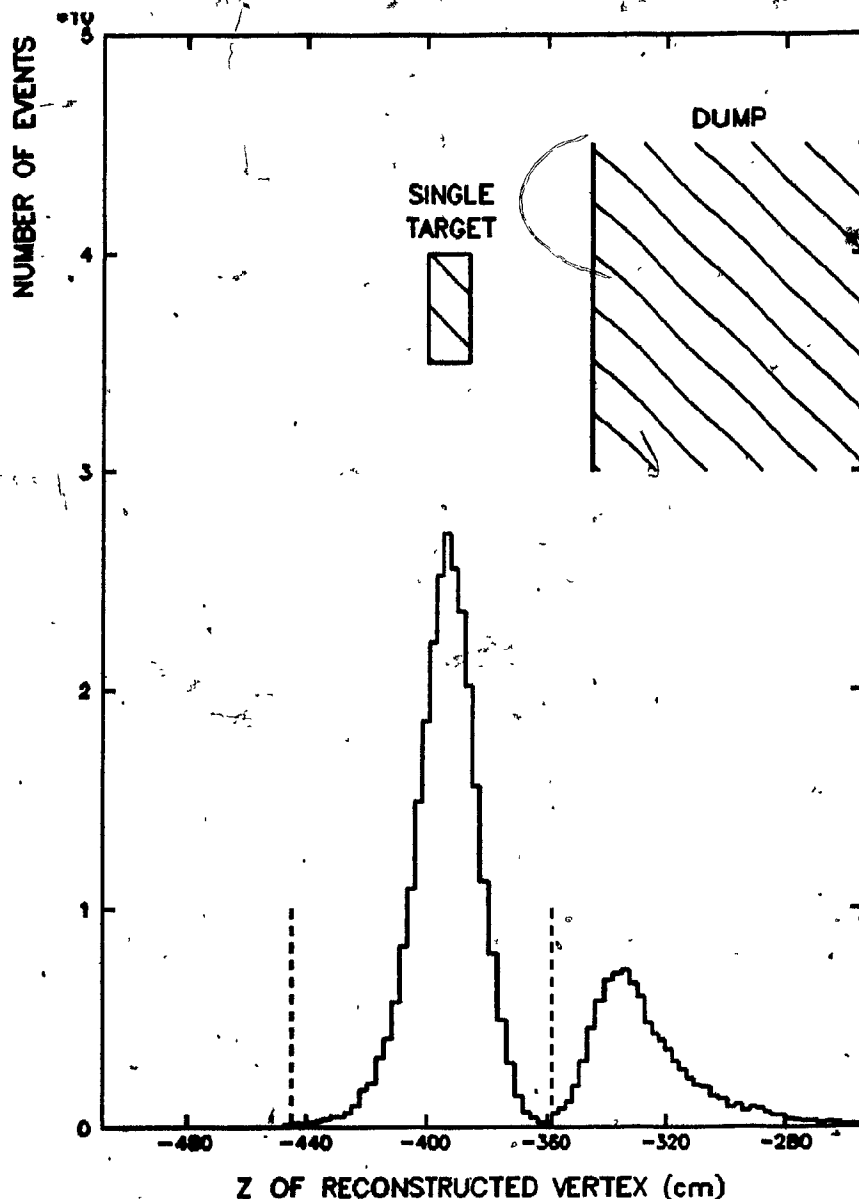
Figure 25 - Reconstructed Vertex

The reconstructed Z vertex position is shown for the tungsten target used during the 1982 run. The positions of the target and the copper beam dump are indicated in the top half of the figure, and the dashed lines show the positions of the vertex cuts. The reconstructed vertex was used to assign the events to either the dump or the target. The kinematic variables for events assigned to the target were recalculated assuming that they had originated at the centre of the target.

be between -444.3 cm and -358.14 cm when the single target was used, and between -495.5 cm and -358.14 cm when a split target was used. The distance of closest approach of the two tracks was required to be less than 7.62 cm in X, 10.16 cm in Y, and 2.54 cm in Z. When these vertex requirements were tested in the Monte Carlo simulation, they resulted in a loss of less than 1 percent of the events with no bias in any of the kinematic variables.

To eliminate any residual contamination by beam halo, special requirements were imposed on events with a high momentum negatively charged muon to ensure that both muons came from a common vertex. Events with a muon of either charge with a momentum of greater than 85 GeV/c were not included in the final data sample. Events with a negative muon with a momentum of greater than 20 GeV/c were excluded from the final data sample if the separation of the tracks at the target was greater than 5.08 cm and if the distance of either track from the reconstructed beam track was greater than 5.08 cm.

The special vertex requirements imposed on events with a high momentum negative muon were studied using the Monte Carlo simulation and by applying them to events with a high momentum positive muon and found to result in a negligible loss. The rejection of events with a muon having a momentum of greater than 85 GeV/c resulted in the loss of a few percent of the oppositely charged high mass events, but eliminated a large fraction of the negative-negative events surviving the other requirements. This requirement had no effect on the kinematic distributions with the exception of the high x_F region. Figures showing the effects of this requirement are presented together with the track finding efficiency in a later section. A correction for these effects was included in the calculation of the acceptance, as discussed in the next chapter.

4.5 Aperture and Trigger Requirements

The reconstructed muon tracks were required to pass through fiducial regions corresponding to the defining apertures of the apparatus. In addition, the tracks were required to point at counters that had been hit in coincidence with the trigger. The muon pair was also required to completely satisfy the trigger conditions that had been imposed during the data taking.

These requirements eliminated most of the events which had satisfied the trigger because of an accidental coincidence between a hadron decay or punch through and a beam halo particle, and guaranteed that counter inefficiencies could be accurately calculated. Because the resolving time of the counters was much smaller than the sensitive time of the drift chambers, it was possible to eliminate tracks from interactions of beam particles in previous RF buckets. The aperture and trigger requirements also ensured that the acceptance of the apparatus could be accurately modelled by making the same requirements in the Monte Carlo.

The X and Y coordinates of the reconstructed tracks were calculated at for various values of Z as listed in Table 5. These correspond to the following physical locations:

1. the edges of the active area of the third drift chamber,

2. the aperture defined by the downstream end of the magnet yoke,

3. the downstream edges of the magnet coils,

Table 5 - Fiducial Regions

This table summarizes the fiducial requirements placed on the reconstructed tracks as discussed in the text. The tracks were required to fall within ±DX and ±DY of the nominal beam centre point at XO and YO at each of the chambers. At chambers DC3 and DC6, additional requirements were also made in U and V. At the absorber counter one of the tracks was required to fall outside a circle of radius DR if signals from the counter were used in the trigger for the event. The tracks were also required to fall outside the beam holes in the CPH and muon counter hodoscopes. The Y coordinate of the beam centre depended on Z because of the upward slope of the beam caused by magnets in the beam spectrometer.

Aperture	ZO (cm)	XO (cm)	YO (cm)	DX (cm)	DY (cm)	DR (cm)	DU (cm)	DV (cm)
Absr Cntr	-174.24	0.0	5.23	25.4	55.88	15.24	-	-
DC3	-137.52	0.0	5.95	24.63	-	-	55.95	55.95
Mgnt Yoke	76.2	0.0	6.17	91.44	45.72	-	-	-
Mgnt Coil	135.3	0.0	6.17	91.44	-	-	-	-
DC4	163.40	0.0	6.746	-	49.53	-	-	-
DC6	414.05	0.0	7.404	167.17		-	174.25	174.25
CPH Hole	441.07	0.0	7.404	15.24	15.24	-	-	-
Muon Cntr	925.20	0.0	8.658	20.32	20.32	-	-	-

4. the edges of the active areas of the fourth and sixth drift chambers,

5. the edges of the beam hole in the CPX and CPY counters, and

6. the edges of the beam hole in the first muon hodoscope.

At the drift chambers and magnet apertures the track coordinates were examined and the event was rejected if they passed outside of a rectangular region of size ±DX and ±DY centred on the nominal beam centre at XO and YO, also listed in Table 5. At the CPX, CPY, and muon hodoscope holes the tracks were rejected if they passed inside of a rectangular region of size ±DX and ±DY centred at XO and YO. Because the active areas of the chambers were not square, the tracks were also required to fall within a region ±DU and ±DV of the nominal beam centre spot at the third and sixth drift chambers, where U and V are defined as

$U = X + Y\tan\theta$,

$V = X - Y\tan\theta$, and

$\theta = \tan^{-1}(0.3)$ is the stereo angle of the U and V planes of the drift chambers.

Both reconstructed muon tracks were required to point to CPX, CPY and muon triple coincidence channels which had been hit in coincidence with the trigger. Half a counter spacing was allowed for resolution at the CPX and the CPY counters and a 12.7 cm margin for multiple scattering was allowed with the muon counters. The two tracks were required to point to muon triple coincidence channels in different quadrants of the hodoscopes. Each muon was required to point to a different CPX counter with a recorded hit to guarantee that the CPX≥2 requirement of the hardware trigger was satisfied.

In addition at least one of the muons was required to pass outside of a circular region corresponding to the absorber counter hole if the trigger for a given event had required the counter. The absorber counter quadrants traversed by the reconstructed tracks were compared to the list of active counters and at least one of the quadrants hit was required to have recorded a count.

4.6 Reconstruction Efficiency

It is difficult to make reconstruction programmes one hundred percent efficient. Missing hits due to chamber inefficiencies, electronics dead time and extra tracks from halo particles or other interactions can confuse even the most carefully written programmes. Our reconstruction efficiency was investigated by generating Monte Carlo events with simulated backgrounds and inefficiencies and reconstructing them with the analysis programmes.

Background hits in the chambers were simulated by using the drift chamber information from events on a special data tape taken using the BEAM signal only as the trigger. Muon pairs generated by the Monte Carlo simulation were propagated through the apparatus using its measured parameters and added to the background drift chamber hits. The drift chambers were assumed to be 99.5 percent efficient, a number consistent with tests using cosmic rays and low intensity beam runs. The dead time of the drift chamber electronics was included by disabling drift chamber wires which had been hit in a second beam event. These simulated data events were analysed with the same programmes as the data events, and the reconstruction efficiency was calculated by comparing the number of events generated to the number surviving the analysis.

The track finding efficiency was typically 90 percent overall for high mass muon pairs produced by antiprotons in the 1982 run. The efficiency (open squares) is shown as a function of the various kinematic variables in Figure 26 and Figure 27. Note that the efficiency is relatively constant for most of the range of the kinematic variables but falls to 80 percent for the highest x_F bin used. Also shown on the figures as solid squares are the efficiencies when the requirement that the individual muon momenta be less than 85 GeV/c, is included. This requirement has little effect on the kinematic distributions with the exception of the high x_F region.

Decreasing the efficiency per plane to 99.0 percent typically decreased the track finding efficiency by 1 percent. Reducing the electronics dead time from 350 ns to 300 ns increased the overall track finding efficiency by 1.2 percent. A calculation of the efficiency using background hits from real reconstructed dimuon data events agreed to within 2 percent with the calculation using background hits from beam triggers.

Comparable results were obtained by independent estimates of the track finding efficency based on the scanning of subsets of the data sample by hand and machine, and by measuring the drift chamber electronics dead time. These estimates are discussed extensively by Kraushaar[85]. A 20 percent residual uncertainty in the track finding inefficiency translates into a 2 percent uncertainty in the final cross section. Including uncertainties in the electronics dead time and the efficiency of the drift chambers, the final uncertainty in the total cross sections is estimated to be less than 4 percent. The maximum correction to any data point is 20 percent, so that the maximum uncertainty in any of the differential cross sections is estimated to be less than 8 percent.
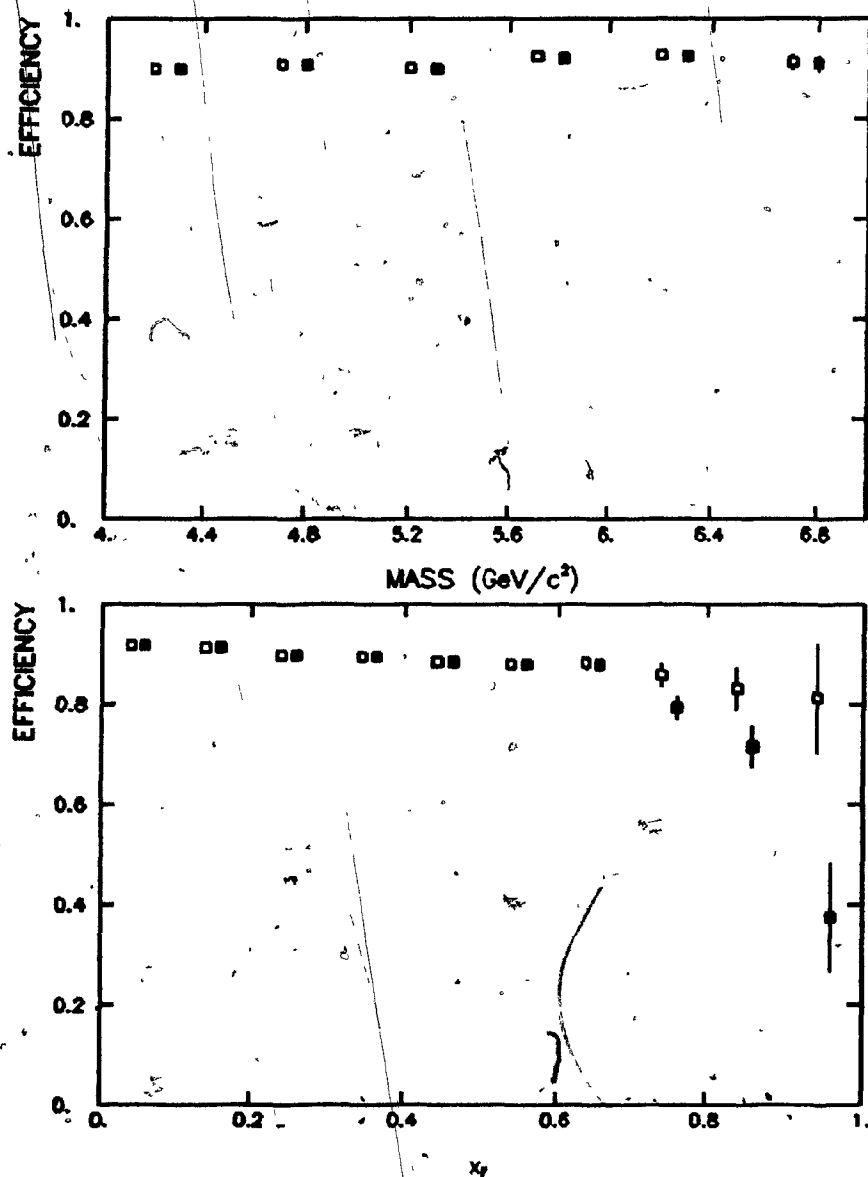
Figure 26 - Track Finding Efficiency vs Mass and x_F

The open squares show the track finding efficiency as functions of mass and x_F for the 1982 running period. The solid squares show the combined effects of track finding efficiency and the kinematic requirements imposed on the reconstructed events. The requirement that both muons have a momentum of less than 85 GeV/c results in the loss of half the events in the highest x_F bins.

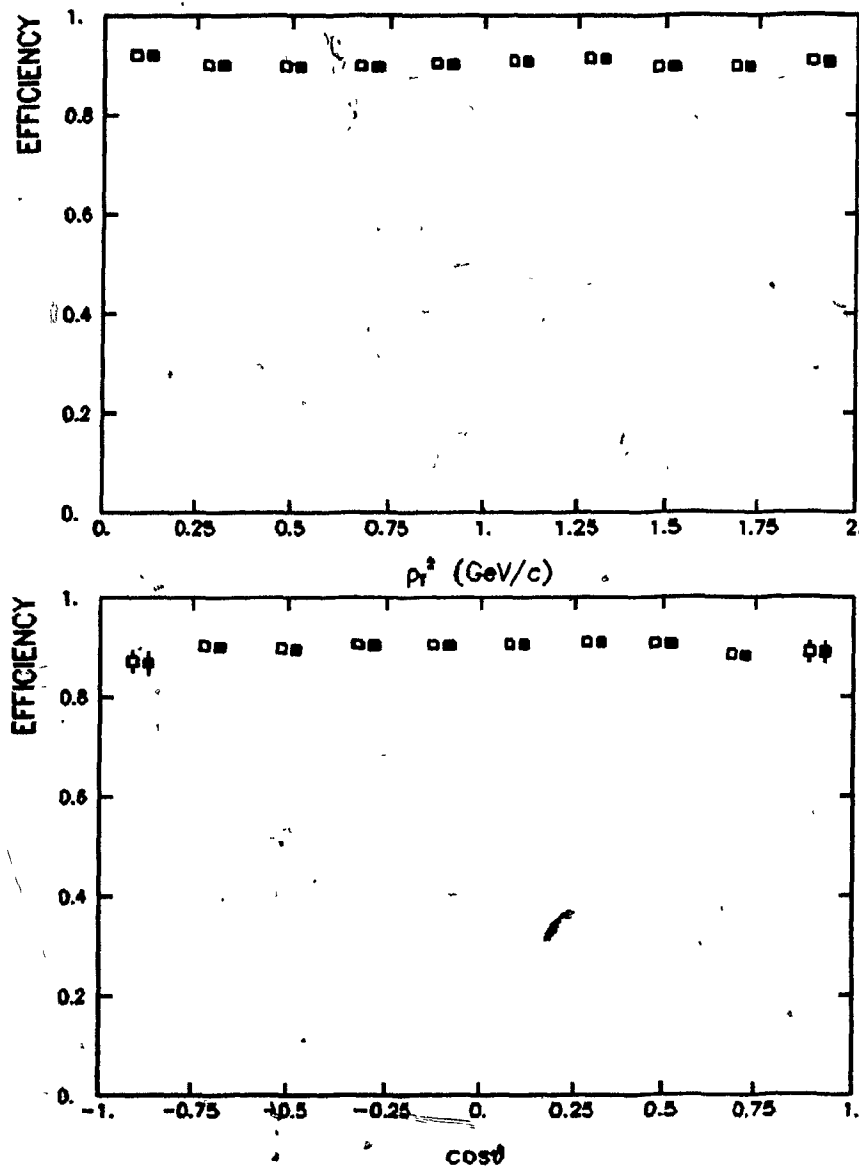Figure 27 - Track Finding Efficiency vs p_T^2 and $\cos\theta$

The open squares show the track finding efficiency as functions of p_T^2 and $\cos\theta$ for the 1982 running period. The solid squares show the combined effects of track finding efficiency and the kinematic requirements imposed on the reconstructed events. There is no strong dependence of the reconstruction efficiency on any of these kinematic variables.

The acceptance of the spectrometer was calculated by generating events with the simulation programme and determining what fraction of them successfully traversed the entire spectrometer. The details of the simulation programme will be discused in the next chapter. The reconstruction efficiency was incorporated by requiring the Monte Carlo events, including background and electronics dead time as decribed here, to be reconstructed with the same series of analysis programmes as the real experimental data.

4.7 Kinematic Reconstruction and Data Sample

The mass resolution of the spectrometer was limited by the uncertainty in the opening angle of the muon pair caused by multiple scattering of the muons in the copper absorber. In the final stage of the analysis, information from the beam chambers and the absorber wire chamber was used to determine the opening angle of the muon pair and thereby give the best resolution for the spectrometer. The four momenta of the muons were then recalculated using this procedure and used to calculate the kinematic variables of the muon pair.

The muon pairs could be assumed to have been created by the interaction of a beam particle in the target. Monte Carlo simulations showed that the measurement of the opening angle could be improved by assuming that the muons had originated at the centre of the target rather than just using the drift chamber tracks to determine the Z position of the vertex. The beam track was used to provide the X and Y coordinate positions of the production vertex. The absorber chamber gave information about the positions of the tracks before they had been fully scattered, and could be used to give the

best determination of the opening angle. To do this, the drift chamber
tracks in the front of the magnet were projected back to the centre plane of
the absorber chamber. A radial area of 1.016 cm around the tracks was
searched for hits. The X and Y positions of the track in the absorber
chamber were taken to be the crossing point of the U and V wires closest to
the track. Line segments linking the absorber chamber coordinates with the
centre of the target segment in which the event was produced were used to
give the final values of the production angles of the muons.

The effects of different reconstruction procedures on the width of the
ψ peak were examined. Using only the tracks in the front drift chambers to
calculate the production angles of the muons gave a ψ peak with a width of
270 MeV/c^2. Using line segments linking the drift chamber tracks in the
front chambers to the centre of the target segment gave a width of
190 MeV/c^2. Incorporating the absorber chamber information reduced the width
of the peak to 185 MeV/c^2.

The four momenta of the muons were recalculated using the best values
for the direction of each muon. The beam-target centre of mass was
calculated from the measured four momentum of the beam particle assuming
that the target particle was a nucleon at rest in the lab frame. The muons
were Lorentz transformed to the centre of mass frame and used to calculate
the invariant mass, x_F, p_T, and rest frame parameters of the pair as
described above in Chapter 2. The individual muons and the beam and target
particles were transformed from the centre of mass frame to the rest frame
of the muon pair and the angular variables, θ and ϕ, were calculated using
the Gottfreid-Jackson convention for the Z axis.

Although data was taken using copper and beryllium targets so that the A dependence of the cross section for ψ production could be investigated, this analysis is based on the tungsten data only. The breakdown of the final data sample by beam type and trigger condition is given in Table 6. The mass spectra for muon pairs produced by antiprotons and pions in all the tungsten targets are shown in Figure 28 and Figure 29 respectively. No correction for the acceptance of the spectrometer has been applied at this stage. The open squares are the sum of events with either two positively or two negatively charged muons. The ψ peak observed at the correct mass of 3.1GeV/c^2 has a width consistent with the calculated resolution of the spectrometer.

The next chapter describes the Monte Carlo computer programme used to calculate the acceptance. The fitting of the kinematic distributions, the corrections applied to the data, and the results are discussed in subsequent chapters.

Table 6 - Breakdown of Events by Target Configuration

This table summarizes the number of reconstructed high mass muon pairs with M between 4 and 9 GeV/c^2 and $x_F \geq 0$. Oppositely charged and like charged pairs are listed in separate columns.

		Antiprotons		Pions	
Target	Trigger	+-	++/--	+-	++/--
BE	TRIG1	10	-	-	-
	TRIG2	3	-	56	-
CU	TRIG1	-	-	-	-
	TRIG2	20	-	70	1
W	TRIG1	-	-	-	-
	TRIG2	106	-	367	2
THICK W	TRIG1	250	5	102	1
	TRIG2	17	-	578	9
THIN W	TRIG1	14	-	-	-
	TRIG2	-	-	54	-
TOTAL W		387	5	1101	12

Figure 28 - Uncorrected Antiproton Produced Mass Spectrum

The solid squares show the number of oppositely charged muon pairs produced
in antiproton-tungsten collisions as a function of mass. The open squares
show the sum of pairs of positively charged muons and pairs of negatively
charged muons.
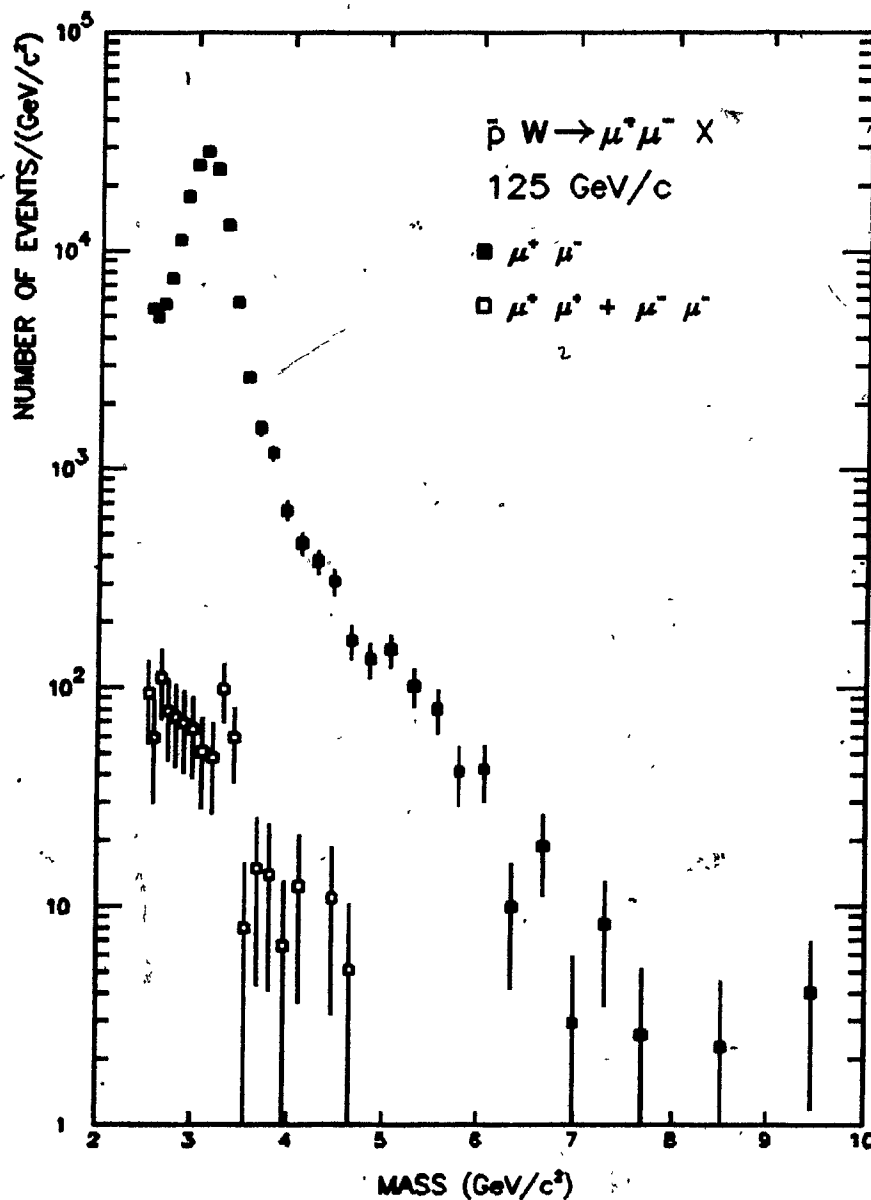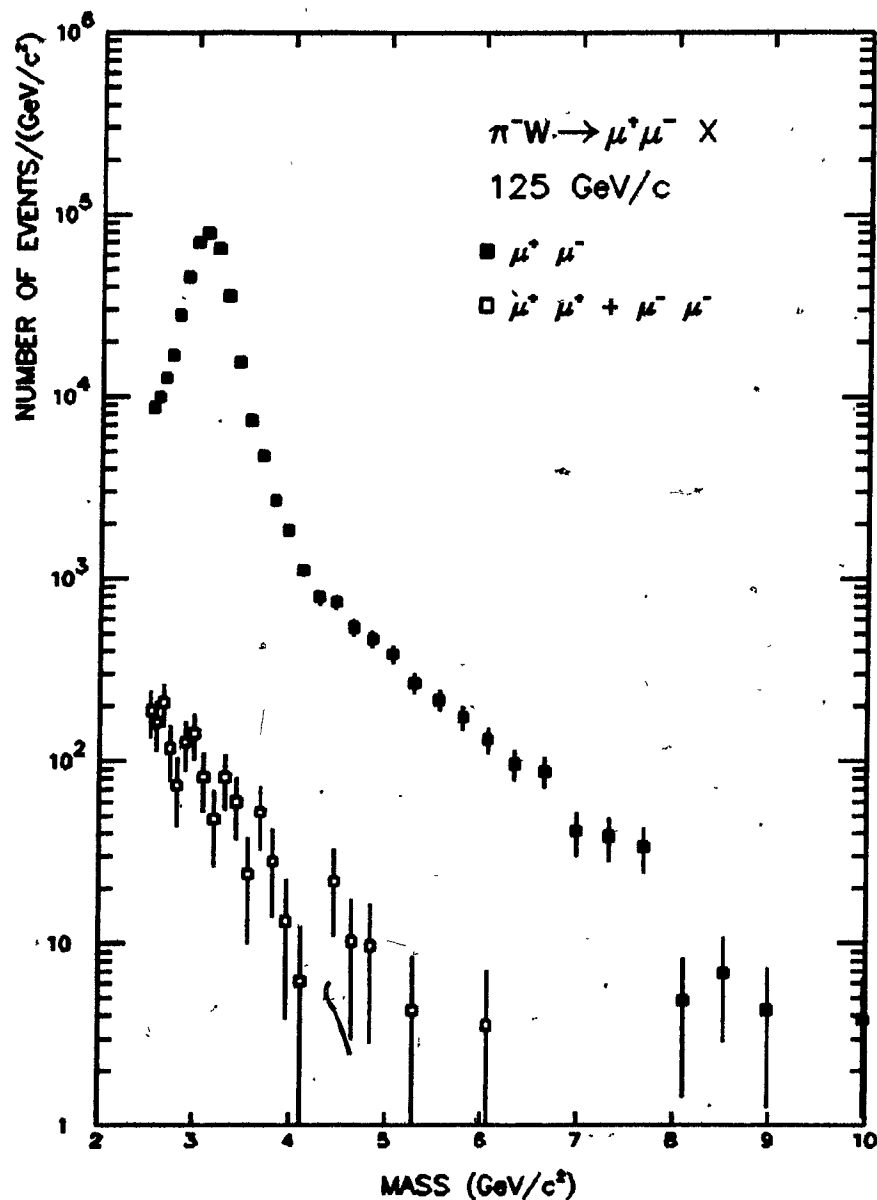
Figure 29 - Uncorrected Pion Produced Mass Spectrum

The solid squares show the number of oppositely charged muon pairs produced in pion-tungsten collisions as a function of mass. The open squares show the sum of pairs of positively charged muons and pairs of negatively charged muons.

CHAPTER 5

Monte Carlo

The largest correction that had to be made to the data was for the limited acceptance of the spectrometer itself. A FORTRAN Monte Carlo programme was written for the Fermilab Cyber 175 computer[86] to model the apparatus and calculate the acceptance.

The programme sought to simulate the apparatus as closely as possible. Events were generated randomly throughout phase space using the measured beam energy spectra and profiles, and the resulting pairs of muons were propagated through the spectrometer taking into account multiple scattering, energy loss, and the Fermi motion of the target nucleon. The track positions at the chambers were digitized, the counters hit were recorded, and the results were written to a disk file in the same format as the data events. Background hits were included as described in the last chapter to allow for electronics dead time and give the same pattern recognition

efficiency as for the data events. The events were subject to the same set of analysis programmes and the same trigger and aperture requirements as the data events. Both the generated and reconstructed kinematic variables of each Monte Carlo event were stored on the disk file.

This chapter describes the details of the simulation programme itself and the mechanics associated with reweighting events. The list of events generated summarized all of the information about the acceptance of the spectrometer and it could be read and reweighted by the fitting programmes, as described in the next chapter, without repeating the entire Monte Carlo calculation.

This Monte Carlo programme was compared to an independently written programme[89]. Each programme generated 1.0×10^5 antiproton produced muon pairs using the kinematic distributions given below. The programmes were found to agree on both the absolute values and shapes of the acceptance as a function of the kinematic variables to within statistical errors.

5.1 Beam Particle

The four vector of the beam particle was selected from files of beam momenta taken from the data summary tapes to give the correct beam profile and momentum distribution in the Monte Carlo. The files contained approximately 9000 and 15000 events for the 1981 and 1982 data runs respectively.

5.2 Target Particle

The four vector of the target nucleon was generated according to a simple Fermi gas model[90] to take into account the motion of the nucleons inside the heavy target. The target nucleon was given an isotropic angular distribution in the laboratory frame with momentum distributed between 0 and the Fermi momentum as follows:

$$\frac{dN}{dp} = 3p^2/p_{Fermi}^3 .$$

The Fermi momentum for the various targets was taken as[91][92][93]

$$p_{Fermi}(Be) = 0.203 \text{ GeV/c},$$

$$p_{Fermi}(Cu) = 0.250 \text{ GeV/c, and}$$

$$p_{Fermi}(W) = 0.265 \text{ GeV/c}.$$

The effect of including high momentum tails[94] in the Fermi distribution was investigated in the simulation and found not to be significant.

5.3 Event Generation

For each muon pair in the continuum region, the five kinematic variables and a random azimuthal angle about the beam direction were generated according to the following unnormalized distributions in the beam-target centre of mass system:

$$\frac{dN}{dM} = \exp(-\alpha_M M),$$

$$\frac{dN}{dx_F} = \exp(-\frac{1}{2}(\frac{x_F - x_{F0}}{\sigma_{x_F}})^2),$$

$$\frac{dN}{dp_T} = p_T[1+(\frac{p_T}{p_{T0}})^2]^{\alpha_{p_T}},$$

$$\frac{dN}{d\cos\theta} = 1+\lambda\cos^2\theta, \text{ and}$$

$$\frac{dN}{d\phi} = 1.$$

The parameters used in the distributions were taken from a preliminary analysis of the data[95] and are as follows:

$$\alpha_M = 1.26$$

$$x_{F_0} = 0.0,$$

$$\sigma_{x_F} = 0.27,$$

$$p_{T_0} = 3.1,$$

$$\alpha_{p_T} = -10.2, \text{ and}$$

$$\lambda = 1.0$$

for antiproton produced pairs; and

$$\alpha_M = 1.0$$

$$x_{F_0} = 0.0,$$

$$\sigma_{x_F} = 0.37,$$

$$p_{T_0} = 3.1$$

$$\alpha_{p_T} = -9.3, \text{ and}$$

$$\lambda = 1.0$$

for pion produced pairs.

To minimize computer time, the mass and p_T^- of the muon pair were calculated by integrating the probability distributions and inverting the equations to find M and p_T in terms of the cumulative probabilities as described by James in his review of Monte Carlo techniques[96]. For example, the mass distribution normalized to unit probability between M_{min} and M_{max} is given by

$$dP = \alpha_M \cdot \exp(\alpha_M(M_{min}-M)) \cdot dM \cdot [1-\exp(\alpha_M(M_{min}-M_{max}))]^{-1}.$$

Defining the cumulative probability distribution to be

$$y(M) = \int_{M_{min}}^{M_{max}} dP.$$

and inverting to obtain M in terms of y, we find

$$M = M_{min} - \frac{1}{\alpha_M} \ln[1 - y \cdot \exp(\alpha_M(M_{min}-M_{max}))].$$

The random number generator, RANF[97], was used to give a value of y uniformly distributed between 0 and 1, and the mass was then calculated from the equation above. The x_F distribution was obtained by scaling a normally distributed random number generated by the CERN library programme NORRAN[98][99]. Because the inversion of the cumulative probability of the cosθ distribution involves the solution of a cubic equation, the standard technique of generating a random value for cosθ between ±1 but using it only if a second random number between 0 and 1 was less than $[1+\cos^2\theta]/2$, was used instead.

The kinematic quantities were used to calculate the four vectors of the two muons in the beam-target centre of mass frame. The CERN library routine LORENC[100] was used to transform the beam and target four momenta from the laboratory frame to the beam-target centre of mass frame. The values of x_F, P_T, and the azimuthal angle of the pair about the beam direction were used to calculate the motion of the muon pair in the centre of mass frame. The beam and target particles were transformed to the muon pair rest frame and used to calculate the X, Y and Z axes of the Gottfreid-Jackson frame. A unit vector along the Z axis was scaled to give a muon energy of M/2 in the rest frame of the pair. The vector was rotated by an angle of θ about the Y axis and then by an angle of φ about the Z axis to give the three momentum vector of the positive muon in the rest frame of the pair. The three momentum of the negative muon was taken as equal and opposite. The muon

four vectors were transformed back to the beam-target centre of mass system and then to the laboratory frame. Whenever possible library subroutines were used to manipulate the vectors to simplify the code and speed programme development.

5.4 Target and Dump

The X and Y coordinates of the production vertex were taken from the file of reconstructed beam momenta in order to reproduce the measured beam profile and include any correlations between the spatial and momentum distributions. The Z coordinate of the production vertex was generated according to an exponentially decaying distribution using the same technique used to generate the mass. The decay length used in the exponential was the absorption length of the target material for the specific beam particle type. The absorption lengths were taken from experimental measurements by Carroll[101] and are listed in Table 2. The four vectors discussed in the last section were used to give the initial directions and momenta for the two muons.

The muons were propagated through the remainder of the target using the Gaussian multiple scattering distribution discussed in Appendix II. In the limit of small scattering angles, negligible energy loss, and many individual scatters, the probability projected on the Y-Z plane that a particle travelling along the Z axis and entering a scatterer at $Y = Z = 0$ will emerge a distance Y from the Z axis with an angle θ_Y with respect to the Z axis, is given by

$$P(Y, \theta_Y | Z) = \frac{2\sqrt{3}}{\pi \theta_{YRMS}^2 Z^2} \exp\left(- \frac{4}{\theta_{YRMS}^2 Z}(\theta_Y - 3\theta_Y\psi + 3\psi^2)\right)$$

where ψ is the dimensionless ratio

$$\psi = Y/Z, \text{ and}$$

the projected RMS scattering angle is given by[13]

$$\theta_{YRMS} = \frac{0.015}{\beta p} \sqrt{\frac{Z}{Z_{rad}}},$$

and

β is the velocity of the particle in units of c,

p is the momentum of the track in GeV/c,

Z is the length of the scatterer, and

Z_{rad} is the radiation length[13] for the particular target material.
A similar expression also holds for the X-Z plane.

The muon momenta in the laboratory frame were also corrected for energy loss in the target using tables[102][103] calculated from the Bethe-Bloch ionization formula with corrections for density effect, bremsstrahlung, and nuclear interactions. The tables of energy loss for tungsten, copper, beryllium, iron and concrete were parameterized for kinetic energies between 100 MeV/c and 125 GeV/c, and these are shown in Figure 30. The parameterization for iron was compared with other references in the literature[104][88] and found to agree to better than 1 percent for muon energies in the range of interest.

The muons were also propagated through the beam dump taking into account scattering and energy loss as in the target. The track coordinates at the absorber chamber were recorded for use in the reconstruction.
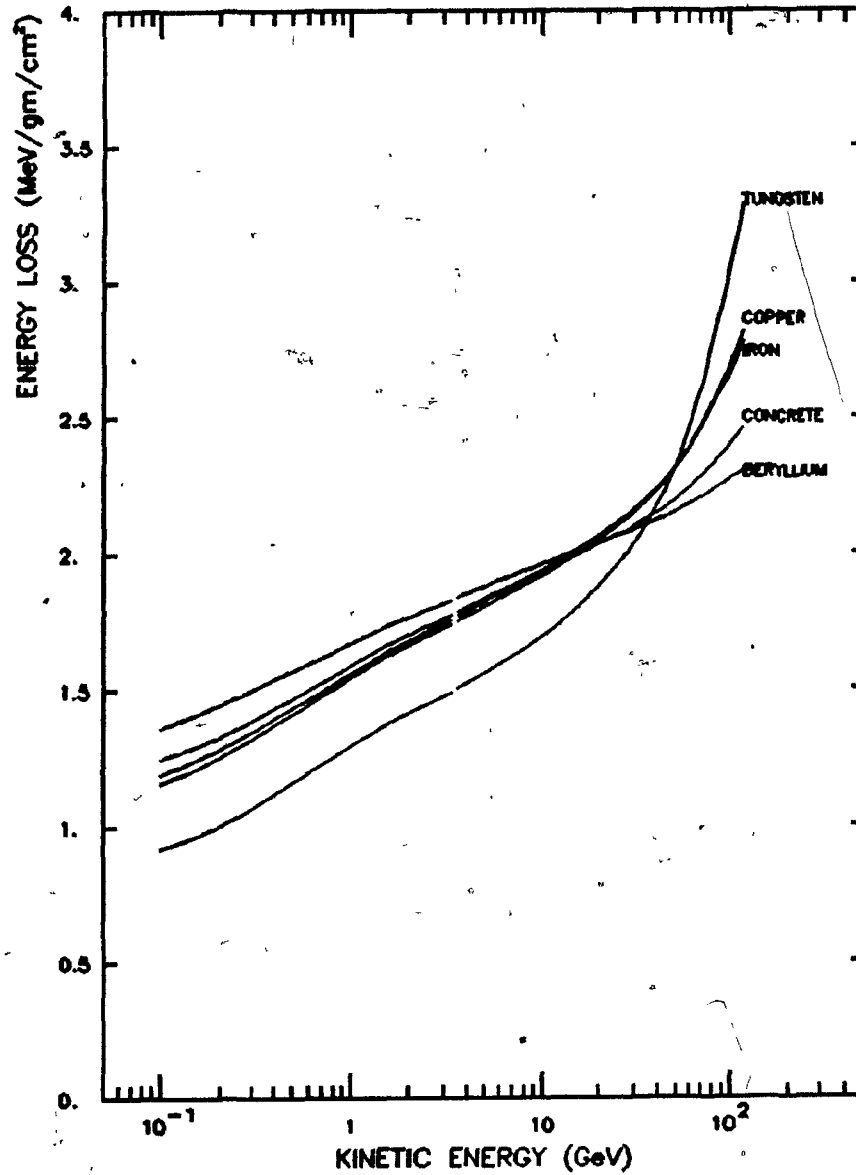
Figure 30 - Energy Loss for Muons

The energy loss for muons in the various materials used in the spectrometer is shown as a function of the kinetic energy of the muon.

5.5 Spectrometer

Muons emerging from the dump were required to pass through regions corresponding to the physical apertures of the front chambers. The trajectories of both muons were examined to determine whether either muon had passed through an absorber counter quadrant. If both muons passed within all of the physical apertures upstream of the magnet, the particles were propagated through the magnetic field using a square field of effective length 2.03 m and central field value 13.6 Kgauss. The tracks were also required to pass through apertures corresponding to the physical dimensions of the magnet field region. Downstream of the magnet, the tracks were checked to make sure that they passed through the drift chambers and CPX and CPY hodoscope counter arrays.

5.6 Muon Hodoscopes and Trigger

Muons tracks passing through all the apertures of the spectrometer were propagated through the muon filter walls taking into account energy loss and multiple scattering as had been done in the target and beam dump. Tracks were required to hit apertures corresponding to the muon hodoscope counter arrays. Counters hit by the tracks were combined to form triple coincidence channels identical to the corresponding hardware channels. The information from these triple coincidences was then combined with the absorber counter information to decide whether the event should be rejected, accepted by the level 1 trigger, or accepted by the level 2 trigger.

5.7 Trigger Processor

The trigger processor algorithm was applied to all events accepted by the software simulation of the apparatus. The track coordinates in the rear drift chambers were digitized and used to calculate the projected slope, dX/dZ, downstream of the magnet. The track positions at the CPY hodoscope were used to give the slope dY/dZ. The downstream track was projected to the magnet bend plane and used to determine the muon momentum assuming that the production vertex was at the centre of the target. The mass of the muon pair was calculated using the approximation

$$M^2 \approx p_1 p_2 \theta^2$$

where p_1 and p_2 are the individual muon momenta and θ is the opening angle between them in the laboratory frame. Only events reconstructing to a mass of greater than 2.0 GeV/c^2 were accepted.

5.8 Reconstruction

To take into account any dependence of the reconstruction efficiency on the kinematic variables of the muon pairs, all of the Monte Carlo events were reconstructed by the analysis programmes used for the real data as described in the last chapter. Events accepted by the software model of the spectrometer were digitized and recorded on a disk file in the original data format. Drift chamber hits from events triggered by beam particles were used to simulate background hits in the chambers. Events from the same beam runs were also used to calculate the inefficiency of the chambers resulting from the dead time in the electronics. An efficiency per plane of 99.5 percent was used for the drift chambers and the electronics dead time was

taken to be 300 ns. The Monte Carlo events were processed by the complete set of analysis programmes and a list of generated and reconstructed kinematic variables was stored on tape for use by the fitting programme.

5.9 Reweighting Events

The calculation of the acceptance using the simulation programme can be viewed as the approximation of an integral by Monte Carlo methods. The reweighting of Monte Carlo events is then equivalent to using the specific technique of importance sampling. Economic considerations require the reweighting of events. The justifications for Monte Carlo evaluation of integrals, comparisons with other methods of numerical integration, importance sampling, and the attendant errors are discussed by James[96], in his review of Monte Carlo methods, and in a book by Schreider[105].

As discussed previously, the Monte Carlo events were generated assuming that the muon pairs were distributed in phase space according to a multidimensional distribution, $G(X)$, where

$$X = (M, x_F, p_T, \ldots)$$

is the set of kinematic variables, and can be considered to include other parameters such as the azimuthal angle about the beam, multiple scattering angles, and nucleon momenta due to Fermi motion. For a given event X, the acceptance is either 1 or 0; the event is either accepted or it is rejected. The calculation of the overall acceptance of the apparatus is equivalent to the evaluation of an integral, that is,

$$I = \int A(X)G(X)dX,$$

where $G(X)$ is normalized such that

$$\int G(X)dX = 1.$$

The evaluation is accomplished by making the approximation

$$\int G(X)A(X)dX = \frac{1}{N} \sum_{i=1}^{N} A(X_i) ,$$

where the X_i are N points randomly distributed according to the multidimensional distribution $G(X)$.

As will become clear in the next chapter, it is necessary to be able to evaluate the acceptance for other multidimensional distributions such as $F(X)$. It is possible to repeat the simulation with the new distributions, but the generation and tracking of the events is an expensive process requiring substantial amounts of computer time. A more economical alternative is to run the simulation once using an initial distribution, $G(X)$, and record a list of the kinematic variables for each event and whether or not the event was accepted. The acceptance can then be evaluated for any other distribution, $F(X)$, normalized such that

$$\int F(X)dX = 1$$

by assigning each event a weight of $F(X_i)/G(X_i)$. This gives for the new distribution

$$I' = \int F(X)A(X)dX = \frac{1}{N} \sum_{i=1}^{N} A(X_i)F(X_i)/G(X_i)$$

where the X_i are the same N points, randomly distributed according to the multidimensional distribution $G(X)$.

5.10 Acceptance

The data must be corrected for the acceptance of the spectrometer, but the acceptance in turn depends on the kinematic distributions of the data. The final acceptance of the spectrometer was calculated using the results from fits described in the next chapter. The acceptance for high mass muon pairs produced by antiprotons as a function of the kinematic variables is

Figure 31 — Acceptance vs Mass and x_F for Antiprotons

The upper figure shows the acceptance of the spectrometer for high mass muon pairs produced in antiproton-tungsten collisions as a function of the invariant mass of the pair. The lower figure shows the acceptance as a function of the longitudinal momentum of the pair, expressed in terms of the dimensionless variable x_F.

Figure 32 - Acceptance vs $p_T{}^2$, $\cos\theta$ and ϕ for Antiprotons

The upper figure shows the acceptance of the spectrometer for high mass muon pairs produced in antiproton-tungsten tungsten nucleus collisions as a function of the transverse momentum of the pair. The central and lower figures show the acceptance as a function of the decay parameters $\cos\theta$ and ϕ respectively.

shown in Figure 31 and Figure 32 and the acceptance for pion produced pairs is shown in Figure 33 and Figure 34. Note that the overall acceptance is typically 20 percent for both antiproton and pion produced pairs. The acceptance does not vary rapidly for most of the range of the kinematic variables but does fall sharply at high values of $\cos^2\theta$ and for negative values of x_F. In both of these cases, one of the muons of the pair did not have enough energy in the laboratory frame to traverse the entire apparatus, since a muon required an inital momentum of 6 GeV/c to penetrate to the final muon counter hodoscope. The acceptance for pion produced pairs also falls off at very high x_F because these events were required to satisfy more stringent trigger requirements during most of the data taking.
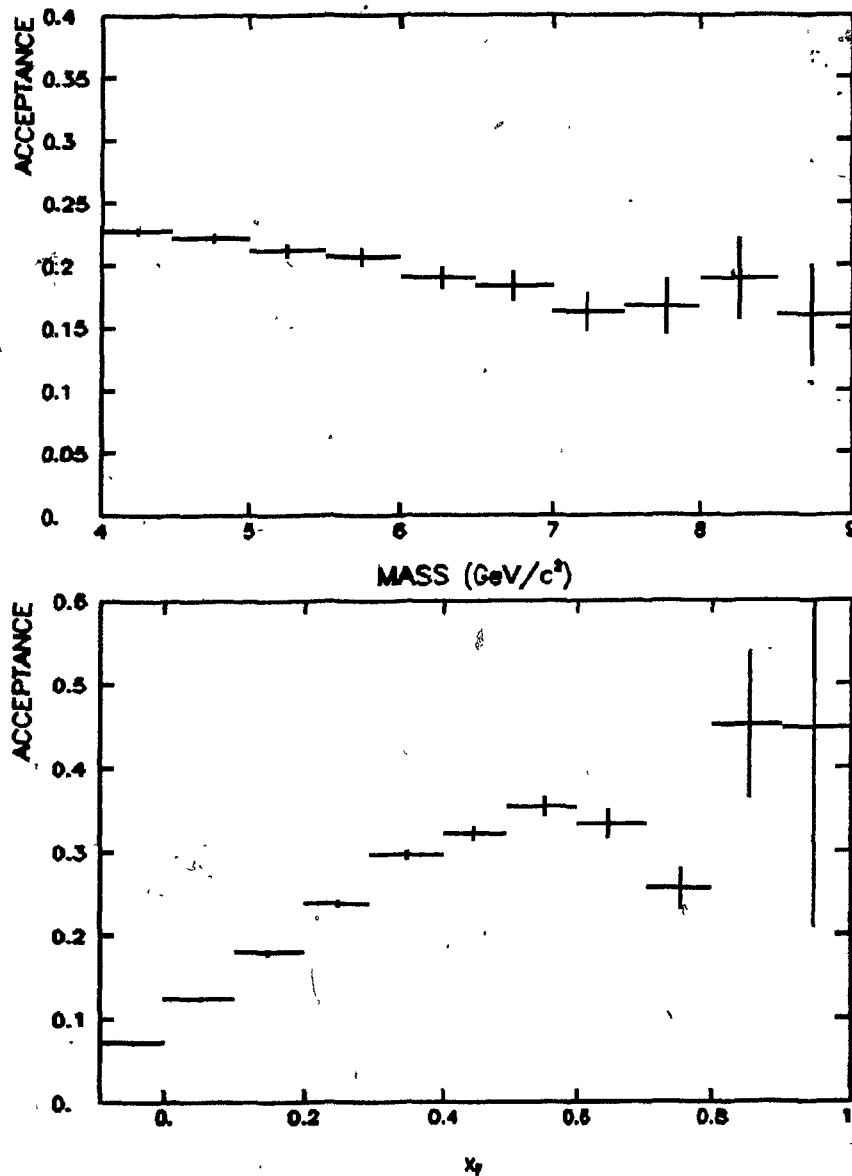
Figure 33 - Acceptance vs Mass and x_F for Pions

The upper figure shows the acceptance of the spectrometer for high mass muon pairs produced in pion-tungsten nucleus collisions as a function of the invariant mass of the pair. The lower figure shows the acceptance as a function of the longitudinal momentum of the pair, expressed in terms of the dimensionless variable x_F.
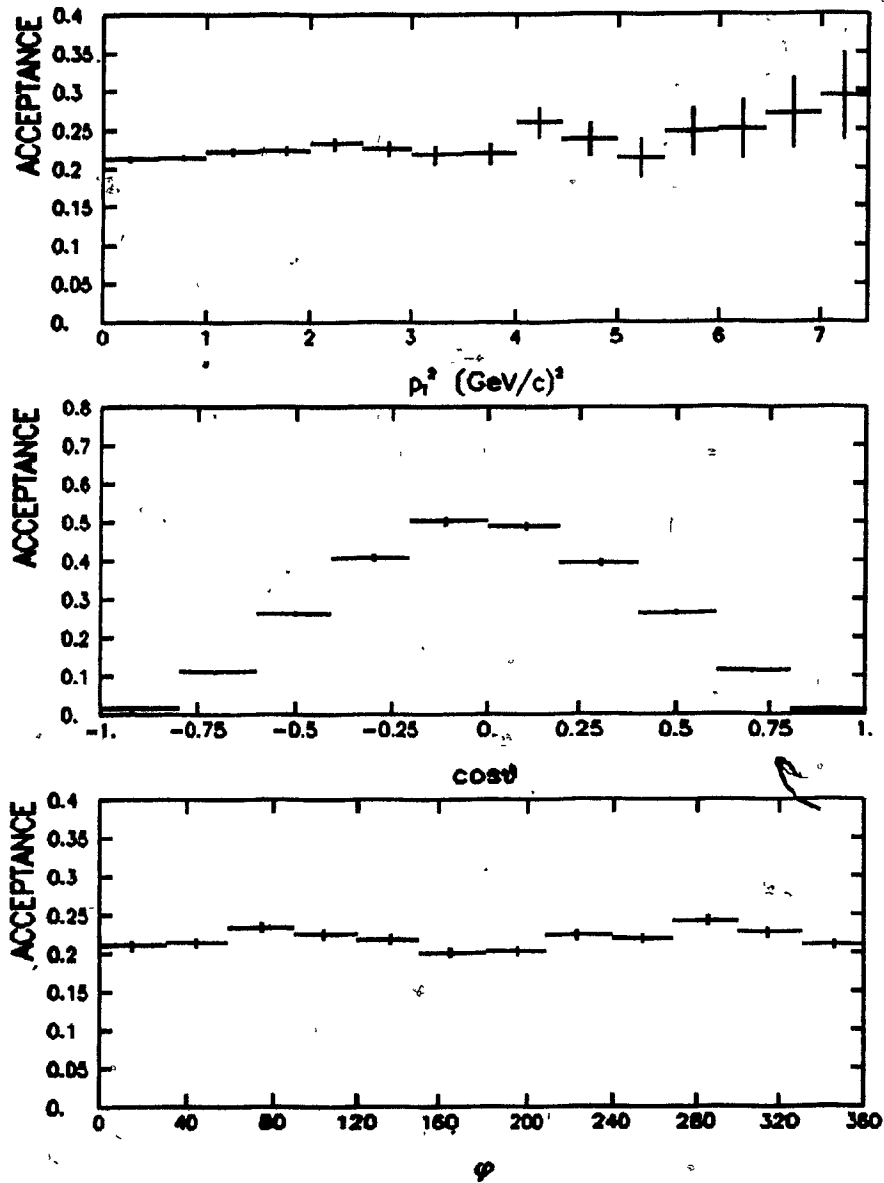
Figure 34 – Acceptance vs p_T^2, $\cos\theta$ and ϕ for Pions
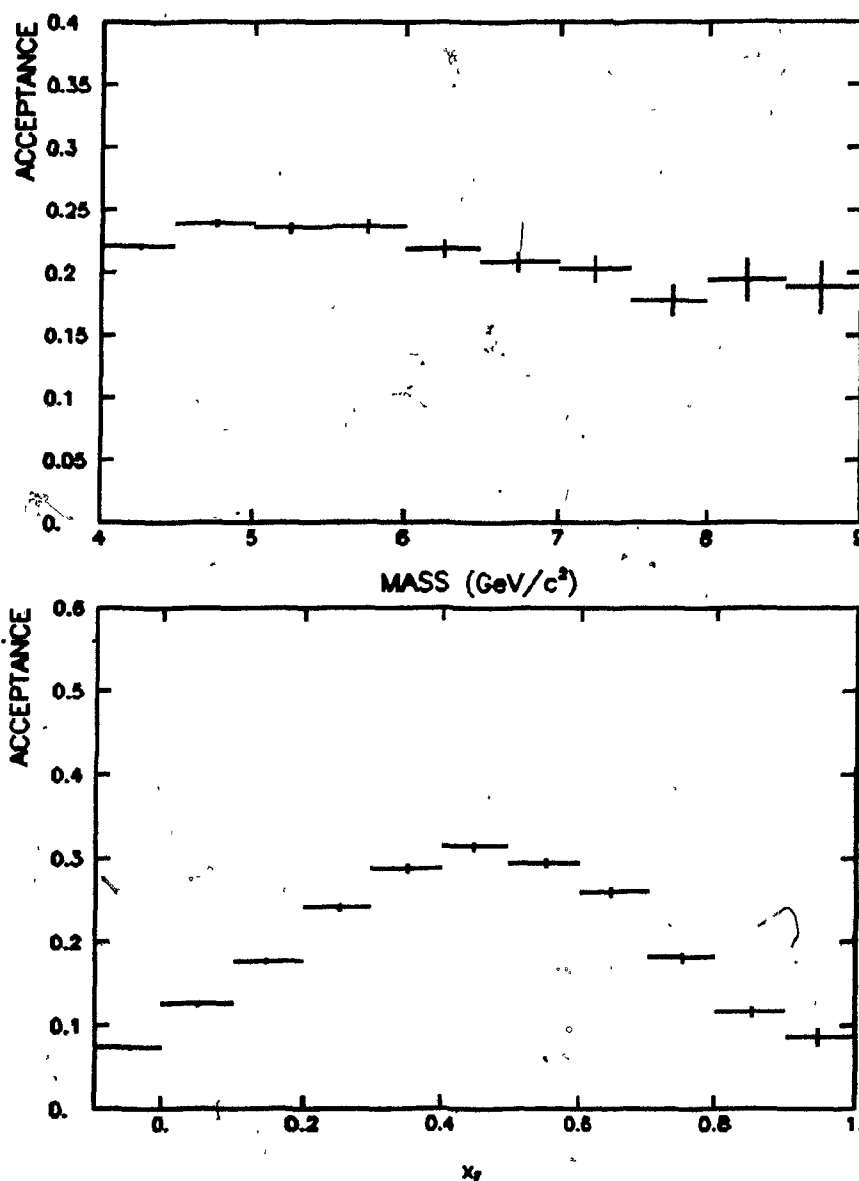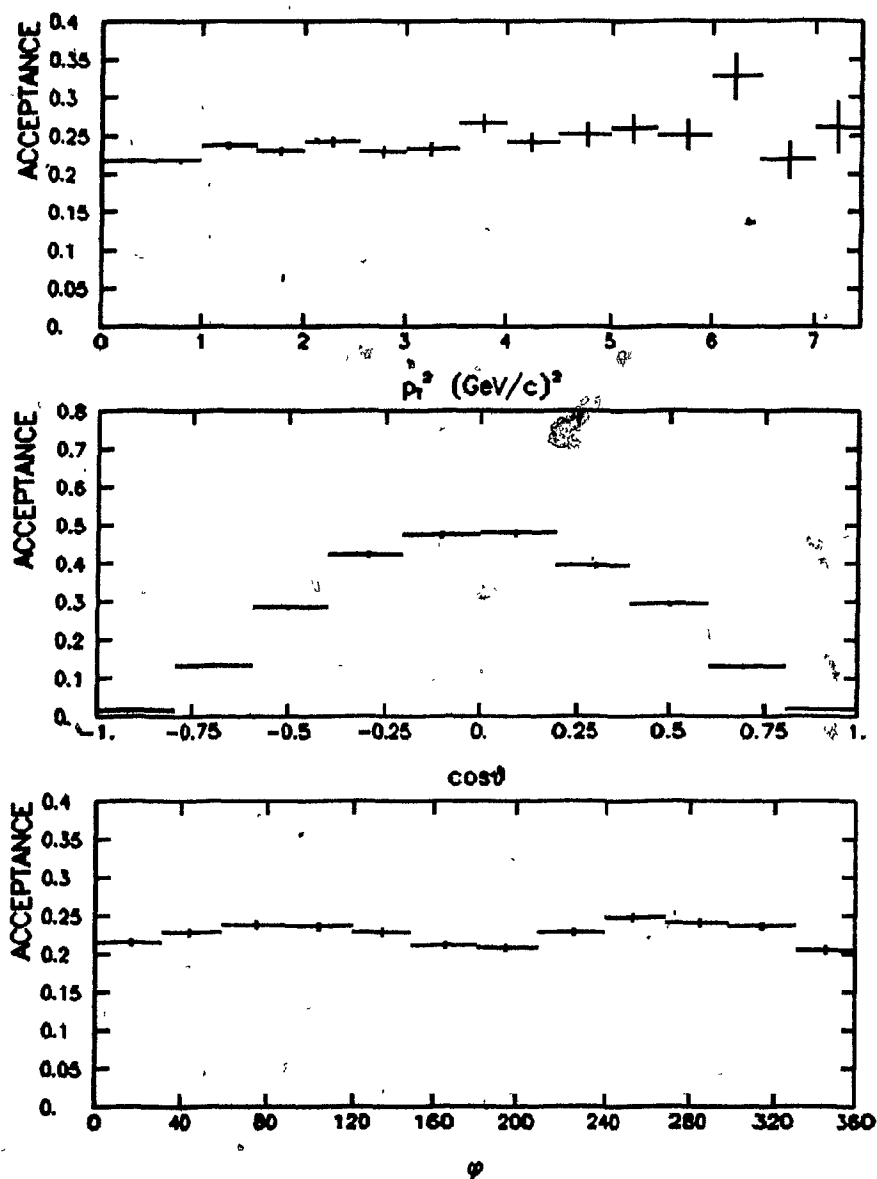
The upper figure shows the acceptance of the spectrometer for high mass muon pairs produced in pion-tungsten nucleus collisions as a function of the transverse momentum of the pair. The central and lower figures show the acceptance as a function of the decay parameters $\cos\theta$ and ϕ respectively.

CHAPTER 6

Analysis

Ideally the cross section per nucleon can be obtained by dividing the number of events observed by the number of beam particles and normalizing to the effective number of nucleons per cm^2 in the target. In practice, the apparatus is not one hundred percent efficient and has limited acceptance. An accidental coincidence between a halo particle and a muon from hadron decay can mimic a muon pair. In thick targets, secondary hadrons can interact and produce real muon pairs. Corrections must be applied for all of these effects.

The reconstruction of the kinematic variables of the muon pair events was discussed in chapter 4. A list of the variables for each reconstructed event was stored on a disk file by the analysis programmes. The generation of a similar list of Monte Carlo events, summarizing the complete knowledge of the acceptance of the apparatus, was discussed in the last chapter. The

maximum likelihood method was used to fit the unbinned data events to empirical parameterizations of the kinematic distributions, and the acceptance of the spectrometer was recalculated at each step of the fit by reweighting the list of Monte Carlo events. The contamination of the data sample by accidental coincidences between uncorrelated muons was evaluated by examining the number of positively and negatively charged muon pairs. A correction for this background was made by subtracting the number of like charged pairs from the number of oppositely charged pairs on a bin by bin basis. The contamination of the data sample by muon pairs produced by reinteracting secondary particles was determined by examining the ψ cross section as a function of the length of the target. A correction for contamination of the high mass region by muon pairs produced in the decay of the ψ' resonance was also applied to the total cross section. Corrections were made to the beam flux to take into account any confusion caused by multiple beam particles in the same RF beam bucket.

These corrections and any resulting systematic uncertainties are discussed in this chapter. The final cross sections and kinematic distributions are presented in the next chapter.

6.1 Fitting and Acceptance

A common approach to multidimensional fitting in particle physics is the fitting of the data in projection[106]. The experimental apparatus as a rule has limited acceptance in some regions of phase space. The parent distributions of the data points can only be determined as well as the acceptance is known, but the acceptance in turn depends on the parent distributions of the data. The data points are binned separately in each of

the variables, that is, projected onto the axes of the multidimensional space to obtain a number of one or two dimensional distributions. The acceptance is calculated for each of the projections using some initial guess for the parent distributions. The one dimensional projections are then corrected for acceptance and fit to the same parameterizations using the least squares method. The results of the fit are used to recalculate the acceptance and the process is repeated until there is no difference between the parameters used to calculate the acceptance and the parameters obtained from the fit.

In principle, it is possible to bin the data points multidimensionally and fit them using the least squares method, but the number of bins that must be used grows rapidly when the number of dimensions exceeds two or three. The least squares method does not handle bins with 0 or 1 event gracefully; this is a problem that occurs when a small number of events are binned in a large number of dimensions. Binning events also results in a loss of information. Since the maximum likelihood method can work with the unbinned data, all of the information is used. If the data is not binned, no problems can arise because bins contain small numbers of events. In the asymptotic limit, as the number of data points to be fit approaches infinity, parameter estimates from the maximum likelihood method are unbiased and normally distributed with minimum variance, or, in other words, asymptotically no other method can do better.

The maximum likelihood method is not without disadvantages. In general the maximum likelihood method is more expensive (uses more computer time) than other methods. The asymptotic properties do not necessarily hold for finite numbers of events. As Eadie[107] has pointed out, the fact that all

of the information is used does not imply that it is necessarily used in the best way. On the whole, however, the maximum likelihood method still provides the best way to extract information from a limited number of events. One advantage over the usual approach of fitting in projection that should not be underestimated is the presence of an objective convergence criteria. Computing stops when the likelihood function has been maximized and not when the experimenter feels that nothing is to be gained by further iteration.

To fit the data points using the maximum likelihood method, the individual kinematic distributions were parameterized using simple functional forms which were multiplied together to obtain a multidimensional distribution. The multidimensional distribution was used to give the probability of observing a set of data events as a function of the parameters. All of the distributions were fit simultaneously by finding the set of parameters which maximized the probability of observing the experimental data points. The acceptance was recalculated at each step of the fit by reweighting the list of Monte Carlo events, as discussed in the last chapter. The maximum likelihood method is treated in some detail in the books by Eadie[107], and by Frodesen[108] and will only be outlined here.

The mass distribution was parameterized with a falling exponential which was normalized to unity between M_{min} and M_{max}, that is,

$$P(M) = \alpha_M \exp(-\alpha_M M) \cdot [\exp(-\alpha_M M_{min}) - \exp(-\alpha_M M_{max})]^{-1}$$

A Johnson bounded empirical distribution[109], a transformation of a Gaussian designed to fall off to zero at the kinematic limits of ±1, was used for the x_F distribution:

$$P(x_F) = \sqrt{\frac{2}{\pi}} \exp(-\frac{1}{2}z^2) \frac{dz}{dx_F},$$

where

$$z = \frac{1}{\sigma_{x_F}}[\ln(\frac{x_F+1}{1-x_F}) - \ln(\frac{x_{F0}+1}{1-x_{F0}})]$$

When normalized to unity between x_{Fmin} and 1, this distribution becomes

$$P(x_F|x_{F0},\sigma_{x_F}) = 2\sqrt{\frac{2}{\pi}} \exp(-\frac{1}{2}z^2) \cdot [\sigma_{x_F}(1-\text{erf}(z_{min}))(x_F+1)(1-x_F))]^{-1}$$

A Gaussian, normalized to unity between 0 and ∞, was chosen for the $p_T{}^2$ distribution:

$$P(p_T{}^2|p_{T0}) = \frac{1}{p_{T0}} \sqrt{\frac{2}{\pi}} \exp(-\frac{1}{2}(\frac{p_T}{p_{T0}})^2).$$

In terms of p_T this becomes:

$$P(p_T|p_{T0}) = 2(\frac{p_T}{p_{T0}}) \sqrt{\frac{2}{\pi}} \exp(-\frac{1}{2}(\frac{p_T}{p_{T0}})^2).$$

The $\cos\theta$ distribution was taken to be

$$P(\cos\theta|\lambda) = \frac{1}{2[1+\lambda/3]} [1+\lambda\cos^2\theta].$$

The ϕ distribution was assumed to be constant, that is,

$$P(\phi) = \frac{1}{2\pi},$$

as was the distribution of the events in the azimuthal angle about the beam direction.

To the extent that these distributions are flexible enough to represent the underlying parent distributions, the likelihood or probability that the ith event will have the kinematic variables

$$X_i = (M_i, x_{Fi}, p_{Ti}, \cos\theta_i, \phi_i),$$

is

$$L(X_i|\Gamma) = P(X_i|\Gamma)A(X_i)[\int P(X|\Gamma)A(X)dX]^{-1},$$

where

$$P(X_i|\Gamma) = P(M_i|\alpha_M) P(x_{Fi}|x_{F0},\sigma_{x_F}) P(p_{Ti}|\sigma_{p_T}) P(\cos\theta_i|\lambda)$$

is the probability that an event will be produced with kinematic variables X_i. The elements of Γ,

$$\Gamma = (\alpha_M, x_{F0}, \sigma_{x_F}, \sigma_{p_T}, \lambda),$$

are the parameters of the kinematic distributions and $A(X_i)$ is the

acceptance of the spectrometer for the event X_i. By definition the acceptance is 1 for an event that has been accepted.

It follows that the likelihood of observing a set of N events $X = (X_0, X_1, \ldots X_N)$ is

$$L(X|\Gamma) = \Pi^N_{i=1}L(X_i|\Gamma).$$

Fitting the N data points to the multidimensional distribution $P(X|\Gamma)$ with the maximum likelihood method involves finding the set of parameters Γ which give the maximum value of the likelihood function, that is, the highest probability that N actual data points would be observed. In practice, because the logarithm of the likelihood is better behaved, the negative logarithm of the likelihood function is minimized, rather than the likelihood itself maximized.

The integral in the denominator of the likelihood function was evaluated using the list of Monte Carlo events. As discussed in the last chapter, the simulation programme had been used to generate muon pairs and follow them through the apparatus. The events were generated randomly throughout phase space according to a multidimensional distribution, $G(X)$, and listed on a disk file. The integral in the denominator of the likelihood function can then be evaluated as

$$\int P(X|\Gamma)A(X)dX = \frac{1}{N} \sum P(X_i|\Gamma)A(X_i)/G(X_i),$$

where

  N is the number of events generated,

  $P(X|\Gamma)$ is the multidimensional distribution being fit to the data points,

  $A(X)$ is the acceptance for an event with kinematic variables X, that is, 1 if the event is accepted and 0 if it is not, and

G(X) is the multidimensional distribution used to generate the Monte Carlo events.

A FORTRAN subroutine was written which evaluated the negative logarithm of the likelihood for a given set of parameters Γ. Positively and negatively charged muon pairs were handled by dividing their likelihood out of the likelihood function. The CERN library routine MINUIT[110][111] was used to search for the minimum of the function. Each time the function was called by MINUIT, the likelihood of each data event was revaluated with the new parameters, and the weights for each Monte Carlo event were recalculated. A full fit of the 387 antiproton continuum events using 10^5 Monte Carlo events took 200 seconds of central processor time on the Fermilab Cyber 175 computer[86].

The parameters obtained from the simultaneous fits of these forms to the unbinned data are given in Table 7 along with the errors and correlation coefficients calculated by MINUIT. The $\cos\theta$ distribution was assumed to behave as

$1+\cos^2\theta$

for these fits. Table 8 gives the results assuming the $\cos\theta$ distribution behaves as

$1+\lambda\cos^2\theta$,

and allowing the fitting program to determine the best value for λ. The resulting value of $\lambda = 1.06 \pm 0.28$ for the pions is in good agreement with the value of $\lambda = 1$ expected from the Drell-Yan model. The agreement obtained for the antiprotons is less satisfactory, but it can be seen that the mass, x_F, and p_T distributions are not sensitive to the value of λ. Both the antiproton and the pion $\cos\theta$ distributions will be discussed further in

Table 7 - Kinematic Distribution Parameters I

This table and the next present the results of fits to the data using different assumptions about the cosθ distribution. The parameter sets in this table assume that the decay distribution behaves as $1+\cos^2\theta$. The acceptance, A, for each of the fits, and the gradient of the acceptance at the minimum of the negative log-likelihood function are also given.

Antiproton I

Parameter	Value	Error	Correlation			Grad(A)
ALPHAM	1.292	0.068				6.326E-3
XFO	0.0	Fixed				
XFSIGMA	0.603	0.019	0.019			1.547E-1
PTO	1.107	0.027	0.013	0.007		-4.066E-3
A	0.217	0.004				

Pion I

Parameter	Value	Error	Correlation			Grad(A)
ALPHAM	1.078	0.037				1.375E-3
XFO	-0.027	0.079	-0.031			2.837E-2
XFSIGMA	1.039	0.074	0.067	-0.928		3.884E-3
PTO	1.155	0.018	0.014	-0.003	0.007	4.190E-3
A	0.229	0.003				

Table 8 - Kinematic Distribution Parameters II

This table presents the results of the fits to the data assuming that the $\cos\theta$ distribution behaves as $1+\lambda\cos^2\theta$, and allowing the fitting programme to find the best value for λ. The acceptance, A, for each of the fits, and the gradient of the acceptance at the minimum of the negative log-likelihood function are also given.

Antiproton II

Parameter	Value	Error	Correlation			Grad(A)
ALPHAM	1.300	0.068				6.074E-3
XFO	0.0	Fixed				
XFSIGMA	0.606	0.019	0.026			1.662E-1
PTO	1.117	0.029	0.032	0.028		-1.193E-2
LAMBDA	0.308	0.363	-0.075	-0.112	-0.227	-4.223E-1
A	0.242	0.022				

Pion II

Parameter	Value	Error	Correlation				Grad(A)
ALPHAM	1.077	0.037					1.494E-3
XFO	-0.028	0.078	-0.016				2.846E-2
XFSIGMA	1.029	0.073	0.059	-0.924			4.177E-3
PTO	1.155	0.018	0.030	0.018	-0.005		4.582E-3
LAMBDA	1.058	0.284	-0.102	-0.127	0.070	-0.163	-2.764E-2
A	0.227	0.011					

the next chapter.

The mass distributions for antiproton and pion produced muon pair events with $x_F > 0$ are shown in Figure 35 and Figure 36 respectively and compared with the exponentials used to calculate the acceptance. In Figure 37 and Figure 38 the x_F distributions for antiproton and pion produced events in the mass range $4 \leq M \leq 9$ GeV/c^2 are shown with the curves used in the acceptance calculations. The p_T, $\cos\theta$, and ϕ distributions are presented and discussed in the next chapter.

The kinematic distributions extracted from the data are in good agreement in all cases with the functional forms assumed. For any variable, the distributions extracted from the data should not be sensitive to the parameterization of that variable. The acceptance correction for the mass plot will depend on the parameterizations chosen for the x_F, p_T, $\cos\theta$, and ϕ distributions, but should not depend on the parameterization chosen for the mass distribution. The agreement between the x_F, p_T, $\cos\theta$ and ϕ dependences extracted and the distributions used to calculate the acceptance leads to confidence in the accuracy of the mass distribution. In the same way the agreement in terms of the other four variables leads to confidence in the x_F distribution, and so on for the other parameters.

Since the acceptance and the kinematic distributions are interrelated, it is necessary to determine the uncertainty in the acceptance due to the uncertainty in the parameters obtained from the likelihood fit. Eadie[107] discusses various methods of estimating error intervals for the parameters from a maximum likelihood fit, but some discussion is necessary here.
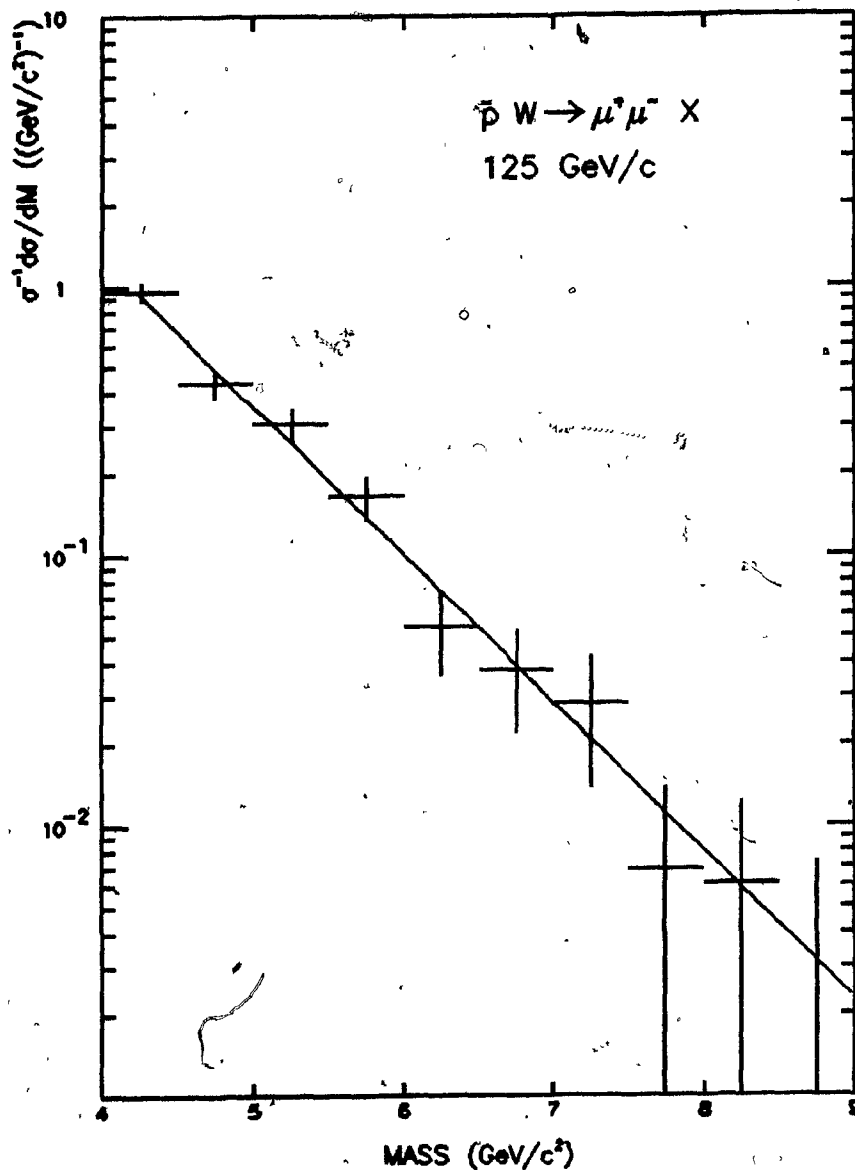
Figure 35 - Antiproton Mass Distribution

The points show the mass distribution of the antiproton produced data. Corrections have been applied for acceptance and reconstruction efficiency. The errors shown are statistical only. The curve shows the exponential fit using the parameter value of $\alpha_M = 1.30$ from Table 7.
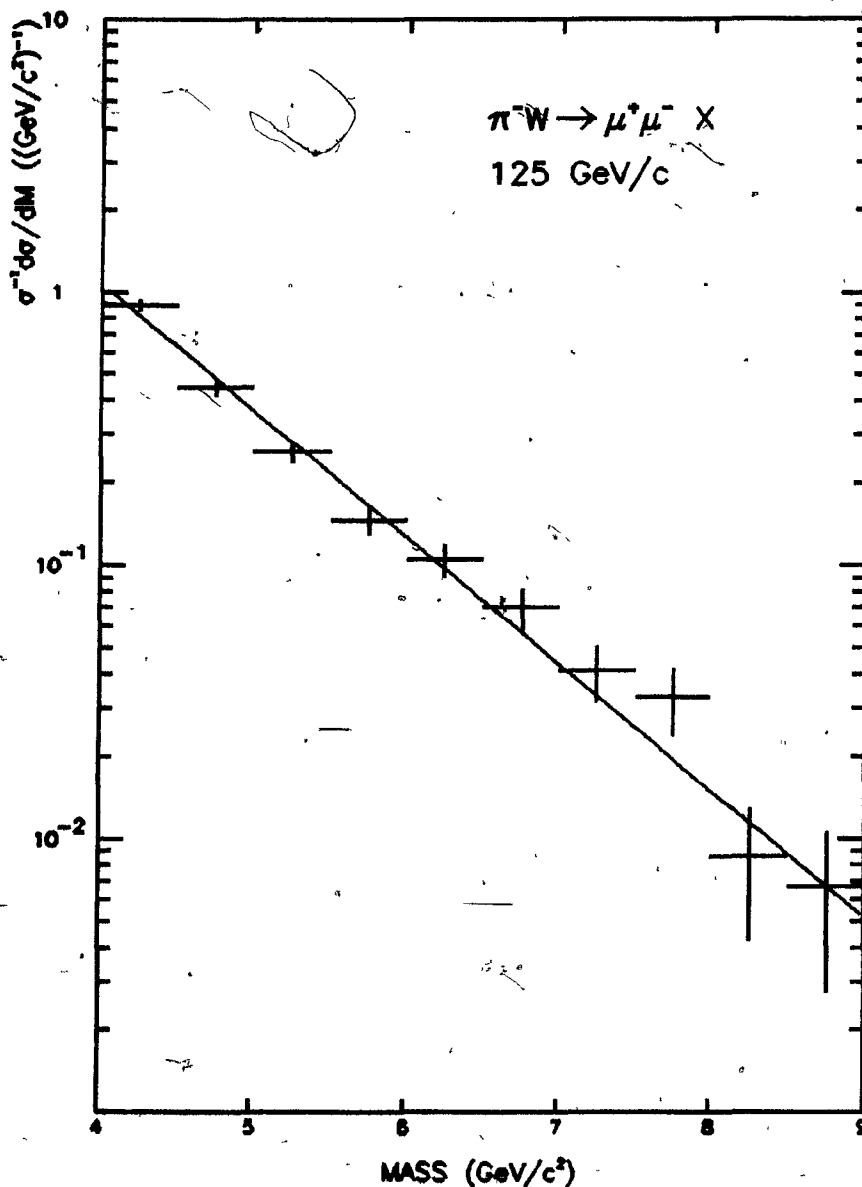
Figure 36 - Pion Mass Distribution

The points show the mass distribution of the pion produced data. Corrections have been applied for acceptance and reconstruction efficiency. The errors shown are statistical only. The curve shows the exponential fit using the parameter value of $\alpha_M = 1.078$ from Table 7.
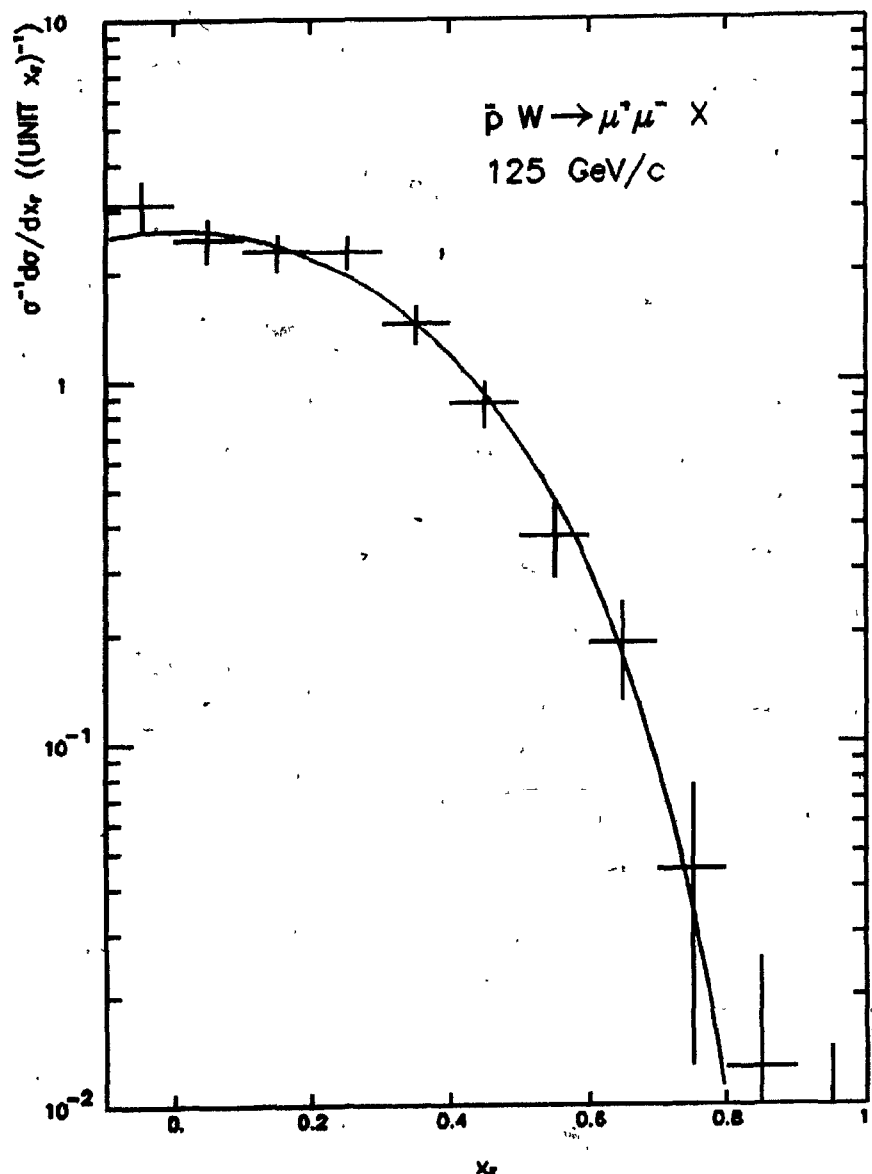
Figure 37 - Antiproton x_F Distribution

The points show the x_F distribution of the antiproton produced data. Corrections have been applied for acceptance and reconstruction efficiency. The errors shown are statistical only. The curve shows the Johnson empirical distribution used to parameterize the data. The parameter values obtained from the fit are given in Table 7.

Figure 38 - Pion x_F Distribution

The points show the x_F distribution of the pion produced data. Corrections have been applied for acceptance and reconstruction efficiency. The errors shown are statistical only. The curve shows the Johnson empirical distribution used to parameterize the data. The parameter values obtained from the fit are given in Table 7.
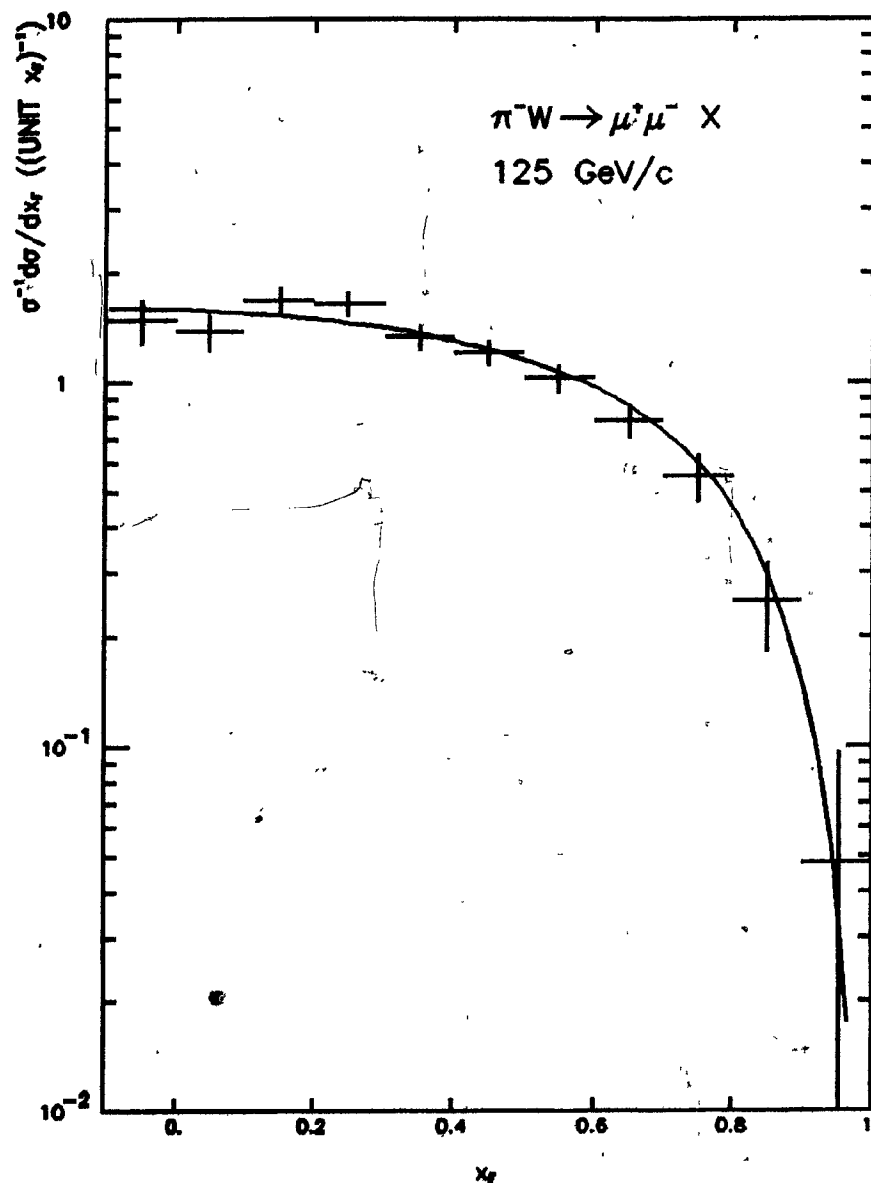
At the minimum, the negative log-likelihood function is roughly parabolic. All the first derivatives vanish and a Taylor series expansion begins with the quadratic terms. A change in the negative log-likelihood of 1/2 corresponds to a change in probability of 68.3 percent, in much the same way as a change in χ^2 of 1 does in the usual least squares fit. If we denote the value of the negative log-likelihood at the minimum by L_0, the locus of points where the negative log-likelihood function has the value

$$-\ln(L) = -\ln(L_0) + \frac{1}{2}$$

defines a hyper-ellipsoidal surface in the multidimensional parameter space, sometimes called the error ellipsoid. This can best be visualised by considering the case of two parameters, α and β, with a minimum in the negative negative log-likelihood function at α_0 and β_0, as illustrated in Figure 39 where the the parameter axes and the error ellipsoid are sketched. Error bounds for a parameter can be evaluated by projecting the ellipsoid onto the parameter axes.

The same technique can be used to calculate bounds on the error in the acceptance. The gradient of the acceptance at the minimum can be used to define an acceptance axis. The error ellipsoid can be projected onto this axis to obtain the values of α and β for which the acceptance is an extremum within the ellipsoid. The acceptance can then be evaluated at these points to obtain bounds on the acceptance. The usual interpretation ascribes a 68.3 percent probability that the acceptance lies within these bounds.

The acceptance of the spectrometer for each of the fits was given in Tables 7 and 8 together with the gradient of the acceptance at the minimum of the negative log-likelihood function, and the calculated bounds for the acceptance. If the $\cos\theta$ distribution is $1+\cos^2\theta$, the probable error made in
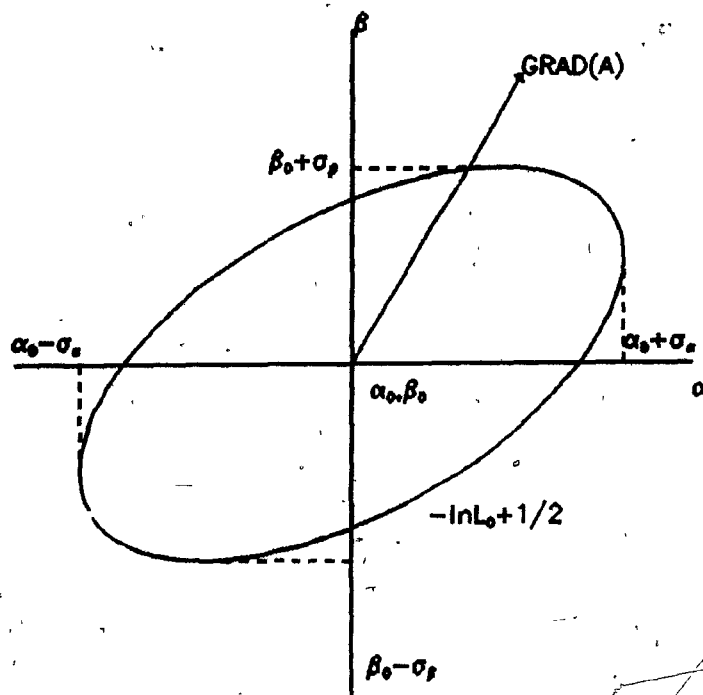
Figure 39 - Error Ellipsoid

The surfaces of constant likelihood oan be used to give error bounds on the parameters by projecting the error ellipsoid onto the parameter axes as discussed in the text. The ellipsoid can also be projected onto the gradient of the acceptance to give bounds for the error in the acceptance calculation as explained in the text.

calculating the acceptance is 2 percent for the antiproton produced data and 1.2 percent for the pion produced data, based on the parameter sets of Table 7. Allowing the fit to determine the value of λ, that is, using the parameter sets of Table 8, the probable error made in calculating the acceptance is 9.1 percent and 5 percent respectively for the antiproton and the pion produced data.

6.2 Reconstruction, Counter, and Trigger Efficiencies

As discussed in the last chapter, the correction for track finding efficiency was included in the calculation of the acceptance by requiring the Monte Carlo events to be reconstructed by the analysis programmes. The uncertainty in the total cross section due to uncertainties in the track finding efficiency correction was calculated to be less than 4 percent. The maximum error in any of the differential cross sections, due to uncertainties in the correction for track finding efficiency, is calculated to be less than 8 percent. The cross section was also corrected for the measured counter and trigger efficiencies.

When the absorber counter was used in the trigger, a subsample of events which did not require the counter was recorded so that the efficiency of the counter could be studied. Reconstructed muon tracks were projected back to the counter and the latch information for these events was examined to see if the counter had been hit in coincidence with the trigger. The overall efficiency was calculated in this way to be

$$\epsilon(ABSR_{1982}) = 0.9700 \pm 0.0012,$$

for the 1982 run, and

$$\epsilon(ABSR_{1981}) = 0.969 \pm 0.004,$$

for the 1981 run.

Events from special runs with the respective hodoscope signals removed from the trigger were used to calculate the CPX and CPY efficiencies. The efficiencies were found to be as follows for the various runs:

$$\epsilon(CPX_{1982}) = 0.9844 \pm 0.0020,$$

$$\epsilon(CPY_{1982}) = 0.9900 \pm 0.0016,$$

$$\epsilon(CPX_{1981}) = 0.9877 \pm 0.0055, \text{ and}$$

$$\epsilon(CPY_{1981}) = 0.9869 \pm 0.0058.$$

The efficiencies of the muon counter arrays were studied in a special run using coincidences between only two out of the three planes in the trigger. The efficiencies of the three muon planes were calculated to be

$$\epsilon(\mu1) = 0.9810 \pm 0.0013,$$

$$\epsilon(\mu2) = 0.9980 \pm 0.0004, \text{ and}$$

$$\epsilon(\mu3) = 0.9970 \pm 0.0005.$$

Combining these numbers yields overall trigger efficiencies for the various runs as follows:

$$\epsilon(TRIG1_{1982}) = 0.905 \pm 0.004 \pm 0.012,$$

$$\epsilon(TRIG2_{1982}) = 0.883 \pm 0.004 \pm 0.013,$$

$$\epsilon(TRIG1_{1981}) = 0.905 \pm 0.011 \pm 0.027, \text{ and}$$

$$\epsilon(TRIG2_{1981}) = 0.877 \pm 0.012 \pm 0.031.$$

The first error quoted for each efficiency is the result of adding the individual errors in quadrature. The second error is the result of assuming

that the individual errors add linearly.

During the data taking, a subsample of events was recorded for which the trigger processor information · was available but not included in the trigger. The trigger processor efficiency was calculated by comparing the state of the trigger processor to the results of a full reconstruction of the event. The trigger processor efficiency was calculated to be

$\varepsilon(TP) = 0.990 \pm 0.010.$

6.3 Resonance Contamination and Reinteraction

The Monte Carlo programme was used to determine the fraction of muon pairs produced in the decay of ψ and ψ' particles which reconstructed to give a mass of $M \geq 4.0$ GeV/c^2. Using the measured value of the ψ cross section, the contamination of the high mass region by pairs from resonace decay was calculated to be 2.4 ± 0.2 percent for both the 1981 and 1982 running periods. A correction was applied to the total cross section to take this contamination into account.

The correction to the total cross section for events produced by secondary interactions in the target was determined by comparing the cross sections for ψ's produced by pions from the different length tungsten targets. If tertiary interactions are ignored and the absorption cross section is assumed to be independent of energy, the measured cross section should depend on the length of the target as

$$\sigma_{Measured} = \sigma_{Direct} + \sigma_{Reinteraction}[1 - \frac{L}{L_{Abs}}/(\exp(\frac{L}{L_{Abs}}) - 1)],$$

where

L is the physical length,

L_{Abs} is the absorption length of the target material,

σ_{Direct} is the cross section that would be measured using an infinitesimally thin target, and

$\sigma_{Reinteraction}$ is a constant that depends on the details of the reinteraction but is independent of the target length.

Measured cross sections for different length targets can therefore be used to obtain these parameters. This equation is discussed further in Appendix III.

The relative production rates for ψ's from the front half of the 1981 tungsten target, the 1982 thick tungsten target, and the 1982 thin tungsten target were found to be 2.728 ± 0.082, 2.715 ± 0.057, and 2.831 ± 0.042 respectively and are plotted in Figure 40. Fitting these values with the above expression gives

$$\sigma_{Direct} = 2.655 \pm 0.078,$$

and

$$\sigma_{Reinteraction} = 0.356 \pm 0.202,$$

so that the correction for any length of target can be determined.

The Monte Carlo programme CASIM[112] was used to extrapolate from pion produced ψ events to the high mass region. CASIM uses the Hagedorn-Ranft thermodynamic model to generate a spectrum of secondary particles. The measured τ dependence of the Drell-Yan cross section[18] was used to generate high mass muon pair events from the spectrum of secondaries. The pairs were propagated through the spectrometer with the simulation program and used to determine the reinteraction rate for the antiproton beam and the high mass region relative to pion produced ψ's. The correction factors for the cross section with various target and beam combinations are given in Table 9.

Table 9 - Reinteraction Correction

These factors have been applied to the various subsets of data to correct for reinteraction. The estimated errors on the corrections are given below the numbers.

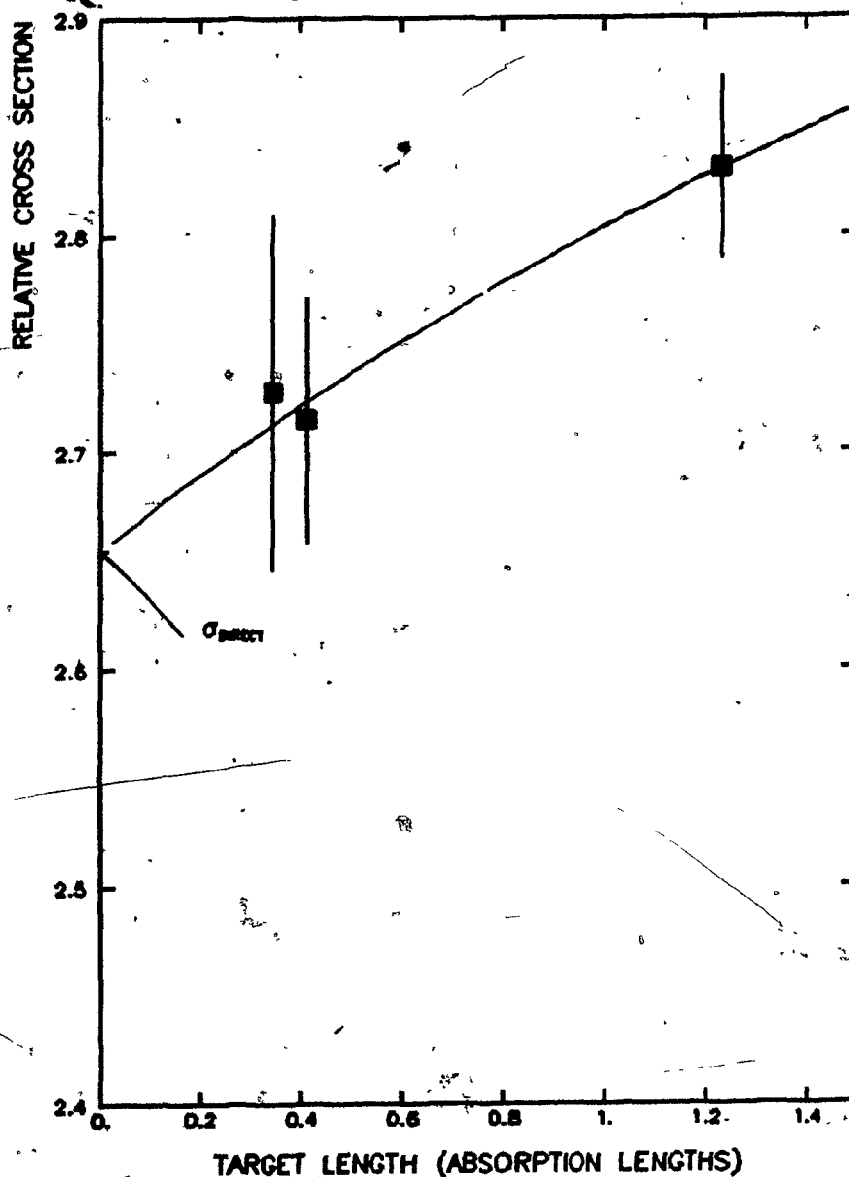|	BE	CU	W	THICK W	THIN W
PSI REINTERACTION CORRECTION					
PBAR	.95440E+00	.95502E+00	.95519E+00	.93899E+00	.97922E+00
	.25233E-01	.24893E-01	.24795E-01	.33760E-01	.11499E-01
PION	.95799E+00	.95442E+00	.95231E+00	.93385E+00	.97832E+00
	.23248E-01	.25223E-01	.26392E-01	.36603E-01	.11996E-01
CONTINUUM REINTERACTION CORRECTION					
PBAR	.96580E+00	.96626E+00	.96640E+00	.95424E+00	.98442E+00
	.18925E-01	.18669E-01	.18596E-01	.25320E-01	.86243E-02
PION	.97479E+00	.97265E+00	.97138E+00	.96031E+00	.98699E+00
	.13949E-01	.15134E-01	.15835E-01	.21962E-01	.71974E-02

Figure 40 - ψ Cross Section vs Target Length

The relative rates for ψ production by pions is shown as a function of target length. The curve shows the parameterization of the cross section as a function of target length discussed in the text. The curve can be extrapolated to a target of infinitesimal thickness to obtain the cross section for direct production of ψ's.

The size of the corrections are less than 5 percent for the high mass antiproton data and less than 4 percent for the pion data. The uncertainties in the corrections lead to a 2 percent uncertainty in the cross sections.

6.4 Beam Flux

The number of beam particles hitting the target was counted directly by the Cerenkov counters and beam hodoscopes. Corrections were made to the flux totals to take into account the probability that two beam particles travelling through the beam telescope at the same time, that is, in the same RF bucket, would not be vetoed by the 2BY≥2 logic. Since no confusion could arise if both particles were pions or if both particles were antiprotons, the flux totals were increased to take these cases into account. Because even a small contamination of pions could bias the antiproton kinematic distributions, all events for which both Cerenkov counters had recorded a beam particle were eliminated from the data sample. The flux totals were correspondingly decreased to take this case into account.

The beam flux totals were taken to be

$$PBAR_{TOTAL} = (PBAR + 2PBAR \cdot VP \cdot HP - (PI \cdot PBAR))(BEAM_{LIVE}/BEAM)$$

for antiprotons, and

$$PI_{TOTAL} = (PI + 2PI \cdot VP \cdot HP - (PI \cdot PBAR))(PI_{PRESCALED}/PI)(BEAM_{LIVE}/BEAM)$$

for pions, where the various terms are defined as follows:

PBAR is the total number of coincidences between a signal in the antiproton Cerenkov counter, CS1, and the BEAM signal, indicating the number of antiprotons which had travelled through the beam telescope;

PI is the total number of coincidences between a signal in the pion Cerenkov counter, CS2, and the BEAM signal, indicating the number of pions which had travelled through the beam telescope;

2PBAR·VP·HP and 2PI·VP·HP are the estimated number of pairs of antiprotons (2PBAR) or pions (2PI) that had travelled through the beam telescope at the same time but were not detected by the 2BY≥2 veto or rejected by the HALO veto logic; the probability that a beam particle would survive the 2BY≥2 veto (VP) or the HALO veto (HP) are discussed below;

(PI·PBAR) is the total number of coincidences between the PI and PBAR signals indicating the number of times that both a pion and antiproton had traversed the beam telescope at the same time;

(BEAM$_{LIVE}$/BEAM) is the live time of the experiment, that is, the fraction of BEAM signals counted while the experiment was not busy reading out a previous event; the live time was calculated on a spill by spill basis and was typically between 80 and 95 percent depending on the running conditions; and

(PI$_{PRESCALED}$/PI) is the fraction of pions that passed the pion prescale logic; this fraction was typically between 1/4 and 1 depending on the setting of the pion prescale unit. This unit was set at the beginning of each run to maintain a reasonable balance between the overall trigger rate and the experimental dead time and depended on the beam spill structure and intensity.

The probability (or formation efficiency, FE) that two beam particles traversing the beam telescope at the same time would give a 2BY≥2 signal was calculated by superimposing beam tracks from the data tapes and determining what fraction of the tracks passed through the same counters in at least two

of the beam stations. The formation efficiency was calculated to be

FE = 0.851

for the 2 out of 3 beam station veto condition. The probability that two beam particles will not be vetoed is then

VP = (1-FE).

The number of times that two beam particles travelled through the beam telescope can be calculated from the number of 2BY≥2 signals counted as

2BEAM = (2BY≥2)/FE.

Poisson statistics were used to determine the number of times two antiprotons (2PBAR) or two pions (2PI) had travelled through the telescope from the number of times two beam particles (2BEAM) had travelled through the beam telescope and from the ratio of the number of antiprotons to pions in the beam.

The probability that a beam particle would not be vetoed by a HALO signal was calculated as

HP = BEAM/[3BY - (2BY≥2)]

where 3BY was the total number of coincidence signals from the three beam stations. HP was typically about 0.96 depending on the running conditions.

The corrections were applied to the beam flux totals on a spill by spill basis. The average corrections to the totals were 0.6 percent for antiprotons and 4 percent for pions. Depending on the intensity, spill structure, and formation efficiency, the correction to the pion total reached 10 percent for some runs. The final flux totals for the various target configurations are given in Table 10. The uncertainty in the cross sections due to uncertainties in the corrections to the beam totals is less than 1.5 percent.

Table 10 - Incident Beam Flux by Target Configuration

This table summarizes the numbers of beam particles hitting the various targets. The number of beam particles of each type hitting the target was counted directly by the Cerenkov counters and beam hodoscopes. All corrections discussed in the text have been applied. The errors in the flux totals are calculated to be less than 1.5 percent for both antiprotons and pions.

Target	Trigger	Antiprotons	Pions
BE	TRIG1	.1578E11	-
	TRIG2	.2453E10	.8354E11
CU	TRIG1	-	-
	TRIG2	.1587E11	.4644E11
W	TRIG1	-	-
	TRIG2	.7792E11	.2014E12
THICK W	TRIG1	.1312E12	.5862E11
	TRIG2	.1026E12	.2646E12
THIN W	TRIG1	.1536E11	-
	TRIG2	-	.7060E11

6.5. Cross Sections

Once the parameters were obtained from the maximum likelihood fit, the data events were binned in terms of the kinematic variables. Like charge muon pairs were subtracted on a bin by bin basis. The acceptance for each bin was calculated using the technique discussed above, and the data points corrected for acceptance. The differential cross section for each bin in the kinematic variable x was then calculated using the formula

$$\frac{d\sigma}{dx} = [A \cdot R \cdot N_{Events}]/[\Delta x \cdot N_o \cdot \rho \cdot L_{Eff} \cdot \xi \cdot E \cdot N_{Beam}]$$

where

x is one of the kinematic variables, M, x_F, p_T, $\cos\theta$ or ϕ,

$\frac{d\sigma}{dx}$ is the differential cross section in cm^2/nucleon assuming an A dependence of A^1,

Δx is the width of the bin,

A is the atomic number of the nuclear target,

N_o is Avagadro's number,

ρ is the density of the target in gm/cm^3,

L_{Eff} is the effective length of the target,

R is the correction for reinteraction and resonance contamination,

ξ is the acceptance for the bin,

E is correction for counter and trigger efficiency,

N_{Events} is the number of data events in the bin, and

N_{Beam} is the number of beam particles hitting the target.

Each of the nuclear targets used was weighed and measured. The length, density, absorption length and effective length of each target are given in Table 2. The absorption length for each target material was interpolated

from absorption cross section data for tungsten, copper and beryllium measured with antiprotons and pions[101] at beam energies of 60 and 200 GeV. The effective length can be expressed in terms of the physical length of the target and the absorption length as

$$L_{Eff} = L_{Abs}[1 - exp(-\frac{L}{L_{Abs}})],$$

where

$L_{Abs} = \sigma_{Abs}\rho N_o A$ is the absorption length of the target material in centimeters,

L is the physical length of the target in centimeters,

σ_{Abs} is the absorption cross section, and

ρ, N_o, and A are the target density in gm/ cm^3, Avagadro's number, and

the atomic number of the target material respectively.

Data from targets of different lengths was combined by taking a weighted average of the effective lengths, using the beam flux as the weighting factor. Uncertainties in the absorption cross section lead to a 1.7 percent uncertainty in the effective length, and thus in the final cross sections.

The final cross sections are presented in the next chapter along with comparisons to the Drell-Yan model and leading order QCD calculations. The statistical uncertainty in the total cross section for antiproton produced muon pairs with masses between 4.0 and 9.0 GeV/c^2 and $x_F \geq 0$ is 5 percent, based on the 387 events collected using the tungsten targets. The statistical uncertainty in the cross section for pion produced pairs is 3 percent based on a sample of 1101 events.

Systematic uncertainties in the acceptance, reinteraction correction, counter efficiencies, and beam totals have been discussed in previous sections of this chapter. These errors and their contributions to the

Table 11 - Systematic Errors

This table gives a summary of the contributions to the systematic error in the measured cross section for antiproton produced muon pairs. Each of the individual component errors has been discussed in the text. If the components are uncorrelated and the errors add in quadrature, the overall systematic error is 5 percent. If the components are completely correlated and the errors add linearly, the overall systematic error is 12 percent.

Source	Error (percent)
Counter and Trigger Efficiency	0.4
Trigger Processor Efficiency	1.0
Reconstruction Efficiency	4.0
Resonance Contamination Correction	0.2
Reinteraction Correction	2.0
Effective Length	1.7
Acceptance	1.2
Beam Normalization	1.5
Total Systematic Error	5.3

uncertainty in the final cross sections are summarized in Table 11. The overall systematic error in the total cross section is 5 percent if the individual components of the error are assumed to be uncorrelated. Alternatively, assuming that the errors are completely correlated gives a bound of 12 percent. These numbers, of course, depend on the assumptions made in calculating them. If the $\cos\theta$ distribution is not $1+\cos^2\theta$, and λ must be determined from the fits, the systematic error is dominated by the resulting uncertainty in the acceptance that the uncertainty in λ introduces, and the uncorrelated systematic errors must be increased to 8 and 11 percent respectively for the antiproton and the pion produced data.

CHAPTER 7

Results

Previous chapters have outlined the reconstruction of the kinematic variables of the muon pairs and the methods used to extract the cross sections. This chapter summarizes the results. The total cross sections for $4 \leq M \leq 9$ GeV/c^2 are compared to the Drell-Yan model and a leading order QCD calculation. The kinematic distributions are presented and compared to other experiments and the Drell-Yan model. In the final section the Drell-Yan model is inverted to extract the valence structure functions of the antiproton and the pion from the data.

7.1 Total Cross Sections

The total cross section per nucleon for continuum muon pair production with $4 \leq M \leq 9$ GeV/c^2 and $x_F \geq 0$ is

$$\frac{\sigma}{p} = 0.104 \pm 0.005 \pm 0.005 \text{ nb}$$

for antiprotons and

$$\sigma_{\pi^-} = 0.107 \pm 0.003 \pm 0.005 \text{ nb}$$

for pions. The first error quoted is statistical and the second error is systematic. The total cross sections were obtained by dividing the number of data events in the appropriate M and x_F ranges by the acceptance calculated using the Monte Carlo simulation and normalizing to the number of beam particles incident on the target, as discussed in the last chapter. The systematic error includes uncertainties in the corrections for counter and reconstruction efficiencies, reinteraction, contamination from the resonance region, and the uncertainty in the acceptance, and assumes that these are uncorrelated.

The calculated value of the cross section in the Drell-Yan model using structure functions from a leading order QCD analysis of deep inelastic muon and neutrino scattering data by Duke and Owens[113] is a factor of

$$K_{\bar{p}^-} = 2.45$$

times smaller than the experimental result. Including leading order QCD corrections[29] and using the same structure functions gives a result

$$\sigma_{Experimental}/\sigma_{LO} = 1.41$$

times smaller than the experimental result. The leading order corrections are only weak functions of mass and x_F. Table 12 gives the ratio of the muon pair cross section calculated using first order QCD to the cross section calculated using the Drell-Yan model for $4 \leq M \leq 9$ GeV/c^2 and $x_F \geq 0$. At low values of x_F, the region that dominates the cross section, this ratio changes by less than 10 percent between masses of 4 and 9 GeV/c^2. The change as a function of x_F for any fixed value of mass is less than 5 percent, and the largest change, at high values of x_F between masses of 4 and 9 GeV/c^2 is only 20 percent.

Table 12 - Leading Order Corrections

This table presents the ratio of the cross section for muon pair production in antiproton-tungsten collisions calcuated using first order QCD to the cross section calculated using the parton model as a function of mass and x_F. The table was calculated using a programme written by R.Wagner using equations from Appendix D of Reference 29, and Set 1 structure functions from Reference 113, with a Λ of 200 MeV/c^2. The programme used a 6 point Gaussian integration routine[114] from the CERN Program Library to calculate the integrals numerically. Doubling the number of integration steps changed the K factor by less than 0.2 percent at any value of mass and x_F in this table.

M \ XF	0.0	0.1	0.2	0.3	0.4	0.5	0.6	0.7	0.8	0.9
4.0	1.725	1.727	1.727	1.726	1.722	1.716	1.707	1.695	1.679	1.654
4.5	1.734	1.735	1.736	1.735	1.733	1.729	1.722	1.714	1.703	1.687
5.0	1.744	1.746	1.747	1.747	1.746	1.743	1.740	1.735	1.728	1.720
5.5	1.757	1.759	1.760	1.760	1.760	1.759	1.758	1.756	1.754	1.754
6.0	1.771	1.773	1.774	1.775	1.776	1.777	1.777	1.778	1.781	1.788
6.5	1.787	1.789	1.791	1.792	1.794	1.796	1.798	1.802	1.808	1.822
7.0	1.805	1.807	1.809	1.811	1.813	1.816	1.820	1.826	1.836	1.857
7.5	1.825	1.827	1.829	1.831	1.834	1.839	1.844	1.852	1.866	1.893
8.0	1.847	1.849	1.851	1.854	1.858	1.863	1.870	1.881	1.897	1.930
8.5	1.872	1.874	1.876	1.879	1.884	1.890	1.899	1.911	1.931	1.970
9.0	1.899	1.901	1.903	1.907	1.912	1.920	1.930	1.945	1.968	2.013

Systematic uncertainties in the antiproton K factor arise from both the theoretical calculation and the experimental measurement. The experimentally measured cross section has an associated statistical uncertainty of 5 percent and a systematic uncertainty of the same magnitude due to errors in the acceptance, counter efficiencies and beam normalization.

It is difficult to make a reliable estimate of the systematic errors associated with the calculated cross section. A ten percent uncertainty in the normalization of the structure functions will lead to a 20 percent uncertainty in the predicted Drell-Yan cross section. The normalization of the deep inelastic structure function, F_2, seems to vary from experiment to experiment by up to 20 percent. Duke and Owens normalized their structure function fits to EMC muon-hydrogen data[115]. Based on their discussions[113] and comparisons by experimental groups[116][117], the normalizations of CDHS neutrino-iron[118], EMC muon-deuterium[119], EMC muon-iron[120], BFP muon-iron[116], CCFRR neutrino-iron[117] and SLAC electron-hydrogen and electron-deuterium[121] scattering data with respect to EMC muon-hydrogen data are 1.1, 1.05, 1.03, 0.98, 0.94, and 0.92 respectively, so that there is a substantial uncertainty in the calculated cross section from this source alone.

Additional uncertainties arise from other sources as well. Some of the difficulties associated with the extraction of structure functions from the data are discussed by Devoto[122] and by Barker, Martin, and Shaw[123]. In both moment analyses and numerical integrations of the Altarelli-Parisi equations, scaling violations depend strongly on the behaviour of the structure functions in the high x region. This is a region which is

difficult to probe experimentally, so that the results of the fits can be sensitive to the functional form assumed.

Problems also arise in the extraction of the non-valence terms which are coupled to an unknown gluon distribution[122][123]. The value of the QCD mass scale parameter, Λ, obtained from the fits depends strongly on the assumptions made about the gluon distribution[113]. Duke and Owens[113] obtained a value for Λ of 0.2 in the fits discussed above using a relatively soft gluon distribution. Assuming a harder gluon distribution changed the value obtained for Λ to 0.4. With structure functions from the fit which assumed a hard gluon distribution, the Drell-Yan contribution to the muon pair cross section changed by only one percent, and only very small changes in the mass and x_F dependence of the cross sections resulted. First order correction terms, however, are directly proportional to

$$\alpha_s = 12\pi/[25 \ln(Q^2/\Lambda^2)]$$

so that, while the dependence of the correction terms on mass and x_F does not change, the correction terms are a factor of

$$\ln(25/0.2^2)/\ln(25/0.4^2) = 1.27$$

higher at $Q^2 = 25$ GeV^2/c^4 if the larger value of Λ is used.

7.2 Kinematic Distributions

The antiproton produced mass distribution is compared to the predictions of the Drell-Yan model in Figure 41. The component contributions to the mass distribution are shown separately. The Drell-Yan predictions were calculated using the deep inelastic structure functions[113] discussed previously, and were multiplied by a factor of
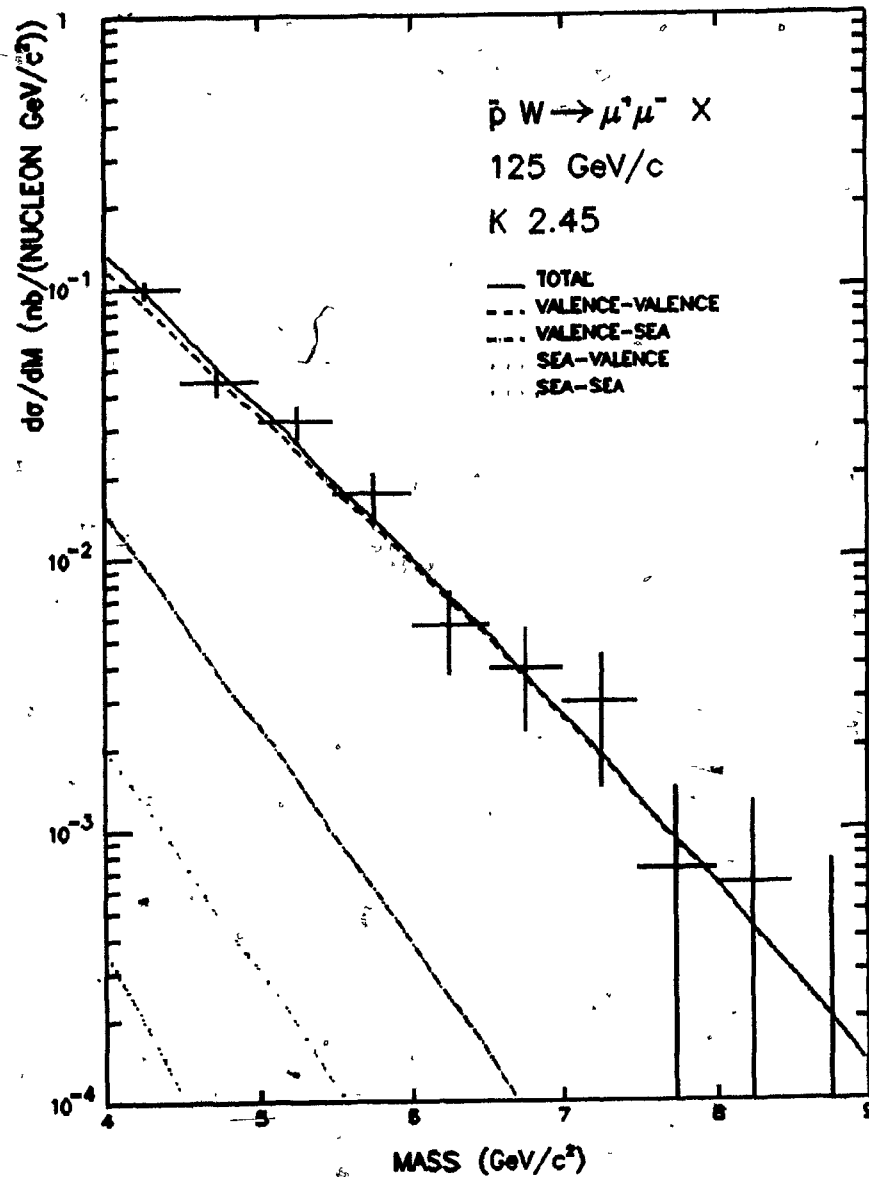
$$K_{\bar{p}} = 2.45$$

Figure 41 - Antiproton Mass Distribution Compared To Drell-Yan Prediction

The points show the mass distribution of the antiproton produced data. The solid line shows the shape of the cross section predicted by the Drell-Yan model using structure functions from measurments of deep-inelastic scattering for both the antiproton and the nucleon. The curve has been multiplied by a factor of 2.45 to reproduce the measured total cross section for $4.0 \leq M \leq 9.0$ GeV/c^2 with $x_F \geq 0$. The other curves show the components of the predicted cross section as indicated. Note that the annihilation of valence antiquarks from the antiproton with valence quarks from the nucleon accounts for more that 90 percent of the total.

to reproduce the measured total cross section. The antiproton cross section
is dominated over the entire mass region by the valence-valence terms.

The pion produced mass spectrum is compared to the Drell-Yan model in
Figure 42. For this plot, the beam structure function was extracted from
our data as discussed later in this chapter, while the nucleon structure
function was taken from the deep inelastic scattering results[113]. The
curves were multiplied by a factor of

$$K_{\pi^-} = 2.39$$

so as to reproduce the measured cross section. Again the component
distributions are shown separately.

In Figure 43 and Figure 44 the x_F distributions are shown together with
the Drell-Yan predictions. Again the calculations have been multiplied by
the empirical K factors necessary to reproduce the experimentally measured
cross sections. As with the mass distributions the separation of the
predictions into the component curves shows the extent to which both the
antiproton and pion processes are dominated by valence-valence annihilation.
Counting rule arguments[124][125] suggest that the x_F distribution for pions
should be flatter than that for antiproton events, and this is confirmed by
the data.

The shapes of the antiproton mass and x_F distributions are sensitive
tests of the Drell-Yan model. Leading order QCD corrections have little
effect other than changing the normalization. The Drell-Yan model describes
both of these distributions very well.

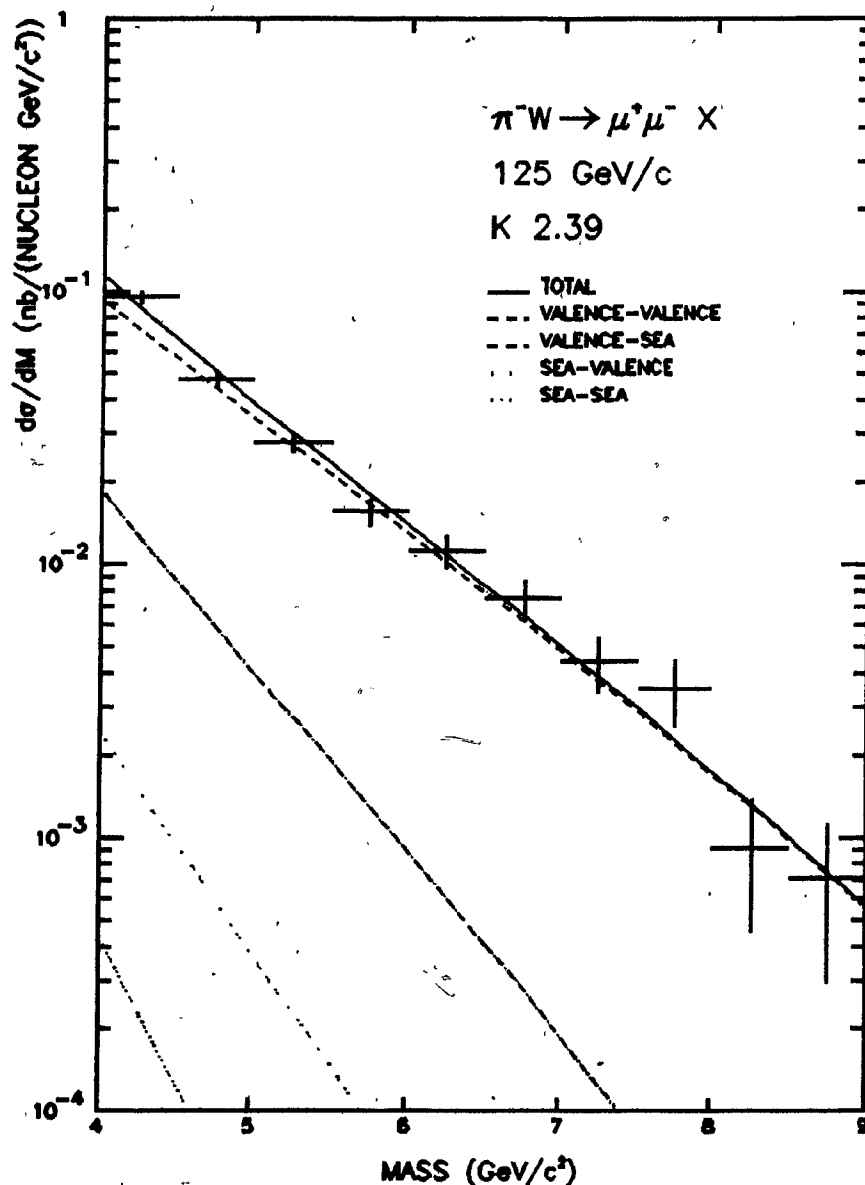The p_T distributions for antiproton and pion produced events with

Figure 42 - Pion Mass Spectrum Compared To Drell-Yan Prediction

The points show the mass distribution of the pion produced data. The solid line shows the shape of the cross section predicted by the Drell-Yan model using structure functions from measurments of deep-inelastic scattering for the nucleon, and our fits for the pion structure function. The curve has been multiplied by a factor of 2.39 to reproduce the measured total cross section for $4.0 \leq M \leq 9.0$ GeV/c^2 with $x_F \geq 0$. The other curves show the components of the predicted cross section as indicated.
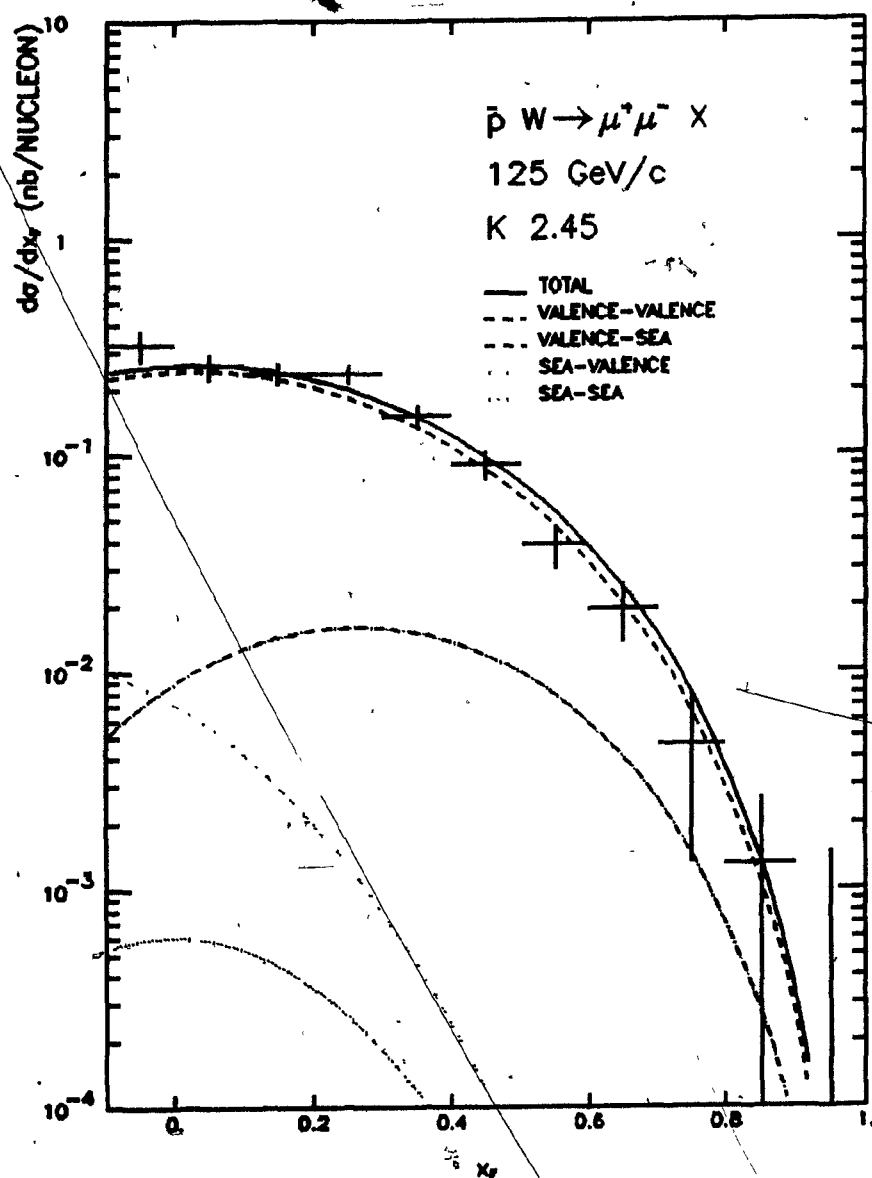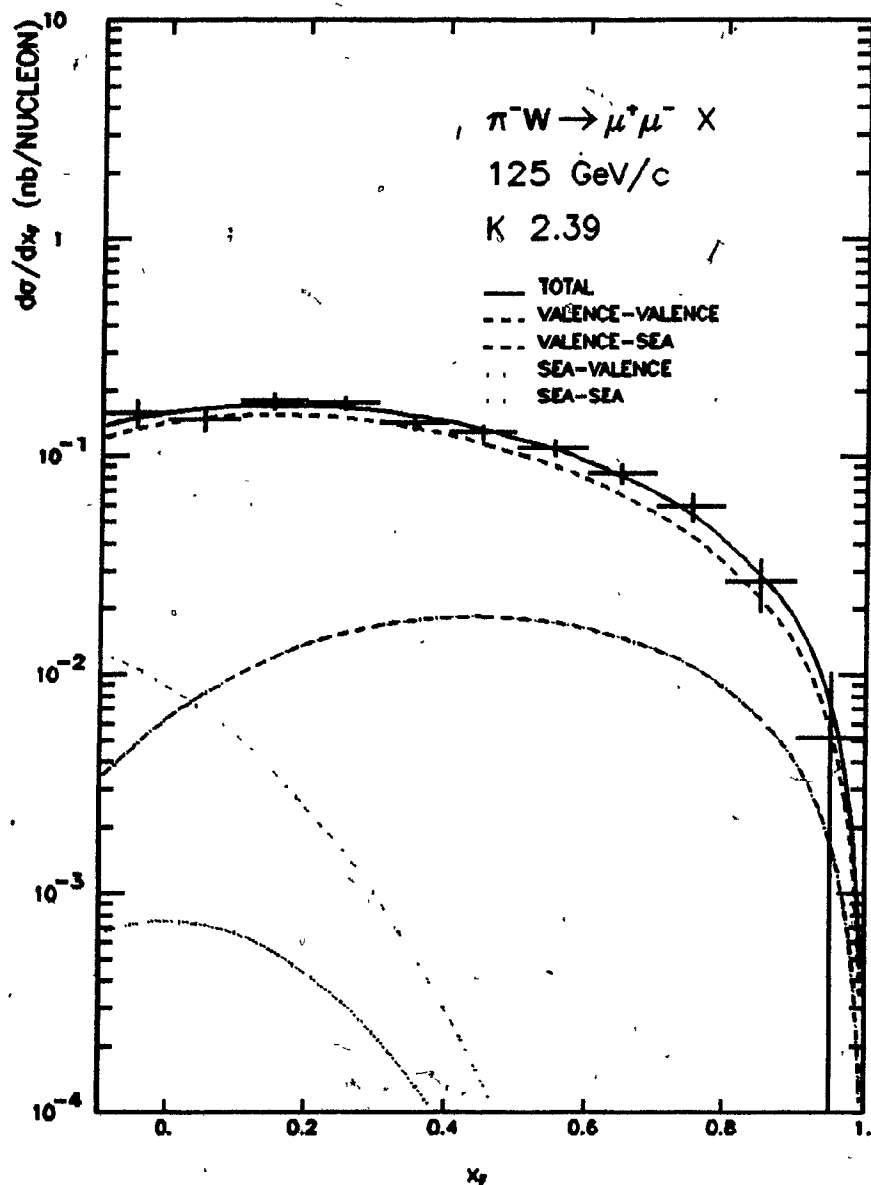
Figure 43 - Antiproton x_F Distribution Compared To Drell-Yan Prediction

The points show the x_F distribution of the antiproton produced data. The solid line shows the shape of the cross section predicted by the Drell-Yan model using structure functions from measurments of deep-inelastic scattering for both the antiproton and the nucleon. The curve has been multiplied by a factor of 2.45 to reproduce the measured total cross section for $4.0 \leq M \leq 9.0$ GeV/c^2 with $x_F \geq 0$. The other curves show the components of the predicted cross section as indicated.

Figure 44 - Pion x_F Distribution Compared To Drell-Yan Prediction

The points show the x_F distribution of the pion produced data. The solid line shows the shape of the cross section predicted by the Drell-Yan model using structure functions from measurments of deep-inelastic scattering for the nucleon, and our fits for the pion structure function. The curve has been multiplied by a factor of 2.39 to reproduce the measured total cross section for $4.0 \leq M \leq 9.0$ GeV/c^2 with $x_F \geq 0$. The other curves show the components of the predicted cross section as indicated.
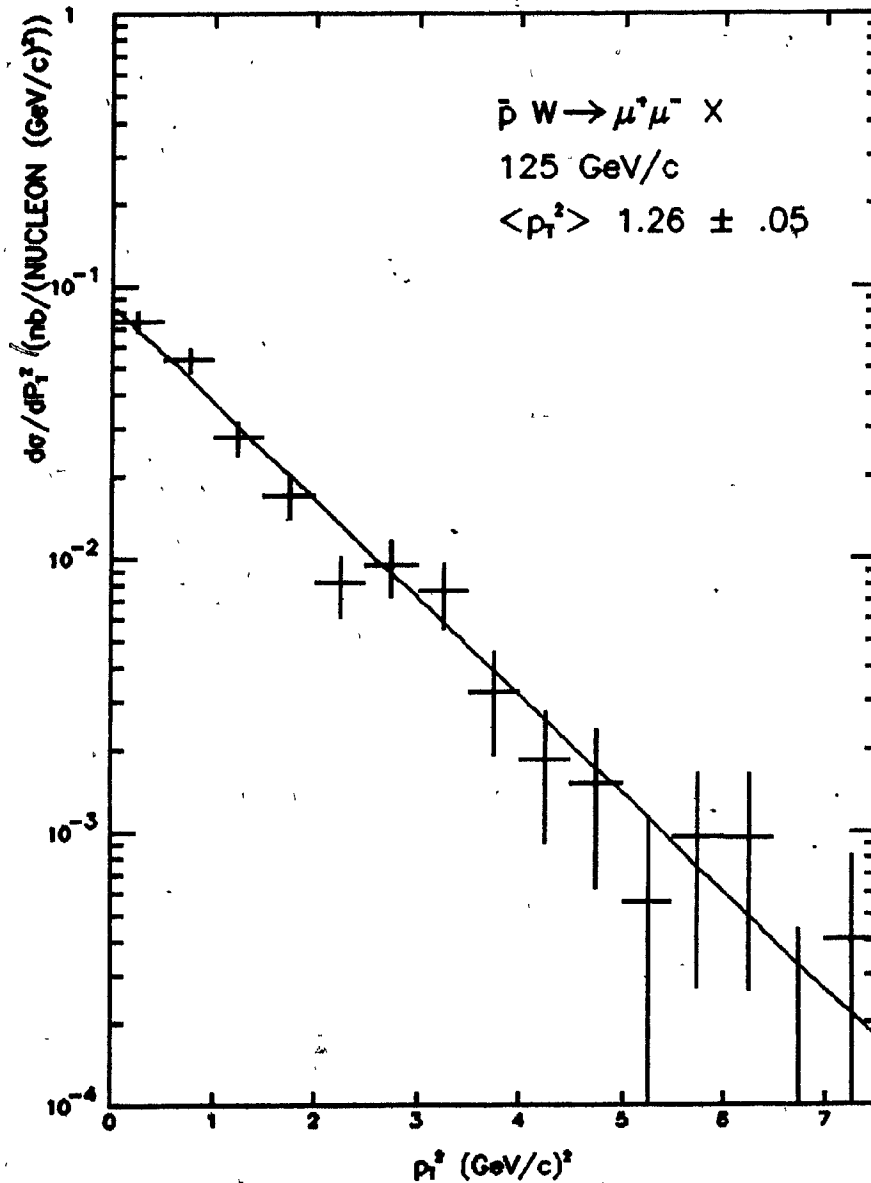
Figure 45 - Antiproton $p_T{}^2$ Distribution

The points show the differential cross section, $d\sigma/dp_T{}^2$, for the production of muon pairs in antiproton-tungsten collisions. The curve shows the Gaussian fit to the data discussed in the last chapter using the parameter value of $p_{T_0}=1.117$ given in Table 7.

$4 \leq M \leq 9$ GeV/c^2 and $x_F \geq 0$ are shown as a function of $p_T{}^2$ in Figure 45 and Figure 46 with the Gaussian distributions used to calculate the acceptance. In both cases the fits are very good, and the parameters of the Gaussians are approximately the same for the two beam particles.

The cosθ distribution for antiproton events with M between 4 and 9 GeV/c^2 and with $x_F \geq 0$ is shown in Figure 47 and the pion cosθ distribution is shown in Figure 48. The curves drawn on the figures are the $1+\cos^2\theta$ distributions assumed to calculate the acceptance. The limited acceptance of the spectrometer at high values of $\cos^2\theta$, and the small data sample make it difficult to determine the value of the λ parameter. The value of λ = 1.06 ± 0.28 obtained from the fit to the pion produced data is consistent with the Drell-Yan model so that we have assumed that λ = 1 for the antiproton produced data as well when fitting the other variables. While the results from fitting with MINUIT discussed in the last chapter suggest that the cosθ distribution may be somewhat flatter than this, the error is large and the data is not inconsistent with the assumed distribution.

The φ distributions are shown in Figure 49 and Figure 50. These distributions were assumed to be uniform in calculating the acceptance for the other variables, as would be expected from the Drell-Yan model. Both the antiproton and the pion data may show a weak dependence on cos 2φ, but this is not statistically significant and will not affect the distributions integrated over this variable.

The good agreement between the data and the parameterizations chosen to describe each of the kinematic distributions leads to confidence in the accuracy of the acceptance calculations for the remaining variables.
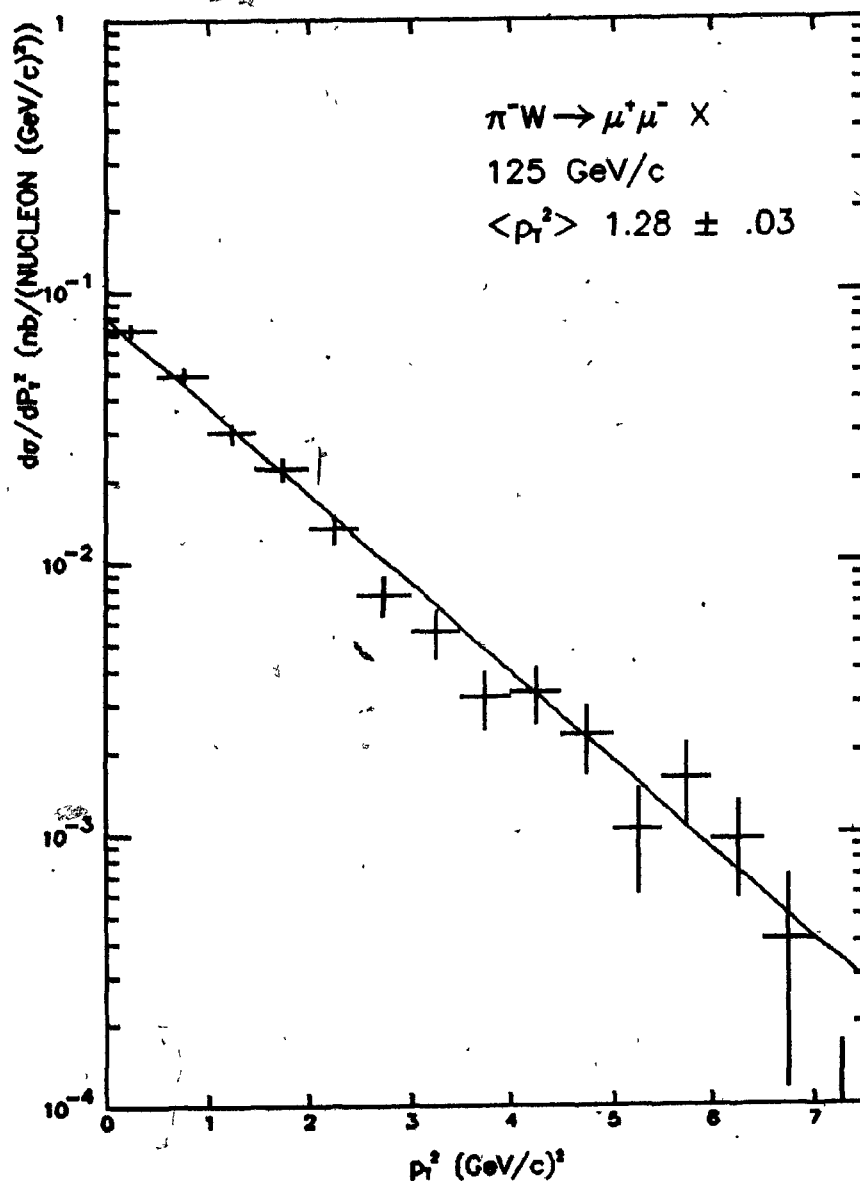
Figure 46 - Pion p_T^2 Distribution

The points show the differential cross section, $d\sigma/dp_T^2$, for the production of muon pairs in pion-tungsten collisions. The curve shows the Gaussian fit to the data discussed in the last chapter using the parameter value of $p_{To} = 1.155$ given in Table 7.
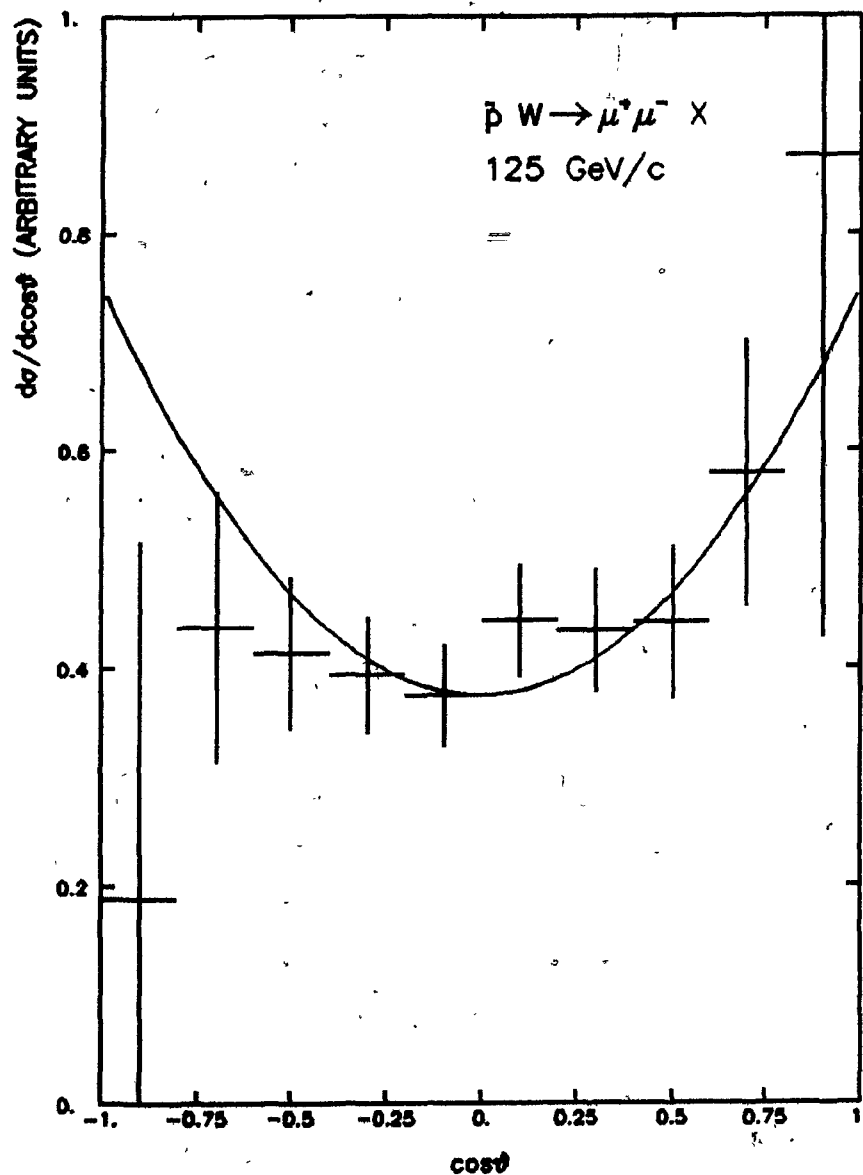
Figure 47 - Antiproton cosθ Distribution In The Gottfreid-Jackson Frame

The points show the distribution, $\sigma^{-1}d\sigma/d\cos\theta$, of muon pairs produced in antiproton-tungsten collisions. The curve shows the $1+\cos^2\theta$ distribution assumed when caluculating the acceptance and discussed in the last chapter.
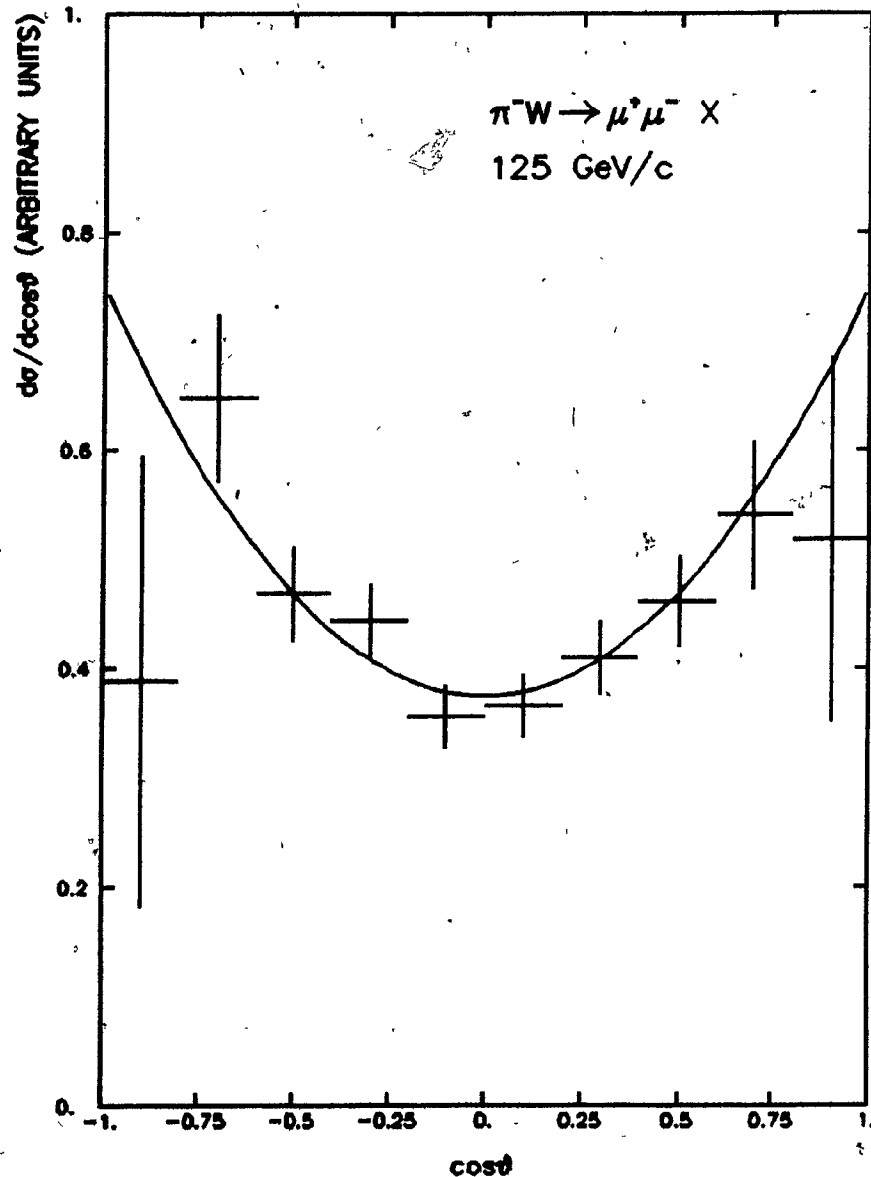
Figure 48 - Pion cosθ Distribution In The Gottfreid-Jackson Frame

The points show the distribution, $\sigma^{-1}d\sigma/d\cos\theta$, of muon pairs produced in pion-tungsten collisions. The curve shows the $1+\cos^2\theta$ distribution assumed when caluculating the acceptance and discussed in the last chapter.
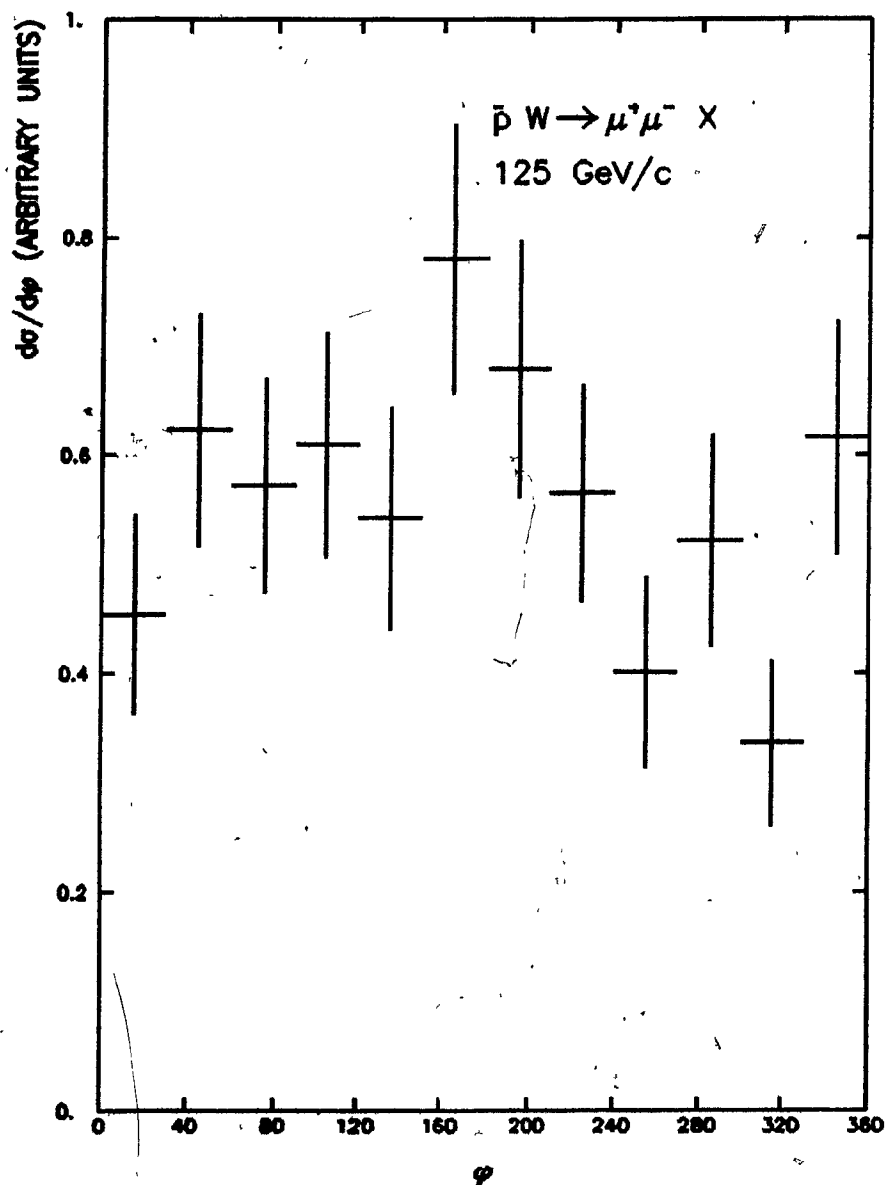
Figure 49 - Antiproton ϕ Distribution In The Gottfreid-Jackson Frame

The points show the distribution, $\sigma^{-1}d\sigma/d\phi$, of muon pairs produced in antiproton-tungsten collisions. This distribution was assumed to be uniform when the acceptance of the spectometer was calculated.
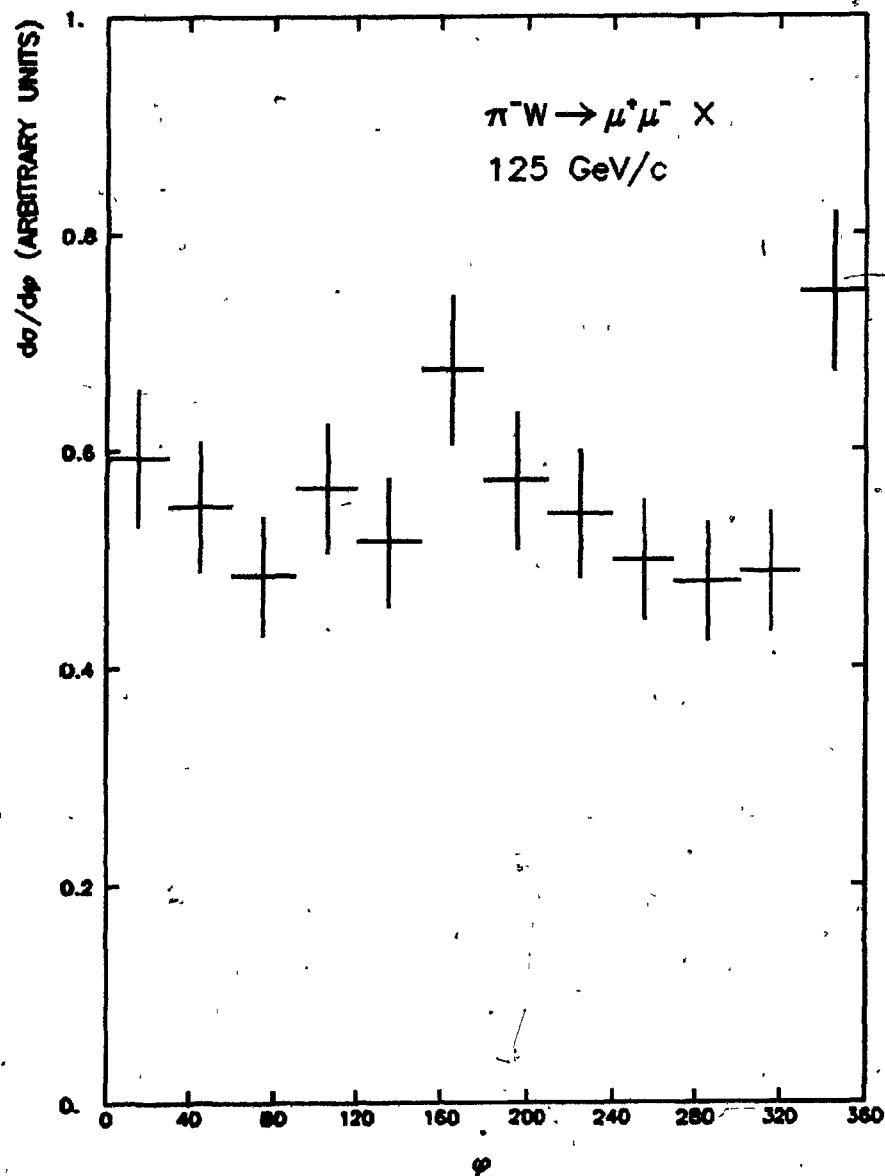
Figure 50 - Pion φ Distribution In The Gottfreid-Jackson Frame

The points show the distribution, $\sigma^{-1}d\sigma/d\phi$, of muon pairs produced in pion-tungsten collisions. This distribution was assumed to be uniform when the acceptance of the spectometer was calculated.

7.3 Comparisons With Other Experiments

Comparison of the data with other experiments is of interest from two points of view. Scaling behaviour of the cross sections provides confirmation of the pointlike nature of the interacting constituents while comparisons with the higher statistics pion data of other experiments provides a valuable cross-check on the antiproton results.

Figure 51 shows the scaling cross section, $M^3 \frac{d\sigma}{dM}$, as a function of $\sqrt{\tau}$ for antiproton produced events with $x_F \geq 0$ compared with similar data using a 150 GeV/c beam obtained by the NA3[126] experiment at CERN. Both the dependence on $\sqrt{\tau}$ and the magnitudes of the two data sets agree very well. Pion produced events are shown in Figure 52, and compared with points from four other experiments[127][128][43][44]. As most fixed target experiments have limited acceptance in the backward hemisphere, the extrapolation of the cross section to all x_F is subject to considerable systematic errors. We have chosen to restrict our results to the region of $x_F \geq 0$, but the same overall trend of the data is evident from the results of all the experiments. Note that we have multiplied the CIP points for this plot by a factor of

$$A_W^{0.12} = 1.87$$

to reflect our assumed A dependence, rather than the $A^{1.12}$ dependence used in their analysis[39].

Perhaps a better test of scaling is the comparison of the cross sections, $s^{3/2} \cdot \frac{d\sigma}{dM}$, for the region with $x_F \geq 0$ as shown in Figure 53. Our pion data is compared with data from the CIP[128] and Omega[43] groups. All of the Omega data and the bulk of the CIP data were taken with a tungsten
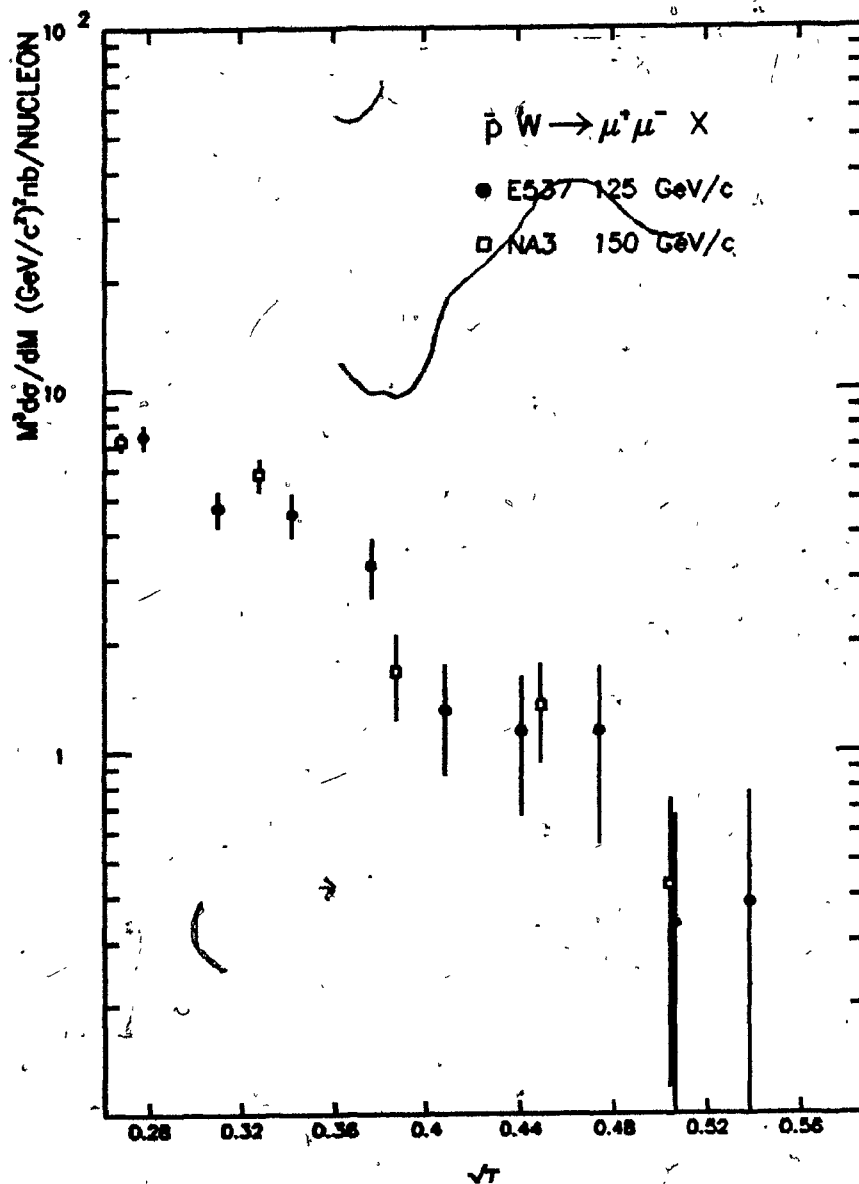
Figure 51 - Antiproton Scaling Cross Section Compared With NA3

Our measurement of the cross section, $M^3 d\sigma/dM$, for the production of muon pairs with $x_F \gtrsim 0$ in antiproton-tungsten collisions is shown together with data obtained by the NA3[10] collaboration using a 150 GeV/c beam incident on a platinum target, as a function of $\sqrt{\tau}$.
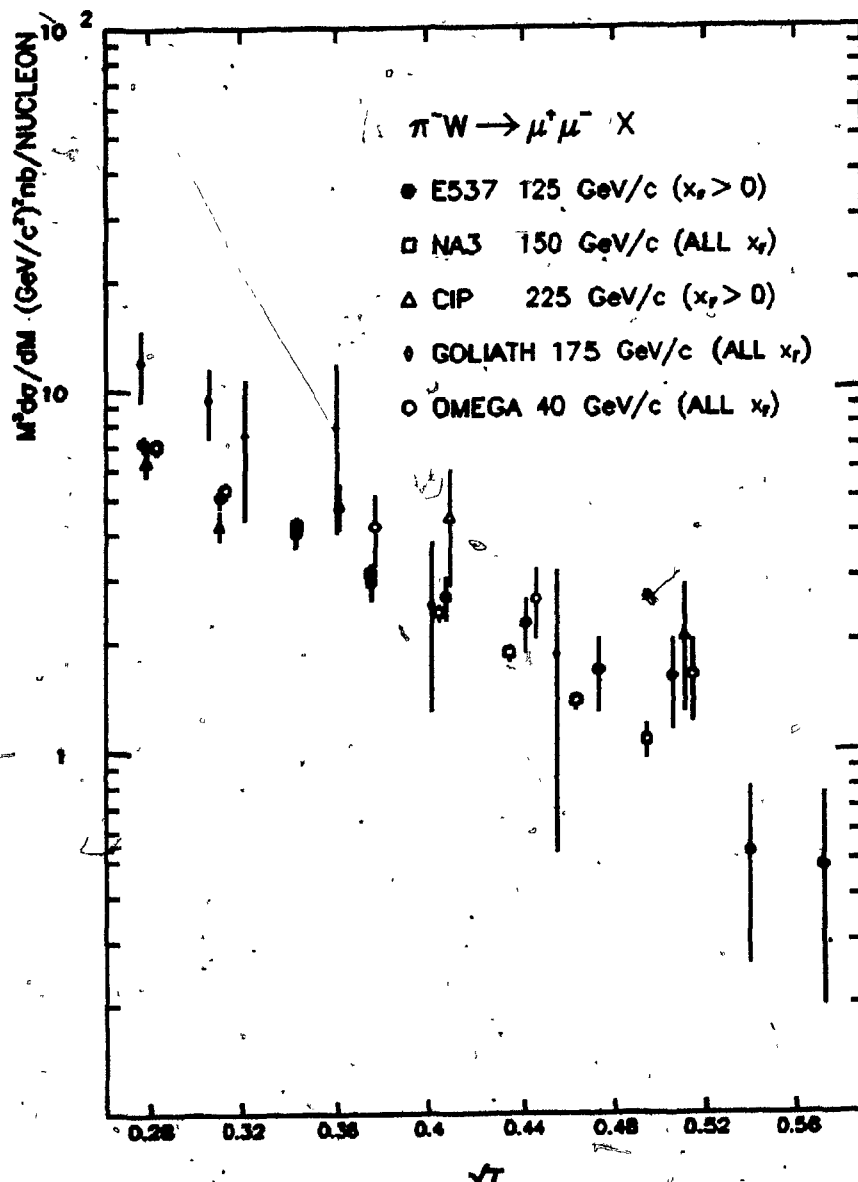
Figure 52 - Pion Scaling Cross Section Comparison

Our measurement of the cross section, $M^3 d\sigma/dM$, for the production of muon pairs in pion-nucleus collisions is shown together with data obtained by the NA3[46], CIP[128], Goliath[44], and Omega[43] collaborations. While we have restricted our measurement to the region with $x_F \geq 0$, the same overall trend is apparent in all the data.
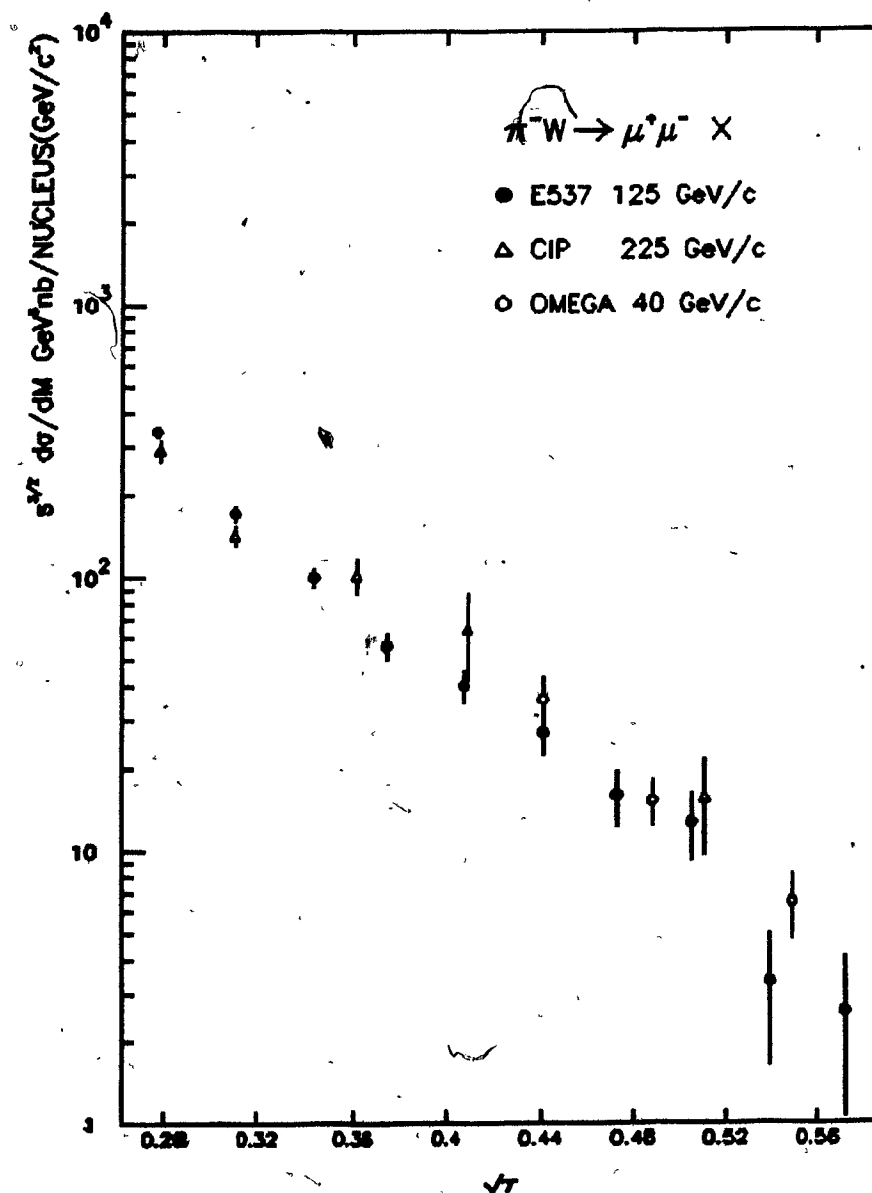
Figure 53 — Pion Mass Cross Section Comparison

Our measurement of the scaling cross section, $s^{3/2} \cdot d\sigma/dM$, with $x_F \geq 0$, for the production of muon pairs in pion-tungsten collisions is shown together with data obtained by the CIP[128] and Omega[43] collaborations as a function of $\sqrt{\tau}$.

target, so that we have presented these cross sections per tungsten nucleus to avoid any controversy about A dependence. There is good agreement over a wide range of incident beam momenta.

According to the Drell-Yan model, the x_F distribution should also exhibit scaling behaviour if it is integrated over the same τ region. Figure 54 shows the good agreement in both shape and magnitude between our measurement of the cross section $s \cdot \frac{d\sigma}{dx_F}$ for masses between 4.10 and 6.71 GeV/c^2 using a 125 GeV/c pion beam incident on a tungsten target and similar data for masses between 5.5 and 9.0 GeV/c^2 as measured by the CIP experiment using a 225 GeV/c beam[128]. Again these cross sections are given per tungsten nucleus.

7.4 Structure Functions

The distributions of the data points in the x_1-x_2 plane are shown in Figure 55 for antiproton produced events and in Figure 56 for pion produced events. Lines of constant M and x_F for a beam momentum of 125 GeV/c are also shown. The kinematic cut at a mass of 4.0 GeV/c^2, which is required to eliminate the resonance region, and our limited acceptance for $x_F \leq 0$ make us insensitive to the behaviour of the beam structure functions below $x_1 \approx 0.2$. The kinematic cut at 4.0 GeV/c^2 is not sharply defined in the x_1-x_2 plane because of the finite momentum bite of the beam and events can appear below the line.

The antiproton and pion structure functions can be extracted from the unbinned data using the fitting procedure outlined in the last chapter. The antiproton valence structure functions were parameterized as
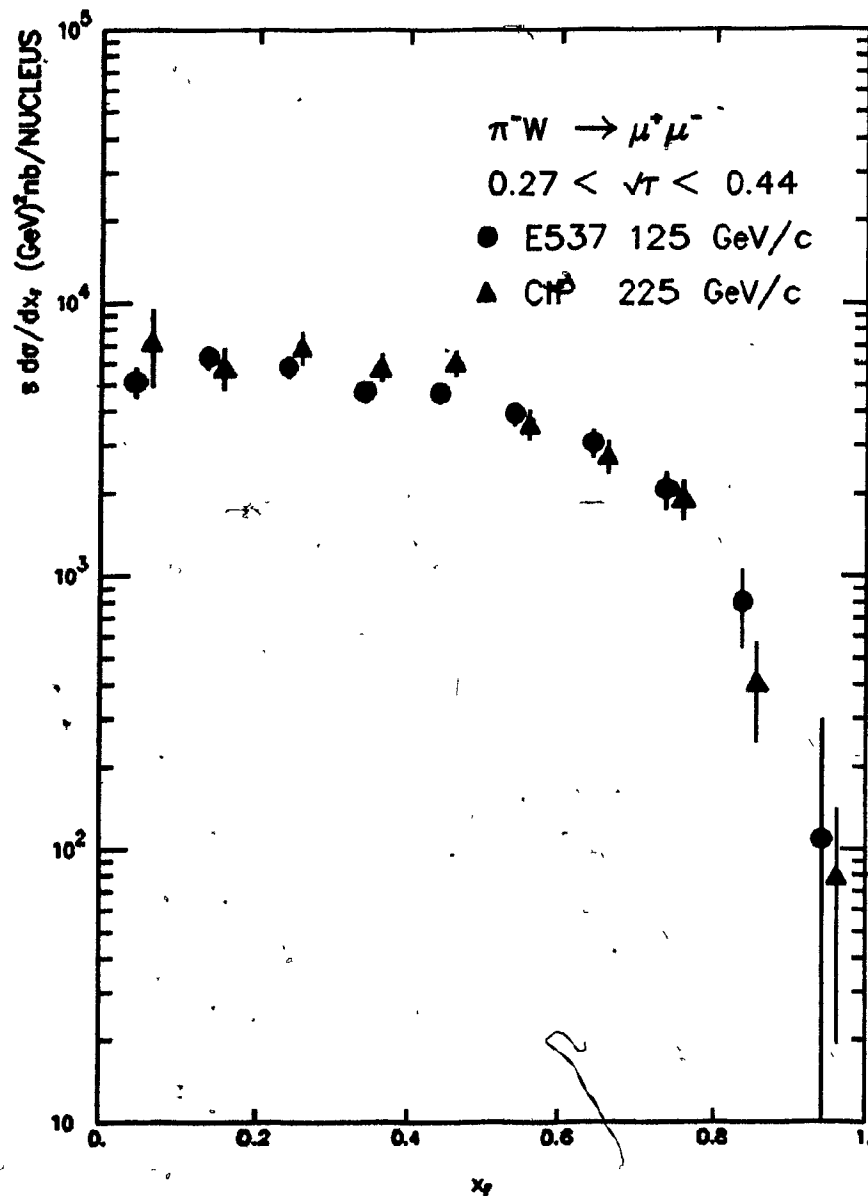
Figure 54 - Pion x_F Distribution Compared With CIP

Our measurement of the cross section, $s \cdot d\sigma/dx_F$, for $4.10 \leq M \leq 6.71$ GeV/c^2 is compared to data obtained by the CIP collaboration[128] in the same region of $\sqrt{\tau}$ for the production of muon pairs in pion-tungsten collisions.
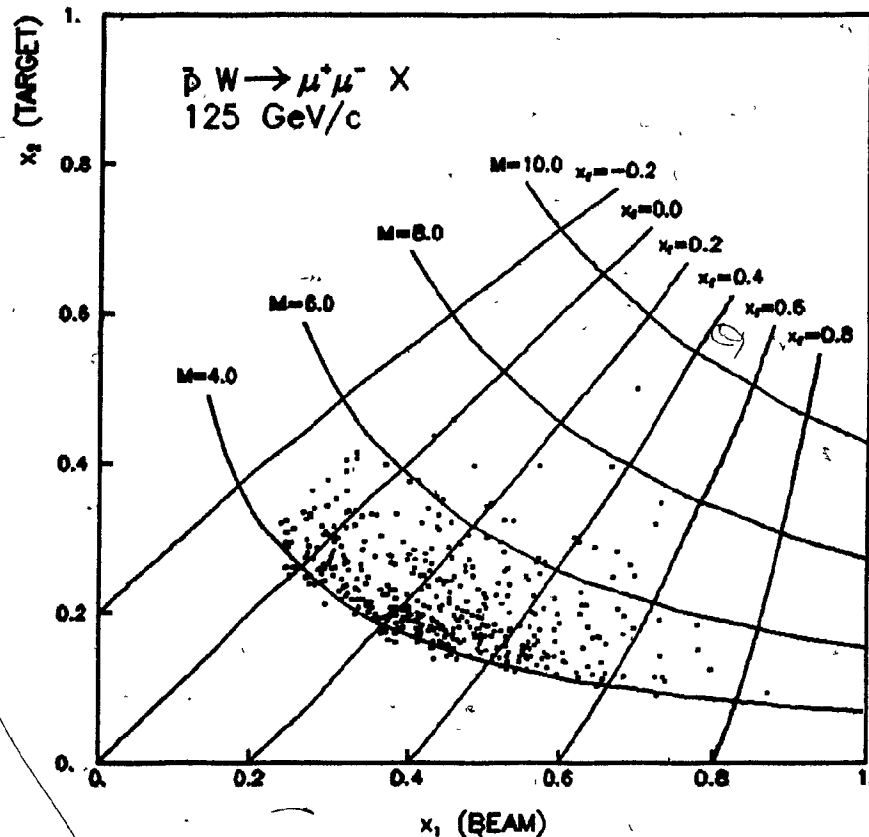
Figure 55 - Distribution of Antiproton Produced Events In The x_1-x_2 Plane

The points show the fractional momenta of the quarks in the beam and target particles, x_1 and x_2, of each of the muon pair events produced by antiprotons. The lines show the contours of constant M and x_F for a beam momentum of 125 GeV/c.

Figure 56 - Distribution of Pion Produced Events In The x_1-x_2 Plane

The points show the values of x_1 and x_2 of each of the muon pair events produced by pions. The lines show the contours of constant M and x_F for a beam momentum of 125 GeV/c.
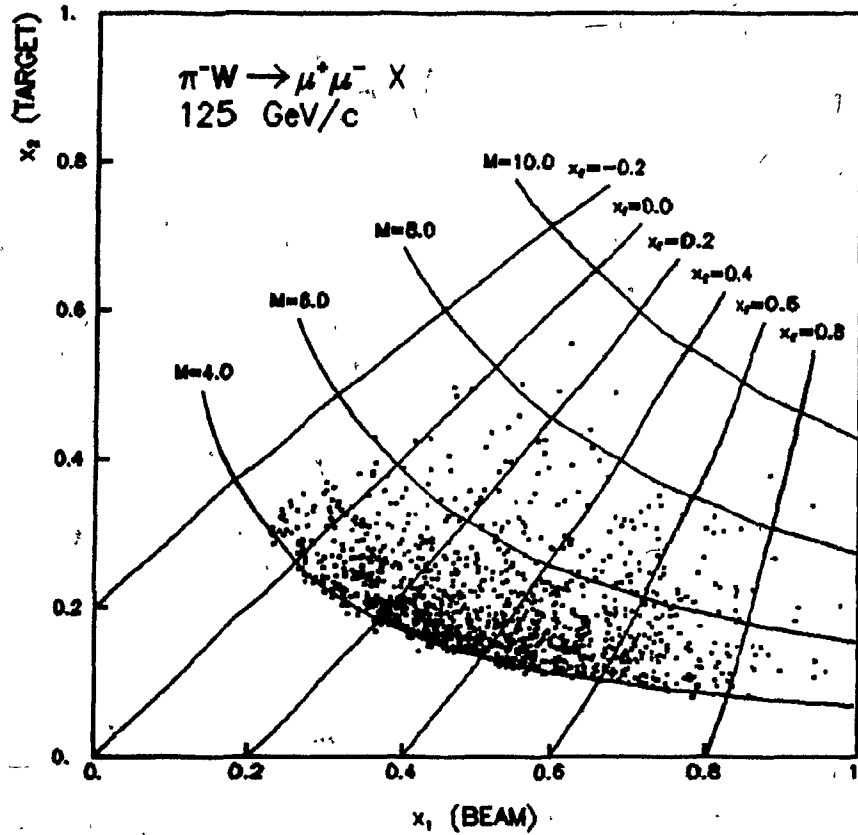
$$\overline{u}_v(x) = Ax^\alpha(1-x)^\beta,$$

and

$$\overline{d}_v(x) = 0.57 \ (1-x) \ \overline{u}_v,$$

with the requirement that

$$\int_0^1 [\overline{u}_v(x) + \overline{d}_v(x)] \frac{dx}{x} = 3.$$

The sea terms used were taken from the analysis by Duke and Owens[113]. With these structure functions, the Drell-Yan model was used to predict the joint M-x_F probability distribution

$$P(M,x_F|\alpha,\beta) = \frac{1}{\sigma} \frac{d^2\sigma}{dMdx_F}.$$

The width of the p_T distribution was allowed to vary freely, while the $\cos\theta$ distribution in the Gottfried-Jackson frame was again assumed to be

$$1+\cos^2\theta.$$

The ϕ distribution was assumed to be uniform. The sea quark structure functions of the antiproton were taken to be the same as the proton sea antiquark structure functions, by particle-antiparticle symmetry. The neutron structure functions were obtained from the proton structure functions by isospin rotation. The results obtained under these conditions are given as Set 2 of Table 13.

When these parameter values are used, the Drell-Yan model requires a K factor of

$$K_{\overline{p}} = 1.91$$

to reproduce the experimental cross section. The kinematic cuts at $M = 4.0$ GeV/c^2 and $x_F = -0.1$ eliminate the region of the x_1-x_2 plane with $x_1 \le 0.2$, making it difficult to determine α reliably; therefore the structure functions were refit with α fixed to 0.5 as expected from Regge theory arguments[129]. The results obtained with this constraint are given as Set 1 of Table 13. The K factor for antiprotons with these assumptions is

Table 13 - Structure Function Parameters

This table presents the results of fitting the antiproton and pion valence structure functions to the mathematical form $x^\alpha(1-x)^\beta$ under various assumptions about the sea and nucleon valence structure functions. The values of α and β obtained from the fits are shown together with the error bounds estimated by MINUIT. The K factor obtained under each of the assumptions is also given.

Antiproton Structure Function Paramters

Set	Alpha	Error	Beta	Error	K
1	0.5	-	3.5155	0.2092	4.63
2	0.7784	0.2207	3.7238	0.2261	1.91
3	0.5	-	3.5232	0.2100	2.45
4	0.8022	0.2703	3.7433	0.2946	2.45
5	0.5	-	3.3799	0.1919	2.45
6	0.9989	0.5602	3.8619	0.5890	2.45
7	0.5	-	3.4143	0.1926	2.45
8	0.9419	0.5594	3.8416	0.5885	2.45

Pion Structure Function Parameters

Set	Alpha	Error	Beta	Error	K
9	0.5	-	1.2609	0.0796	2.39
10	0.3915	0.2011	1.1791	0.1750	2.93

$$K\frac{-}{p} = 4.63,$$

and this illustrates the sensitivity of the cross section to the assumed behaviour of the structure functions at low values of x. Approximately one half the integral,

$$\int_0^1 [\overline{u}_v(x) + \overline{d}_v(x)] \frac{dx}{x} = 3,$$

is contributed by the region $x \leq 0.2$. The normalization of the Drell-Yan cross section in turn depends quadratically on the normalization of the structure functions. The choice of a different functional form to parameterize the structure functions, for example, a sum of terms of the form $x^\alpha(1-x)^\beta$, could drastically alter the normalization of the calculated Drell-Yan cross section while still conserving baryon number by integrating to give three valence quarks.

The relative contribution of the valence quarks is also sensitive to the method used to normalize the structure functions. Using the Drell-Yan calculations with deep inelastic structure functions as a guide, the data was constrained so that the valence quarks contributed a constant fraction of the total cross section given by

$$\sigma_{vv} = 0.91 \ \sigma_{Total}.$$

The results of these fits with α fixed, (Set 3), and α free, (Set 4), are also given in Table 13. It can be seen from the small changes in α and β, that the shape of the structure function is not very sensitive to the normalization convention chosen. In addition, the antiproton structure function was fit using the deep inelastic structure functions for the target particle only. While we did not have sufficient data to allow the beam particle structure functions to violate scaling, we allowed the target particle structure functions to evolve with $Q^2 = M^2$, and the results are given as Sets 5 and 6 in Table 13. Using the deep inelastic structure

functions for the target particle with Q^2 fixed to our mean value of $\langle M^2 \rangle = 25$ $(GeV/c^2)^2$ gives similar results which are Sets 7 and 8 of Table 13.

The pion valence structure function was fit in a similar fashion. The valence structure function was parameterized as

$$V^{\pi}(x) = Ax^{\alpha}(1-x)^{\beta},$$

normalized such that

$$\int_0^1 V^{\pi}(x) \frac{dx}{x} = 1.$$

The NA3[130] result,

$$S^{\pi}(x) = 0.292 (1-x)^{8.2},$$

obtained from a simultaneous analysis of 200 GeV/c π^+ and π^- data, was used for the sea. Results with α fixed at 0.5 and free to vary are given as Sets 9 and 10 respectively in Table 13.

Using the results of Set 9, where α has been fixed at 0.5, in the Drell-Yan model, we find a K factor of

$$K_{\pi^-} = 2.39$$

is needed to reproduce the experimental cross section for the pion produced data with masses between 4.0 and 9.0 GeV/c^2 and $x_F \geq 0$. Using the results of Set 10, where the value of α is determined by the fitting programme, a K factor of

$$K_{\pi^-} = 2.93$$

is required. As for the antiproton, the normalization of the structure function is dominated by its behaviour at low values of x. Using a different functional form to parameterize the structure function results in a different K factor. It is apparent from the results of the fits to both the antiproton and the pion produced data that the sum rules are not a good

guide to the normalization of the structure functions in the absence of information about their behaviour at low values of x. The shape of the structure functions is less sensitive. The results of two of our antiproton structure function fits are shown in Figure 57. The points on this graph are projected from our data as discussed in the next section. The dashed line shows the results of Set 5 of Table 13, where α was fixed to 0.5, while the dot-dashed line shows the results of Set 6. Both of these fits describe the data well over the range of x_1 accessible to our experiment. The dot-blank line and the dotted line show the average deep inelastic valence structure functions with $Q^2 = M^2$ and with $Q^2 = \langle M^2 \rangle = 25 \ (GeV/c^2)^2$, respectively. All of the curves have been multiplied by

$$K\frac{}{p} = 2.45$$

to allow them to be compared to the data points. It is apparent from these curves that the agreement between our structure function fits and the results obtained from deep inelastic scattering is good. The small differences between the two deep inelastic curves justify ignoring the scale breaking behaviour of the beam structure function in the fitting.

Figure 58 shows our fits to the pion valence structure function. Set 9 of Table 13 is shown by the dashed line, and Set 10 is shown as the dot-dashed line. Again the points are the projection of our data on the x_1 axis described in the next section, and the two fits have been multiplied by their respective K factors. Both reproduce the shape of the structure function very well. It is clear that any measurement of the pion K factor is subject to large systematic uncertainties as long as the behaviour of the valence quark structure function is unkown.
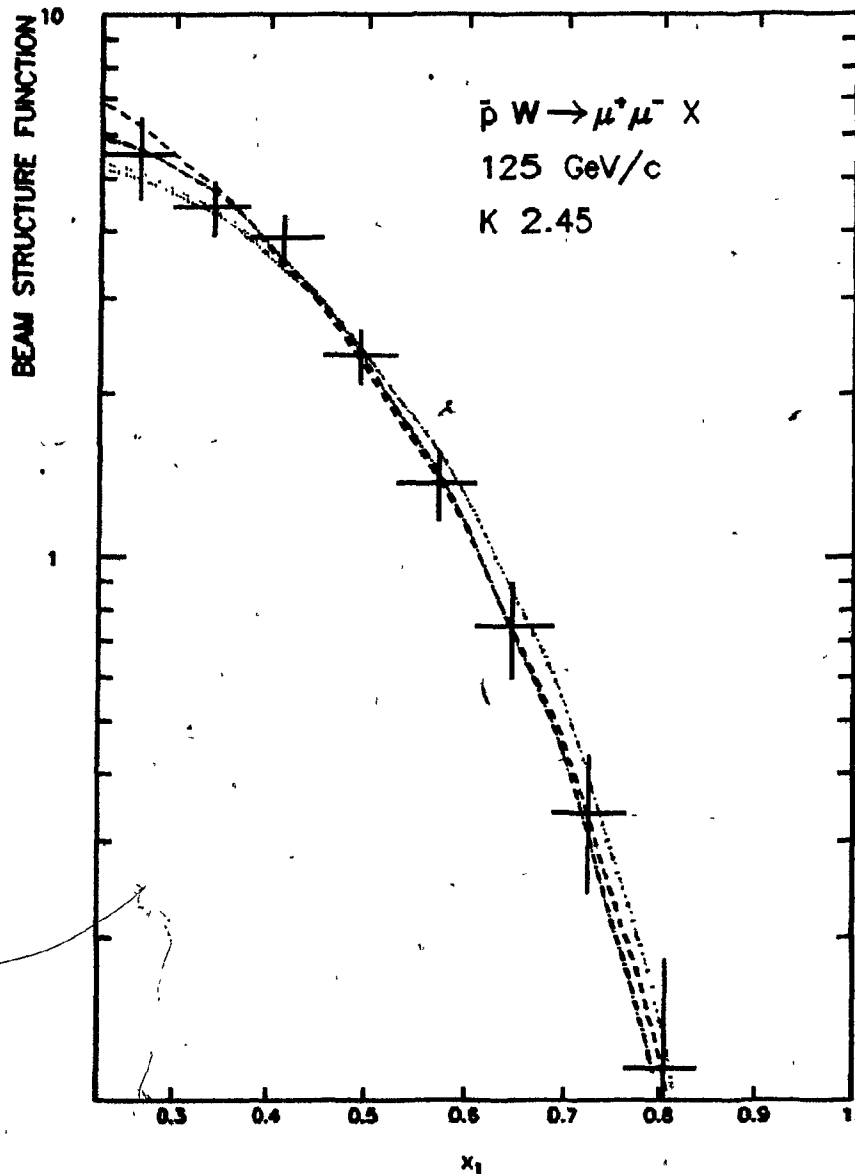
Figure 57 - Antiproton Structure Function Fits

The dot-dashed line shows the antiproton structure function fit, Set 5 of Table 13, with α fixed to 0.5. The dashed line shows the curve corresponding to Set 6. The dot-blank line and the dotted line show the value of the deep inelastic structure functions[113] with $Q^2 = M^2$ and $Q^2 = 25$ $(GeV/c^2)^2$ respectively.
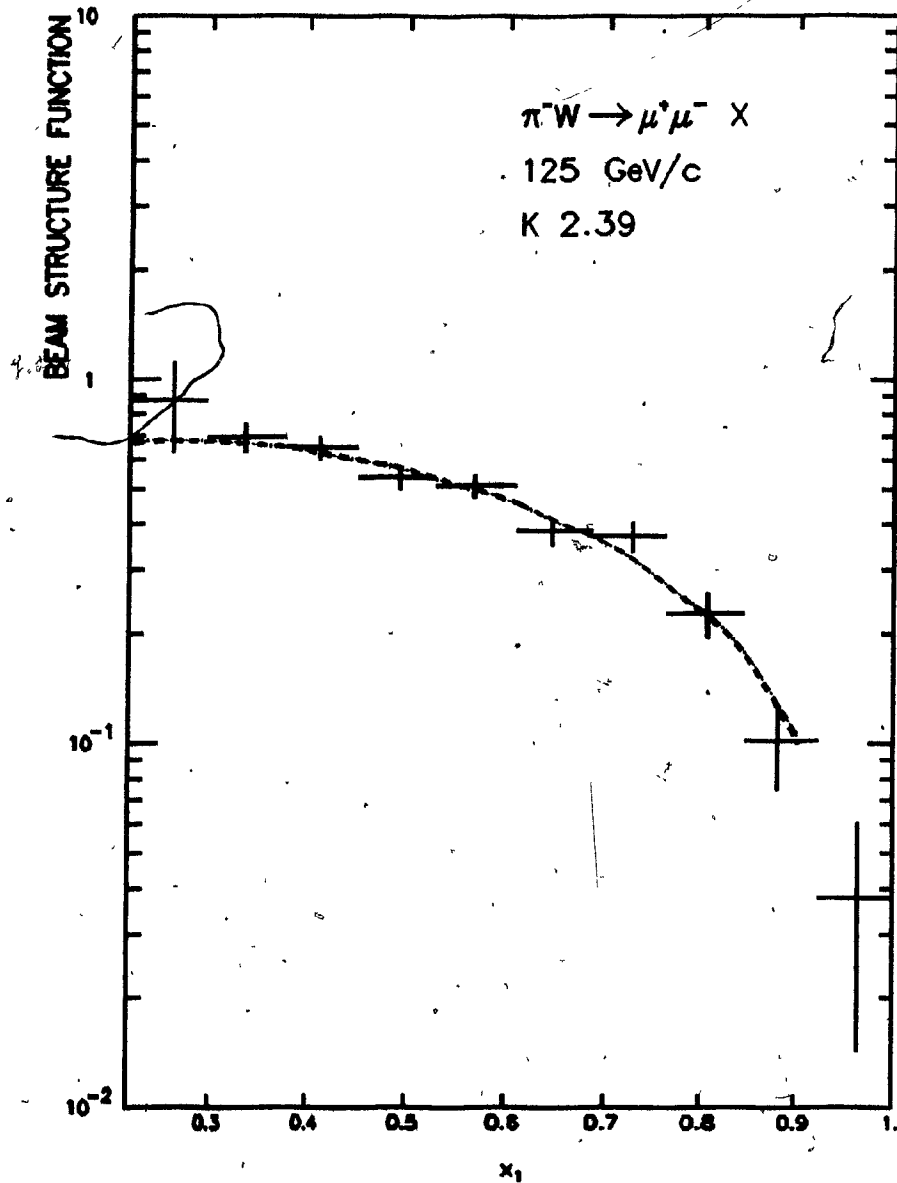
Figure 58 - Pion Structure Function Fits

The dashed line shows the pion valence quark structure function fit using the parameters of Set 9 of Table 13, with α fixed to 0.5. The dot-dashed line shows the curve corresponding to Set 10. Both curves have been multiplied by their respective K factors.

7.5 Structure Function Projections

Because the expressions for the cross sections can be approximated by the product of a function of x_1 and a function of x_2, it is possible to project average beam and target structure functions from the data. These projections can be used to compare the structure function fits obtained above with the data, and to compare the data to other experiments.

The cross section can be written exactly as

$$\frac{d^2\sigma}{dx_1 dx_2} = \frac{\sigma_0}{x_1^2 x_2^2} [F_0(x_1,Q^2) \, G_0(x_2,Q^2) + F_1(x_1,Q^2) \, G_1(x_2,Q^2) + F_2(x_1,Q^2) \, G_2(x_2,Q^2)],$$

where

$F_0(x_1,Q^2)$, $F_1(x_1,Q^2)$ and $F_2(x_1,Q^2)$ are combinations of beam particle quark structure functions,

$G_0(x_2,Q^2)$, $G_1(x_2,Q^2)$ and $G_2(x_2,Q^2)$ are combinations of target particle quark structure functions and

$\sigma_0 = \frac{4\pi\alpha^2}{81s}$ is a normalization factor independent of x_1 and x_2.

For antiproton-tungsten collisions, the structure functions F and G are usually chosen as

$$F_0(x_1) = 4u^P(x_1) + d^P(x_1),$$

$$F_1(x_1) = d^P(x_1),$$

$$F_2(x_1) = S^P(x_1),$$

and

$$G_0(x_2) = \frac{Z}{A}u^P(x_2) + (1-\frac{Z}{A})d^P(x_2) + S^P(x_2),$$

$$G_1(x_2) = (1-2\frac{Z}{A})(u^P(x_2) - d^P(x_2)),$$

$$G_2(x_2) = (1-3\frac{Z}{A})u^P(x_2) + (4-3\frac{Z}{A})d^P(x_2) + 10.5S^P(x_2),$$

where

$u^P(x)$, $d^P(x)$, and $S^P(x)$ are the up quark, down quark and sea quark

structure functions respectively for the proton, and

$\frac{Z}{A}$ is the fraction of protons in the nuclear target.

For pion-tungsten collisions F and G are given by

$$F_0(x_1) = V^\pi(x_1),$$

$$F_1(x_1) = S^\pi(x_1),$$

and

$$G_0(x_2) = 4\frac{Z}{A}u^P(x_2) + 4(1-\frac{Z}{A})d^P(x_2) + 5S^P(x_2);$$

$$G_1(x_2) = (1+3\frac{Z}{A})u^P(x_2) + (4-3\frac{Z}{A})d^P(x_2) + 11S^P(x_2),$$

where $V^\pi(x)$ and $S^\pi(x)$ are the valence and sea structure functions of the

pion and $F_2(x_2)$ and $G_2(x_2)$ are both zero. The terms have been chosen in

such a way that the second and third terms are small compared to the first.

If we ignore them, we can write the cross section as

$$\frac{d^2\sigma}{dx_1dx_2} = \frac{\sigma_0}{x_1^2x_2^2} F_0(x_1,Q^2) G_0(x_2,Q^2).$$

When this is integrated over x_2 we obtain

$$\frac{d\sigma}{dx_1} = \frac{\sigma_0}{x_1^2} \int F_0(x_1,Q^2) G_0(x_2,Q^2) \frac{dx_2}{x_2^2}$$

which we can write as

$$\frac{d\sigma}{dx_1} = \frac{\sigma_0}{x_1^2} \overline{F}_0(x_1) \int G_0(x_2,Q^2) \frac{dx_2}{x_2^2}$$

where we have defined, $\overline{F}_0(x_1)$, a structure function averaged over x_2, and

thus over Q^2, as

$$\overline{F}_0(x_1) = \int F_0(x_1,Q^2)G_0(x_2,Q^2) \frac{dx_2}{x_2^2} \cdot [\int G_0(x_2,Q^2) \frac{dx_2}{x_2^2}]^{-1}.$$

We can therefore project out the averaged beam structure function, $\overline{F}_0(x_1)$,

by histogramming the data in terms of x_1 with a weight given by:

$$w(x_1) = \frac{x_1^2}{\sigma_0} [\int G_0(x_2,Q^2) \frac{dx_2}{x_2^2}]^{-1}.$$

Similarly the averaged target structure function, $\overline{G}_0(x_2)$, can be projected

out by histogramming the events in terms of x_2 with a weight of

$$w(x_2) = \frac{x_2^2}{\sigma_0} [\int F_0(x_1,Q^2) \frac{dx_1}{x_1^2}]^{-1}.$$

When the exact expression for the cross section is used, a structure function projection can still be defined as

$$\overline{F}(x_1) = \frac{x_1^2}{\sigma_0} \frac{d\sigma}{dx_1} \left[\int G_0(x_2) \frac{dx_2}{x_2^2} \right]^{-1}$$

and corrections can be applied to this quantity to obtain the averaged beam valence structure function $\overline{F}_0(x_1)$. The projection, $\overline{F}(x_1)$, of the data using the deep inelastic scattering structure functions[113] for the target nucleon is shown in Figure 59. The upper curve shows the value for the projection, $\overline{F}(x_1)$, expected from the Drell-Yan model. The lower curve shows the averaged sum of valence quark distributions, $\overline{F}_0(x_1)$, that would be expected if the cross section could be written exactly as a the product of a function of x_1 and a function of x_2. Both curves have been multiplied by the antiproton K factor discussed above. It is clear by comparing the curves that the terms neglected by the projection are small even at the lowest accessible values of x_1. The projection of the target structure function,

$$\overline{G}(x_2) = \frac{x_2^2}{\sigma_0} \frac{d\sigma}{dx_2} \left[\int F_0(x_1) \frac{dx_1}{x_1^2} \right]^{-1},$$

using the deep inelastic scattering structure functions for the antiproton is shown in Figure 60. Again the upper curve shows the Drell-Yan prediction for the projection, $\overline{G}(x_2)$, while the lower curve represents the corresponding sum of quark structure functions $\overline{G}_0(x_2)$ that would be obtained if the cross section factorized exactly. It is again evident from the curves that the neglected terms are small.

Figure 61 shows the projection of the antiproton valence structure function data compared with 150 GeV/c data from the NA3 experiment using both antiproton and proton data to subtract away non-valence contributions. Corrections for the neglected terms have been applied to our data points on this plot. There is good agreement between the experiments about both the shape and normalization of the data points.
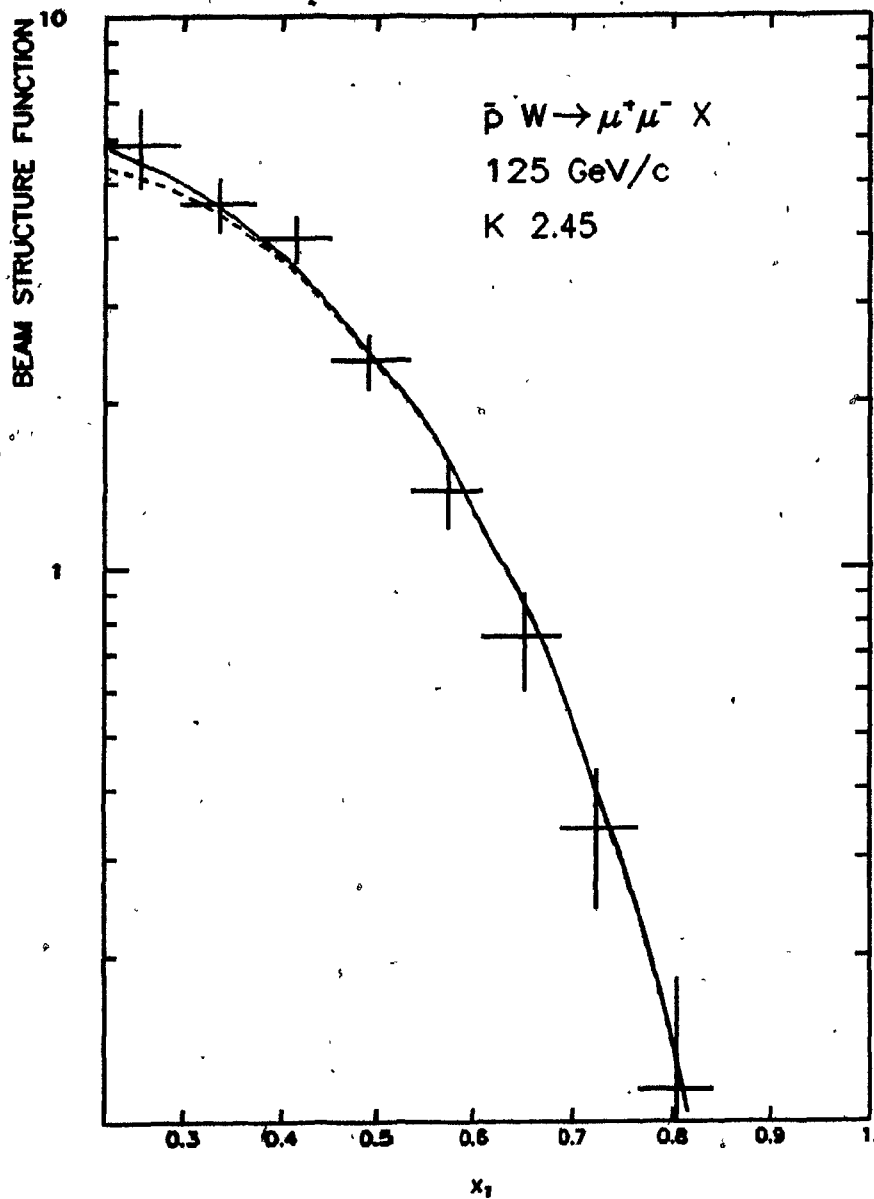
Figure 59 - Antiproton Beam Structure Function Projection

The points show the projection of our antiproton produced data on the x_1 axis. The upper curve shows the projection, $\overline{F}(x_1)$, expected from the Drell-Yan model. The lower curve shows the averaged sum of valence quark structure functions, $\overline{F}_0(x_1)$, that would be expected if the cross section could be written exactly as the product of a function of x_1 times a function of x_2.
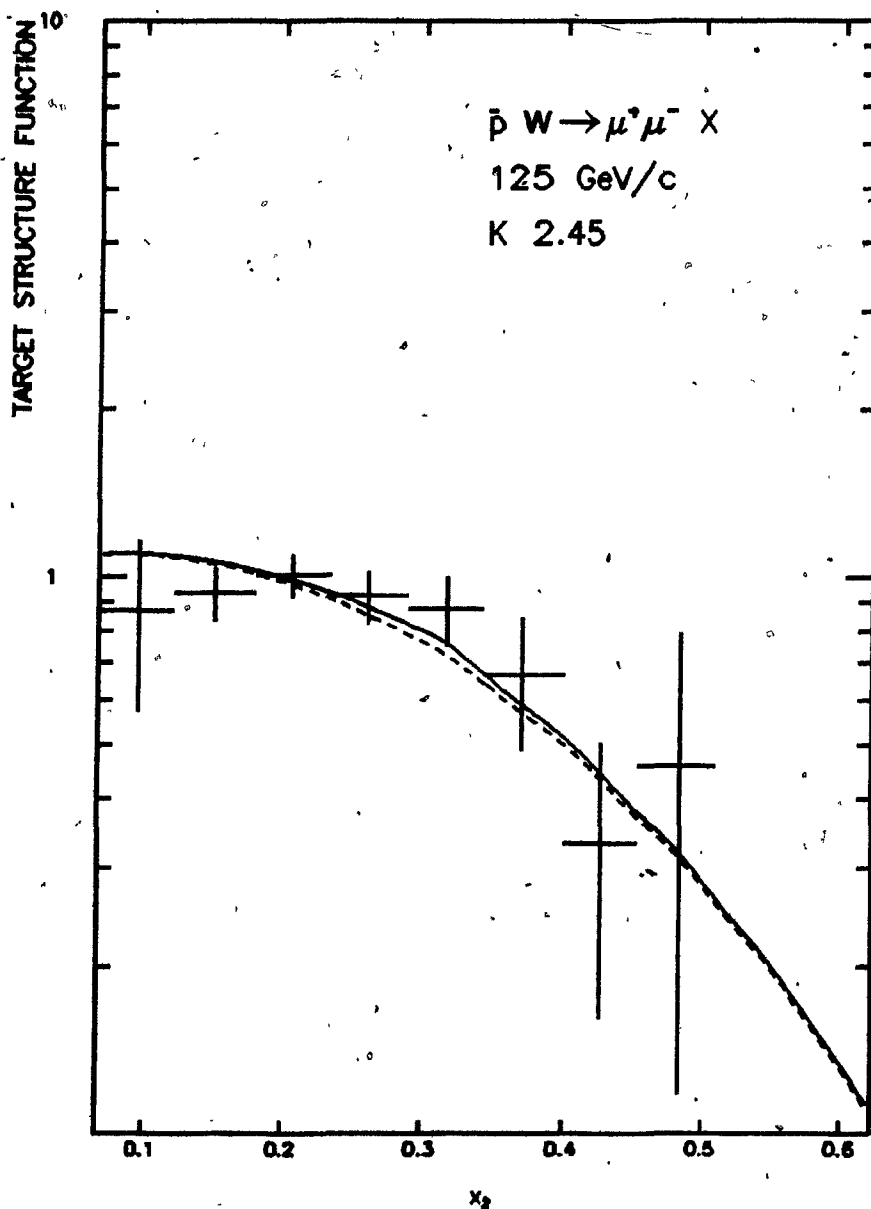
Figure 60 - Antiproton Target Structure Function Projection

The points show the projection of our antiproton produced data on the x_2 axis. The upper curve shows the result, $\overline{G}(x_1)$, expected from the Drell-Yan model. The lower curve shows the valence quark structure function $\overline{G}_0(x_1)$.
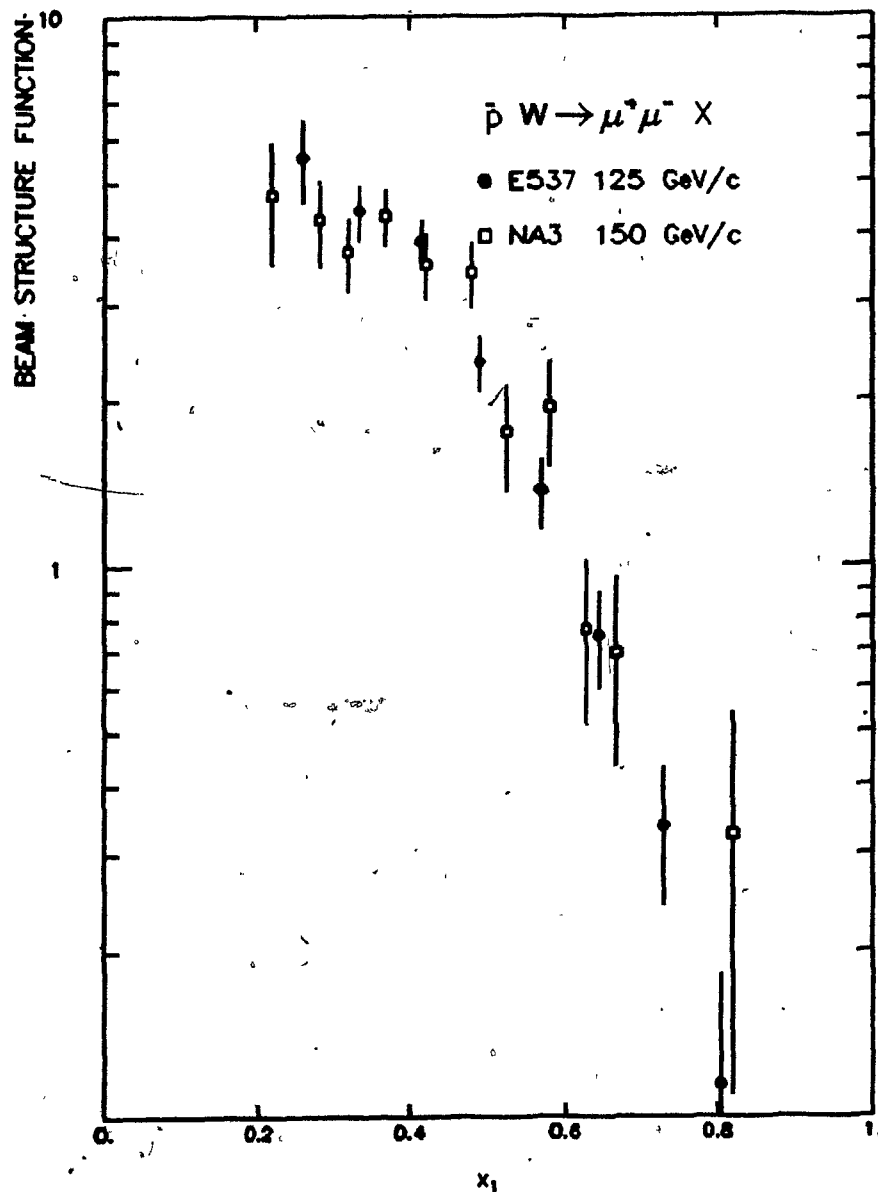
Figure 61 - Antiproton Beam Structure Function Compared To NA3

Our projected antiproton valence quark structure function is compared with data obtained by the NA3[10] collaboration.

Figure 62 shows the beam structure function projection, $\overline{F}(x_1)$, projected from the pion data using the deep inelastic structure functions for the target nucleon. The upper curve shows the results expected for the projection, $\overline{F}(x_1)$, from the Drell-Yan model. The lower curve shows the sum of valence quark distributions, $\overline{F}_0(x_1)$, that would be expected if the cross section factorized exactly. Here we have used the parameters from Set 9 of Table 13 for the pion valence structure function, the NA3[46] 200 GeV/c results for the pion sea, and the deep inelastic scattering structure functions[113] for the target nucleon, to calculate the Drell-Yan curves. The Drell-Yan curves have been multiplied by a factor of

$$K_{\pi^-} = 2.39$$

to normalize to the measured cross setion. The projection of the target structure function, $\overline{G}(x_2)$, for the pion data is shown in Figure 63. The curves again show the values expected for $\overline{G}(x_2)$ and $\overline{G}_0(x_2)$ from the Drell-Yan model, and again the terms neglected by the projection are small. Comparisons of our beam structure function with data from the NA3[46], CIP[40], Omega[43], and GOLIATH[44] collaborations are shown in Figure 64. Note that we have adjusted the CIP points on this plot to reflect our assumed A dependence. The agreement between ourselves and the other experiments is very good over the entire x_1 range, both in shape and absolute value. Our target structure function is compared to the results obtained by NA3[46] and CIP[40] in Figure 65. Again the agreement is quite good in both cases.

7.6 Conclusion

This thesis has reported the results of an experiment which has measured muon pair production in 125 GeV/c antiproton-tungsten and
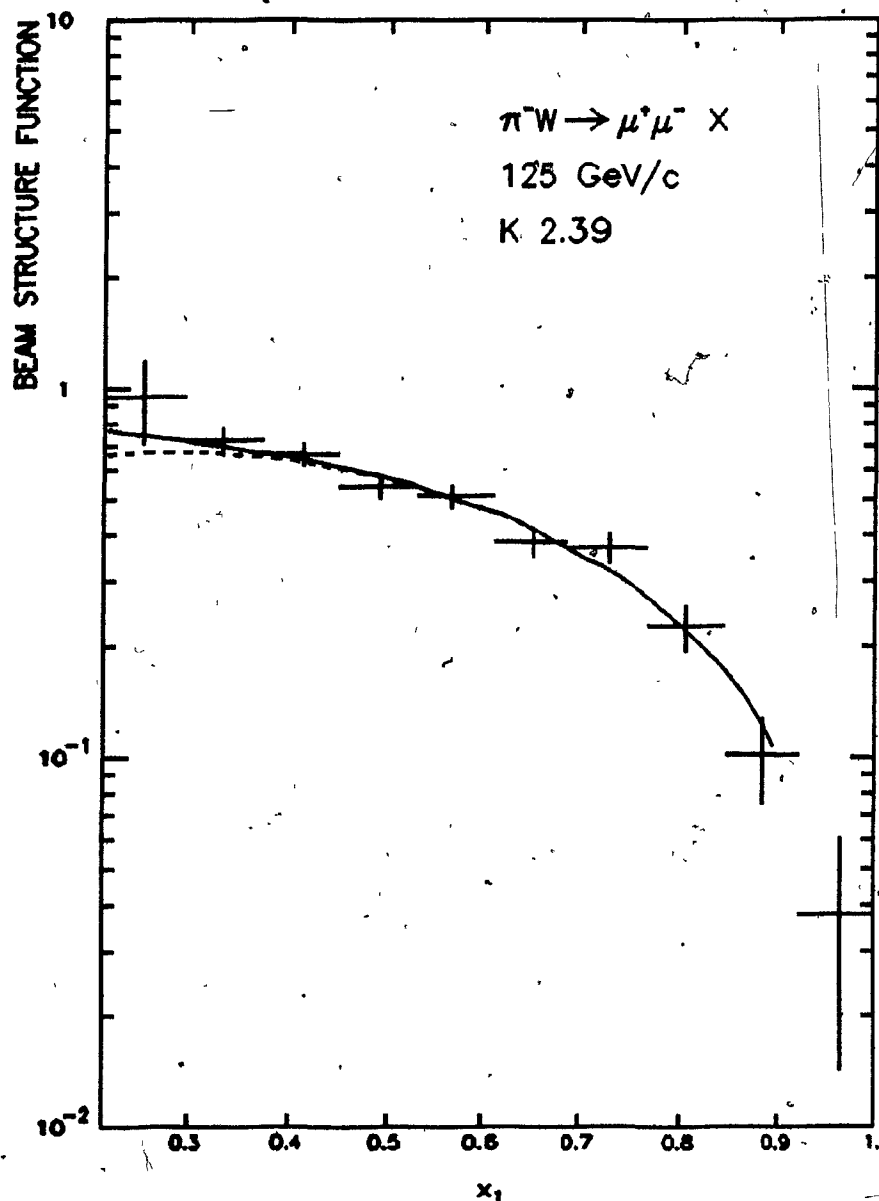
Figure 62 - Pion Beam Structure Function Projection

The points show the projection of our pion produced data on the x_1 axis. The upper curve shows the result, $\overline{F}(x_1)$, expected from the Drell-Yan model. The lower curve shows the averaged sum of valence quark structure functions, $\overline{F}_0(x_1)$.
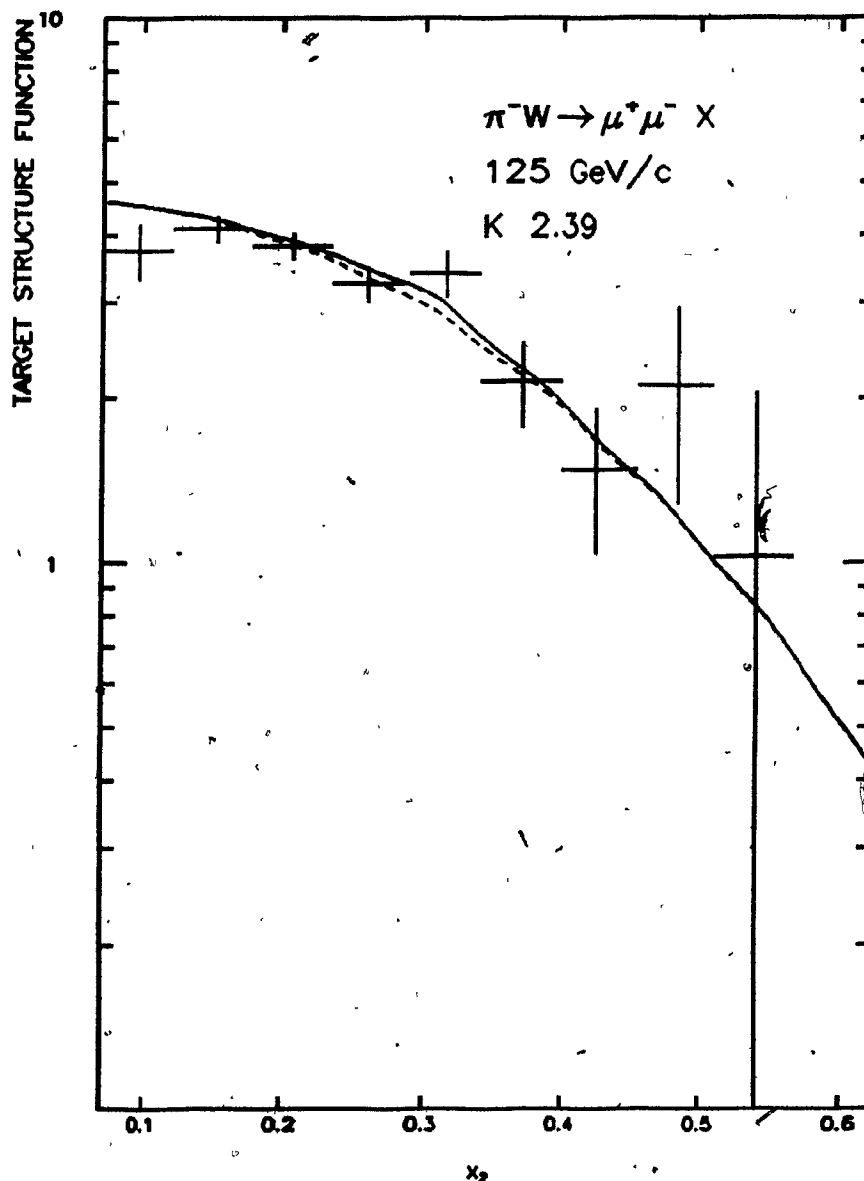
Figure 63 - Pion Target Structure Function Projection

The points show the projection of our pion produced data on the x_2 axis. The upper curve shows the result, $\overline{G}(x_2)$, expected from the Drell-Yan model. The lower curve shows the valence quark structure function $\overline{G}_0(x_2)$.
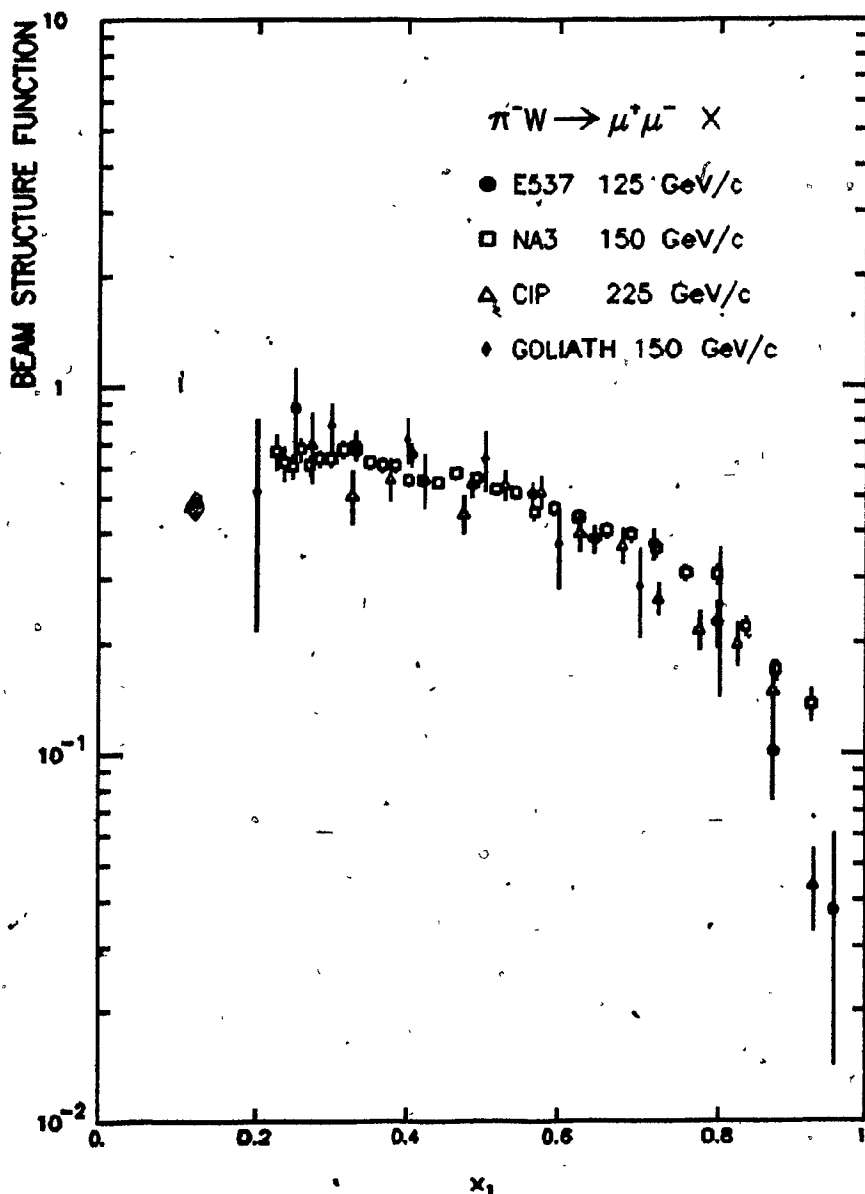
Figure 64 - Pion Beam Structure Function Comparison

Our projected pion valence quark structure function is compared with data from the NA3[46], CIP[40], and Goliath[44] experiments. There is good agreement between the four experiments.
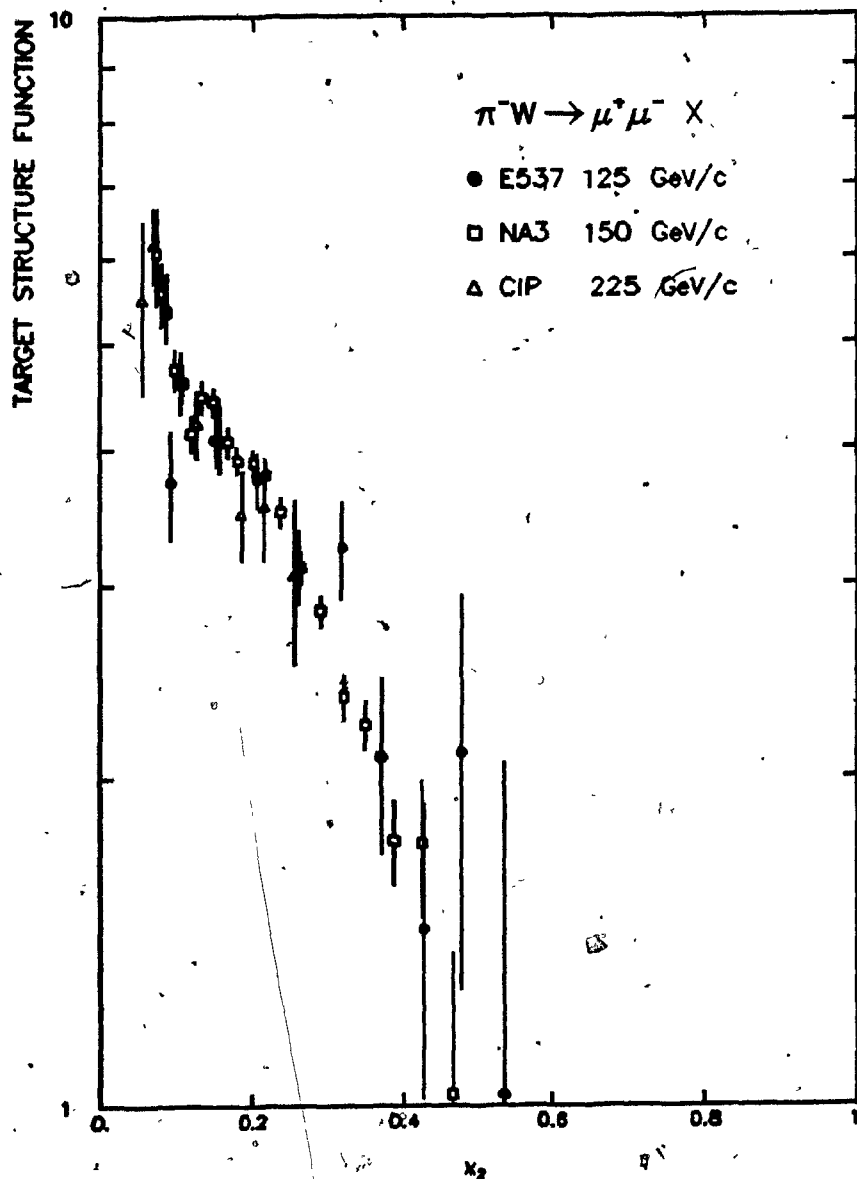
Figure 65 - Rion Target Structure Function Comparison

The nucleon structure function projected from our pion produced data is compared to data from the NA3[46], and CIP[40] experiments.

pion-tungsten collisions using a tungsten target, a spectrometer with good acceptance for masses between 4.0 and 9.0 GeV/c^2 with $x_F \geq 0$, and a beam tagging system capable of counting and identifying individual beam particles. The measurement of the cross section for muon pair production by antiprotons provides an unambiguous test of the Drell-Yan model and QCD corrections since the valence quark structure functions of the nucleon have been accurately determined in deep inelastic lepton scattering experiments. Our sample of 387 events and our identification of individual beam particles give us the best measurement of the cross section for muon pair production by antiprotons to date. Because of the scaling properties of the cross section predicted by the Drell-Yan model, comparison of the pion produced data to results from other experiments using different beam energies provides a valuable cross-check on the antiproton results as well as testing the model itself.

We find that both the kinematic dependences and the absolute normalization of the cross section for pion produced pairs agrees well with measurements by other experiments. We also find good agreement with the only other data for antiproton produced pairs. We have compared our measurements of the differential cross sections, $\frac{d\sigma}{dM}$ and $\frac{d\sigma}{dx_F}$, for the production of muon pairs in antiproton-tungsten collisions to the predictions of the Drell-Yan model using nucleon structure functions measured in deep inelastic scattering and find good agreement between the data and the model if we multiply the predictions by

$$K_{\bar{p}} = 2.45.$$

The leading order QCD corrections make only small changes in the predicted kinematic dependences of the cross sections but increase the absolute magnitude of the predicted cross section by a factor of 1.87, so that we

find that the experimental cross section exceeds the leading order prediction by a factor of

$$\sigma_{Experimental}/\sigma_{LO} = 1.41.$$

Calculations of the cross section for muon pair production in pion-tungsten collisions involve large uncertainties because the pion valence quark structure function cannot be measured in inelastic scattering experiments. The pion produced, data does, however, exhibit the qualitative features expected from the model. The differential cross section, $\frac{d\sigma}{dM}$, falls more quickly with increasing mass for antiprotons than for pions as would be expected from the model on the basis of counting rule arguments. The differential cross section, $\frac{d\sigma}{dx_F}$, also falls more quickly with increasing x_F for antiprotons as would be expected from the same arguments. The angular distributions, $\frac{1}{\sigma} \cdot \frac{d\sigma}{d\cos\theta}$ and $\frac{1}{\sigma} \cdot \frac{d\sigma}{d\phi}$, are also consistent with the expectations of the Drell-Yan model for both the pion produced data and the antiproton produced data.

The Drell-Yan formula has been inverted and used to obtain the antiproton structure function from the data. Again we find good agreement between our results and data obtained by the NA3 collaboration[10] using a 150 GeV/c beam. The shape of the antiproton structure function is also in good agreement with the shape of the proton structure function measured by deep inelastic scattering experiments. The pion structure function extracted in the same way agrees well with measurements by other muon pair experiments both in shape and magnitude.

It is clear that antiproton experiments with higher statistics are necessary to make detailed comparisons of the shapes of the kinematic distributions with the Drell-Yan model and the first order QCD predictions

in different ranges of M and x_F. Experiments with good acceptance over the whole range of $\cos\theta$ and ϕ would be able to determine the variation of the angular distributions with M, x_F, and p_T. Experiments at higher beam energies will be able study the scaling violations predicted by QCD. Some of this work is already underway. The NA10[51] experiment at CERN has reported preliminary results from extensive measurements of the cross section for pion produced pairs using a 194 GeV/c beam incident on a tungsten target. Two experiments at Fermilab, E605[53] and E615[54], are measuring muon pair production in proton-tungsten and pion-tungsten collisions respectively. The latter experiment in particular was designed to have good acceptance over the entire range of $\cos\theta$.

Appendix I - E537 Collaboration

E. Anassontzis, S. Katsavenas, P. Kostarakis, C. Kourkoumelis,
A. Markou, L.K. Resvanis G. Voulgaris

University of Athens, Athens, Greece

M. Binkley, B. Cox, J. Enagonio, C. Hojvat, D. Judd, R.D. Kephart,
P.K. Malhotra, P.O. Mazur, C.T. Murphy, F. Turkot, R.L. Wagner,
D. Wagoner, W. Yang

Fermi National Accelerator Laboratory, Batavia, IL 60510, USA

H. Areti, S. Conetti, P. Lebrun, D. Ryan, T. Ryan, W. Schappert,
D. Stairs

McGill University, Montreal, Province of Quebec, H3A2T8, Canada

C. Akerlof, X. Cui, P. Kraushaar, D. Nitz, R. Thun, L. Wang

University of Michigan, Ann Arbor, MN 48109, USA

He Mao, Zhang Nai-jian

Shandong University, Jinan, Shandong, Peoples Republic of China

Appendix II - Vertex Reconstruction

The resolution of the spectrometer was limited by multiple scattering of the muons in the copper hadron filter. Substantial improvement was achieved in the mass resolution by fixing the production vertex at the centre of the target as discussed in the text. This was possible once the event was known to have originated in the target, but the misassignment of an event produced in the dump to the target could result in a substantial error in the reconstructed mass. A simple distance of closest approach method allowed most events to be unambiguously assigned to either the dump or the target but enough events remained unresolved to cause concern about bias in the kinematic distributions. A better determination of the production point was made by finding the most probable vertex for the pair of muons using a Gaussian model for multiple scattering.

The model for multiple scattering used here is due to Fermi and is discussed by Rossi and Greisen[131] and in Rossi's book[132]. The algorithm used to find the best vertex is a straightforward adaptation of techniques originally applied to cosmic ray tracks in cloud chambers[133], and was more recently used in other muon pair experiments[128][134]. The implementation of the algorithm in this case was discussed in some detail by Kraushaar[85] but will be outlined here because of its importance.

In the limit of small scattering angles, negligible energy loss, many separate scatters, and working in the projection on the Y-Z plane as illustrated in Figure 66, the probability that a particle travelling along the Z axis and entering a scatterer at $Y = Z = 0$, will emerge a distance Y from the Z axis, with an angle θ_Y with respect to the Z axis, is given by
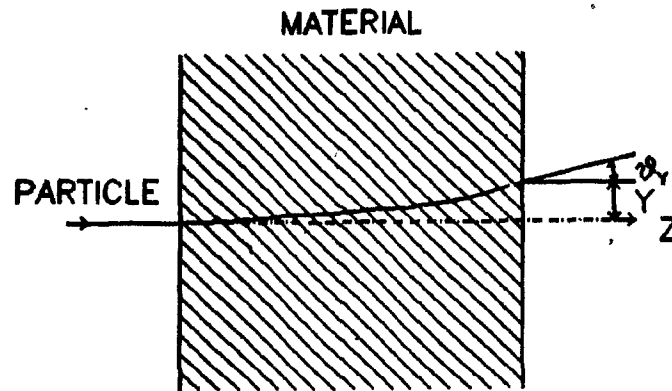
Figure 66 - Multiple Scattering

A charged particle, normally incident at Y = Z = 0, will undergo multiple Coulomb scattering with the nuclei of a target material. After traversing a length Z of material the particle will emerge with a spatial displacement Y and an angular displacement θ_Y.

$$P(Y, \theta_Y | Z) = \frac{2\sqrt{3}}{\pi \theta_{YRMS}^2 Z^2} \exp\left(-\frac{4}{\theta_{YRMS}^2 Z}(\theta_Y - 3\theta_Y\psi + 3\psi^2)\right)$$

where ψ is the dimensionless ratio

$$\psi = Y/Z.$$

The plane projected RMS scattering angle is commonly taken to be[13]

$$\theta_{YRMS} = \frac{0.015}{\beta p} \sqrt{\frac{Z}{Z_{rad}}}$$

where

β is the velocity of the particle in units of c,

p is the momentum of the track in GeV/c,

Z is the length of the scatterer, and

Z_{rad} is the of the radiation length[13] for the scattering material.

The probability that a particle which enters the scatterer at $Y = Z = 0$, travels to an intermediate point Y_1, Z_1 with angle θ_1, then emerges at a point Y_2, Z_2, at an angle θ_2, is given by

$$P(Y_1, Y_2, \theta_1, \theta_2 | Z_1, Z_2) =$$

$$P(Y_1, \theta_1 | Z_1) \cdot P(Y_2 - Y_1 - \theta_1(Z_2 - Z_1), \theta_2 - \theta_1 | Z_2 - Z_1) =$$

$$A \cdot \exp(-\chi^2/2)$$

where we have defined the various parameters that appear as follows:

$$A = 2\sqrt{3}/[\pi \theta_{YRMS}^2 k^2 (1-k)^2 z_2^4],$$

$$\chi^2/2 = \frac{4}{\theta_{YRMS}^2 Z_2} (\delta^2 + \xi^2 + \omega^2 + \vartheta^2),$$

$$\delta^2 = \frac{1}{k(1-k)} \left(\theta_1 + \frac{3}{2}\frac{2k-1}{1-k}\psi_1 - \frac{3}{2}\frac{k}{1-k}\psi_2 + \frac{k}{2}\theta_2\right)^2,$$

$$\xi^2 = \frac{3}{4}\frac{1}{k(1-k)^3}(\psi_1 - k(3-2k)\psi_2 + k(1-k)\theta_2)^2,$$

$$\omega^2 = 3(\psi_2 - \frac{1}{2}\theta_2)^2,$$

$$\theta^2 = \frac{1}{4} \theta_2{}^2,$$

and the dimensionless variables are

$$k = Z_1/Z_2;$$

$$\psi_1 = Y_1/kz_2, \text{ and}$$

$$\psi_2 = Y_2/Z_2.$$

Integration over all values of θ_1 using

$$d\theta_1 = \sqrt{k(1-k)} \, d\delta$$

gives the probability that a particle entering a scatterer at $Y = Z = 0$ is observed at Y_1, Z_1 and emerges from the scatterer at Y_2, Z_2 with angle θ_2.

It is straightforward to generalize to the case of a particle produced at a point Y_0, Z_0 at an angle θ_0, being observed at a point Y_1, Z_1 and emerging at a point Y_2, Z_2 with angle θ_2 by making the following substitutions:

$$\theta_2 \rightarrow \theta_2 - \theta_0,$$

$$Y_2 \rightarrow Y_2 - (Z_2 - Z_0)\theta_0, \text{ and}$$

$$Y_1 \rightarrow Y_1 - (Z_1 - Z_0)\theta_0.$$

For the case of two particles produced at a common vertex at Y_0, Z_0 with angles θ_{01} and θ_{02}, and being observed with Y_{11}, Y_{21}, θ_{21} and Y_{12}, Y_{22}, θ_{22} respectively, as shown schematically in Figure 67, the total probability will be the product of the individual probabilites. Scattering in the X direction can be treated in exactly the same fashion.

Here the drift chambers were used to give measurements of the track positions and slopes downstream of the dump, that is at Z_2. The absorber chamber gave information about the track coordinates 2/3 of the way through
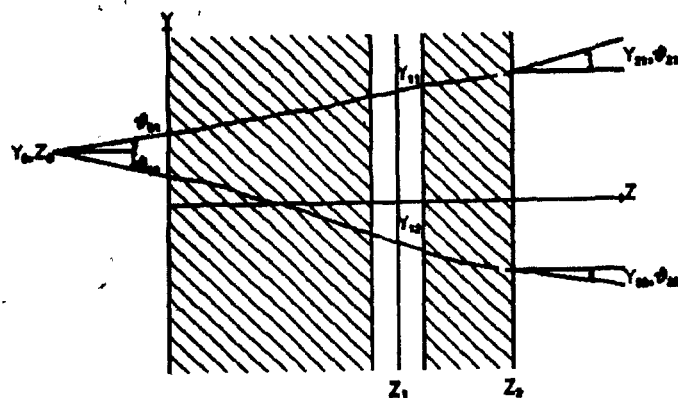
Figure 67 - Vertex Reconstruction

The Z position of the production vertex of the muon pair was calculated by finding the point Z_0, Y_0 which gave the highest probability of observing the muons at their actual positions as discussed in the text.

the dump at Z_1. The beam chambers were used to determine the X and Y of the production vertex. The Z position of the production vertex was found by numerically searching for the values of Z_0 and the production angles, θ_{01} and θ_{02}, that gave the the highest value of the probability function in the above expressions. The search was performed using ZXSSQ, a FORTRAN callable nonlinear minimization routine from the IMSL library[135].

Appendix III - Reinteraction Correction

The incident beam is attenuated in the target according to the well known exponential law,

$$I(Z) = I_0 \exp(-Z/L_{Abs}),$$

where L_{Abs} is the absorption length of the target material. If each particle removed from the beam creates dn secondary particles in the energy range dE, then the number of secondaries, di, created in the interval dz will be

$$\frac{di}{dz} = -\frac{dI}{dz}\frac{dn}{dE}.$$

If the absorption length does not depend on energy, each secondary created in an element of length dz will see a target of effective length

$$L_{Eff}(Z) = L_{Abs}[1 - \exp(-\frac{L-Z}{L_{Abs}})]$$

where L is the physical length of the target. If $o(E)$ denotes the cross section for the production of muon pairs by secondary particles of energy E, the number of muon pairs dN (within constant factors) produced by secondaries created in the element of length dz will be

$$\frac{dN}{dz} = -I_0/L_{Abs} \exp(-\frac{L}{L_{Abs}}) \cdot L_{Abs}[1 - \exp(-\frac{L-Z}{L_{Abs}})] \cdot \int_0^{E_{max}} \frac{dn}{dE} o(E) \, dE.$$

Integrating from $Z = 0$ to $Z = L$ gives

$$N(L) = N_0[1 - (1 + \frac{L}{L_{Abs}})\exp(-\frac{L}{L_{Abs}})]$$

where we have defined

$$N_0 = I_0 L_{Abs} \int_0^{E_{max}} \frac{dn}{dE} o(E) \, dE.$$

This quantity depends only on the physical processes taking place and not on the length of the target.

In contrast, the number of muon pairs produced by primary particles depends on the target length as

$$N_{Direct}(L) = N_{0Direct}[1 - \exp(-\frac{L}{L_{Abs}})],$$

where

$$N_{0_{Direct}} = I_0 \cdot \sigma(E_{max}) \cdot L_{Abs}$$

which again does not depend on the target length. The measured cross section will then be

$$\sigma_{Measured}(L) = [N_{Direct}(L) + N_{Secondary}(L)] / [I_0 L_{Abs}(1 - \exp(-\frac{L}{L_{Abs}}))]$$

$$= \sigma_{Direct} + \sigma_{Reinteraction}[1 - \frac{L}{L_{Abs}} / (\exp(\frac{L}{L_{Abs}}) - 1)]$$

where

σ_{Direct} is the cross section that would be measured using an infinitesimally thin target, and

$\sigma_{Reinteraction}$ is a constant independent of the length of the target. This expression can be fit to cross sections measured using targets of different lengths to obtain σ_{Direct} and $\sigma_{Reinteraction}$. Once these are given, the expression can be used to calculate the correction for reinteraction for a target of any length.

List of References

1. Christenson,J., et al., Phys.Rev.Lett. 25, 1523 (1970).

2. Rutherford,E., Phil.Mag. 21, 669 (1911).

3. Chadwick,J., Nature 129, 312 (1932).

4. Chadwick,J., Proc.Roy.Soc. A136, 692 (1932).

5. Hofstadter,R., Ann.Rev.Nucl.Sci. 7, 231 (1958).

6. Gell-Mann,M., Phys.Lett. 8, 214 (1964).

7. Zweig,G., CERN Report 8182/Th.401, CERN, Geneva, Switzerland (1964).

8. Pennington,M.R., Rep.Prog.Phys. 46, 393 (1983).

9. Marciano,W., and H.Pagels, Phys.Rept. 36, 137 (1978).

10. Badier,J., et al., Phys.Lett. 96B, 422 (1980).

11. Drell,S., and Yan,T.M., Phys,Rev.Lett. 25, 578 (1970).

12. Drell,S., and Yan,T.M., Ann.Phys. 66, 578 (1970).

13. Particle Data Group, Review of Particle Properties, Published in Phys.Lett. 111B, 1 (1982).

14. Politzer,H.D., Nucl.Phys. B129, 301 (1977).

15. Bodwin,G., Brodsky,S., and Lepage,G., Phys.Rev.Lett. 47, 1799 (1981).

16. Lindsay,W., Ross,D., and Sachrajda,C., Nucl.Phys. B222, 189 (1983).

17. Lindsay,W., Ross,D., and Sachrajda,C., Nucl.Phys. B214, 61 (1983).

18. Lyons,L., Prog.Part.and.Nucl.Sci. 7, 169 (1981).

19. Stroynowski,R., Phys.Rept. 71, 1 (1981).

20. Kenyon,I., Rept.Prog,Phys. 45, 1264 (1982).

21. Tran Than Van,J.,ed., 1981 Moriond Workshop, Les Arcs; Editions Frontiers, Dreux, France.

22. Berger,E., et al., Proceedings of the Drell-Yan Workshop, Fermilab, Batavia, IL 60510, USA. (October 1982).

23. Gottfreid,K., and Jackson,J.D., Nuovo Cimento 33, 309 (1964).

24. Collins,J., and Soper,D., Phys.Rev.D 16, 2219 (1977).

25. Lam,C.S., and Tung,W.K., Phys,.Rev.D 18, 7 (1978).

26. Collins,J. Phys.Rev.Lett. 42, 291 (1979).

27. Politzer,H.D., Nucl.Phys. B129, 301 (1977).

28. Sachradja,C.T., Phys.Lett. 73B, 185 (1978).

29. Kubar,J., et al., Nucl.Phys. B175, 271 (1979).

30. Altarelli,G., et al., Nucl.Phys. B157, 461 (1979).

31. Curci,G., and M.Greco, Phys.Lett. 92B, 175 (1980).

32. Contogouris,A., and L.Marleau, Phys.Rev D 28, 1644 (1983).

33. Marleau,L., Unpublished Ph.D. Thesis, McGill University (1983).

34. Kenyon[20] reviews Drell-Yan A dependence.

35. Aubert,J., et al., Phys.Lett. 123B, 123 (1983).

36. Bodek,A., et.al, Phys.Rev.Lett. 50, 1431 (1983).

37. Bodek,A., et al., Phys.Rev.Lett. 51, 534 (1983).

38. Ito,A., et al., Phys.Rev.D 23, 604 (1981).

39. Anderson,K., et al., Phys.Rev.Lett. 42, 944 (1979).

40. Hogan,G., Phys.Rev.Lett. 42, 948 (1979).

41. Corden,M.J., et al., Phys.Lett. 76B, 226 (1978).

42. Corden,M.J., et al., Phys.Lett. 96B, 411 (1980).

43. Corden,M.J., et al., Phys.Lett. 96B, 417 (1980).

44. Barate,R., et al., Phys.Rev.Lett. 43, 1541 (1979).

45. Badier,J., et al., Unpublished Preprint CERN-EP/84-16 CERN, Geneva, Switzerland (February 1984).

46. Badier,J., et al., Phys.Lett. 89B, 145 (1979).

47. Badier,J., et al., Unpublished Preprint, CERN/EP 80-148, CERN, Geneva, Switzerland (August 1980).

48. Lefrancois,L., 1980 Proc.Int.Conf. on High-Energy Physics, Madison. AIP Conf 68 pg. 1319 (1980).

49. Badier,J., et al., Zeit.Phys.C 11, 195 (1981).

50. Michelini,A., Unpublished Preprint CERN-EP/81-128, CERN, Geneva, Switzerland (1981).

51. Varela,J., Ecole Poly. Paliseau Preprint LPHNE/X 83-02, Presented to 1983 Moriond Conf. La Plagne, (January 1983).

52. Falciano,S., et al., Unpublished Preprint CERN-EP/81-52, CERN, Geneva, Switzerland (1981).

53. Lederman,L., et al., Fermilab Proposal P605, Fermilab, Batavia, IL 60510, USA. (1978).

54. Anderson,K., et.al, Fermilab Proposal P615, Fermilab, Batavia, IL 60510, USA. (1978).

55. J.R.Sanford, Ann.Rev.Nucl.Sci. 26, 151 (1976).

56. Cox,B., et al., Unpublished P-WEST Design Report, Fermilab, Batavia, IL 60510, USA. (March 1977).

57. Cox,B., Fermilab Report, pg.6 Fermilab, Batavia, IL 60510, USA. (January 1979).

58. Agoritsas,V., AGS Tech. Note 136, BNL, Upton, NY 11973 USA., (June 28 1977), discusses the SEMs used at Fermilab.

59. Hornstra,F., and Simanton,J., NIM 77, 303 (1970).

60. Hornstra,F., and Simanton,J., NIM 68, 138 (1969).

61. Kephart,R., and Kerns,C., Unpublished Technical Memo TM-1157, Fermilab, Batavia, IL 60510, USA. (1979).

62. Mfg. Nuclear Enterprises Corp., San Carlos, CA 94070 USA.

63. Mfg. Amperex Corp., Elk Grove Village, IL 60007, USA.

64. Mfg. RCA Corp., Des Plaines, IL 60018, USA.

65. Kerns,C:, IEEE Trans.Nucl.Sci. NS-24, 353 (1977).

66. Mfg. Lecroy Research Services, Spring Valley, NY 10977, USA.

67. US AEC Committee, Standard Nuclear Instrument Modules, TID-20893 (Rev. 4), GPO, Washington, DC, USA. (1974).

68. Mfg. Pilot Chemicals Division, New England Nuclear Corp., Waterton, MS 02172, USA.

69. Charpak,G., Ann.Rev.Nucl.Sci. 20, 195 (1970).

70. Rice-Evans,P., Spark, Streamer, Proportional and Drift Chambers, Richelieu, London, (1974).

71. Sauli,F., CERN Report 77-09, CERN, Geneva, Switzerland (May 1977).

72. Daum,H., et al., NIM 152, 541 (1979).

73. Kirsten,F.A., Ann.Rev.Nucl.Sci. 25, 510 (1975) discusses CAMAC.

74. Mfg. EMI Corp., Plainview, NY 11803, USA.

75. Areti,H., et al., NIM 212, 135 (1983).

76. Barsotti,E., IEEE Trans.Nucl.Sci. NS-26, 686 (1979).

77. Barsotti,E., et al., Unpublished TM-821 2nd ed., Fermilab, Batavia, IL 60510, USA. (1979).

78. Hammond,H.W., and M.S.Ewing, DECUS Program Library Routine 11-32, DECUS, Marlboro, MS 01752, USA (November 1980).

79. Mfg. Digital Equipment Corp., Maynard, MS 01754, USA.

80. Beil,J.,and R.J.Dosen, Unpublished PN-1+2, Fermilab, Batavia, IL 60510, USA. (November 1979).

81. Beil,J.,and R.J.Dosen, Unpublished PN-148, Fermilab, Batavia, IL 60510, USA. (May 1979).

82. Mfg. Digital Pathways, Mt.View, CA 94043, USA.

83. Akerlof,C.and Nitz,D., Proc. Digital Equipment Users Society, San Diego Meeting, DECUS, Marlboro, MS 01752, USA (November 1980).

84. Akerlof,C., and Nitz,D., Unpublished SUPERGRAM Users Guide, University of Michigan, Ann Arbor, MN 48104, USA (1980).

85. Kraushsaar,P., Unpublished Thesis, University of Michigan, Ann Arbor MN 48104, USA., (November 1982).

86. Mfg. Control Data Corp., Minneapolis, MA 55440, USA.

87. Sauli,F., CERN Report 77-09 pg.52, CERN, Geneva, Switzerland, (May 1977).

88. Koizumi,G., Unpublished Technical Memo TM-786, Fermilab, Batavia, IL 60510, USA., (May 1978).

89. This program was written by R.Wagner of Fermilab.

90. For example see Roy,R., and Nigram,B., Nuclear Physics, Wiley, N.Y. NY, USA., for a discussion of the Fermi Gas Model.

91. Moniz,E., et al., Phys.Rev.Lett. 26, 445 (1971).

92. The Fermi momentum for Cu was taken to be the same as for Ni as measured by [91].

93. The Fermi momentum for Be was interpolated between Li and C[91] using $P_{Fermi}=C_0+C_1/A$.

94. Fermi motion effects are discussed by Bodek,A., and Ritchie,J., Phys.Rev.D 23, 1070 (1981).

95. Anassontzis,E., et.al, Unpublished Preprint Fermilab-CONF 82/50-EXP, Fermilab, Batavia, IL 60510, USA., (July 1982).

96. James,F., Rep.Prog.Phys 42, 3 1145 (1983).

97. Common Library Mathematical Routines, Pub. 60483100, Control Data Corp, Minneapolis MA 55440, USA.

98. NORRAN, CERN Program Library, Routine U101, CERN, Geneva, Switzerland.

99. Ahrens,J., and Dieter,U., Comm. ACM 15, 873 (1972).

100. Lindelof,T., CERN Program Library Routine V101, CERN, Geneva, Switzerland.

101. Carroll,A.S., et al., Phys.Lett. 80B, 319 (1979).

102. Richard-Serre,C., CERN Report 71-18, CERN, Geneva, Switzerland (1971).

103. Serre,C., CERN Report 67-5, CERN, Geneva, Switzerland (1967).

104. Joseph,P., NIM 75, 13 (1969).

105. Schreider,Y.,ed., The Monte Carlo Method, Peragamon, London. (1966).

106. See for example, J.Badier et al., Zeit.Phys.C 11, 195 (1981), or J.de Groot, Zeit.Phys.C 1, 143 (1979).

107. Eadie,W., et al., Statistical Methods in Experimental Physics, North Holland, Amsterdam, (1971).

108. Frodesen,A., et al., Probability and Statistics in Particle Physics, Universitetforlaget, Oslo (1979).

109. Johnson empirical distributions are discussed by Eadie et al.,[107].

110. James,F., and Roos,M., CERN Program Library Routine D506, CERN, Geneva, Switzerland (1971).

111. MINUIT uses the Davidon variable matrix algorithm described in Davidon,W. Computer J. 10, 406 (1968).

112. Van Ginnekin,A., Unpublished Technical Memo FN-272, Fermilab, Batavia, IL 60510, USA. (Jan. 1975).

113. Duke,D., and J.Owens, Unpublished Preprint FSU-HEP-831115, Florida State University, Tallahasse, FA 32306, USA (1983).

114. Lipps,H., CERN Program Library Routine D112, CERN, Geneva, Switzerland (1979).

115. Aubert,J.,et al., Phys.Lett. 105B, 315 (1981).

116. Clark,A., et al., Phys.Rev.Lett. 51, 1826 (1983).

117. MacFarlane,D., et al., Unpublished Preprint Fermilab 83/108-EXP, Fermilab, Batavia, IL 60510, USA. (January 1984).

118. Abramowicz,H., et al., Zeit.Phys.C 17, 283 (1983).

119. Aubert,J., et al., Phys.Lett. 123B, 123 (1983).

120. Aubert,J., et al., Phys.Lett. 105B, 322 (1981).

121. Bodek,A., et al., Phys.Rev.D 20, 1471 (1979).

122. Devoto,A., et al., Phys.Rev.D 27, 508 (1983).

123. Barker,I., B.Martin and G.Shaw, Zeit.Phys.C 19, 147 (1983).

124. Brodsky,S., and Farrar,G., Phys.Rev.Lett. 31, 1153 (1973).

125. Brodsky,S., and Farrar,G., Phys.Rev.D 11, 1309 (1975).

126. Badier,J., Phys.Lett. 96B, 422 (1980).

127. Callot,O., Unpublished Thesis, Universite de Paris Sud, Orsay, France (1981).

128. Newman,C., Unpublished Thesis, University of Chicago, Chicago, IL 60637, USA. (March 1979).

129. Farrar,G., Nucl.Phys. B77, 429 (1974).

130. Badier,J., et al., Zeit.Phys.C 18, 281-287 (1983).

131. Rossi,B., and Greisen,K., Rev.Mod.Phys. 13, 240 (1941).

132. Rossi,B., High Energy Particles, Prentice Hall, Englewood Cliffs, NJ ,USA. (1952).

133. Scott,W.T., Phys.Rev. 76, 212 (1949).

134. Badier,J., et al., NIM 175, 319 (1980).

135. ZXSSQ, IMSL Library Reference Manual, 9th ed., IMSL, Houston, TX 77036, USA (1982).